Optimal control of solar sails

Alesia Herasimenka

UNIVERSITÉ CÔTE D'AZUR

ÉCOLE DOCTORALE
SCIENCES FONDAMENTALES ET APPLIQUÉES

THÈSE DE DOCTORAT

Contrôle optimal des voiles solaires

Alesia Herasimenka

Laboratoire Jean Alexandre Dieudonnée, CNRS, équipe GAD
Centre Inria d'Université Côte d'Azur, équipe McTAO

Présentée en vue de l'obtention du grade de docteur en mathématiques appliquées **d'**Université Côte d'Azur
Dirigée par : Jean-Baptiste Caillau, Lamberto Dell'Elce, et Jean-Baptiste Pomet
Soutenue le : 7 septembre 2023

Devant le jury, composé de :
Jean-Baptiste Caillau, Professeur, Université Côte d'Azur
Massimo Casasco, Ingénieur, European Space Agency
Bernd Dachwald, Professeur, Aachen University
Lamberto Dell'Elce, Chargé de recherche, Inria
Ariadna Farrès, Chercheuse, NASA, University of Maryland
Pascal Morin, Professeur, Sorbonne Université
Jean-Baptiste Pomet, Directeur de recherche, Inria
Daniel J. Scheeres, Professeur, University of Colorado
Emmanuel Trélat, Professeur, Sorbonne Université

Inria esa

Contrôle optimal des voiles solaires

Optimal control of solar sails

Jury :

Président du jury
Pascal Morin, Professeur, Sorbonne Université

Rapporteurs
Bernd Dachwald, Professeur, Aachen University
Daniel J. Scheeres, Professeur, University of Colorado
Emmanuel Trélat, Professeur, Sorbonne Université

Examinateurs
Jean-Baptiste Caillau, Professeur, Université Côte d'Azur
Lamberto Dell'Elce, Chargé de recherche, Inria
Ariadna Farrès, Chercheuse, NASA, University of Maryland
Jean-Baptiste Pomet, Directeur de recherche, Inria

Invité
Massimo Casasco, Ingénieur, European Space Agency

Résumé

Cette thèse porte sur le contrôle optimal des voiles solaires qui sont des engins spatiaux propulsés par la pression de radiation solaire. Les voiles solaires génèrent une force propulsive en réfléchissant et en absorbant les photons, ce qui en fait un moyen de navigation spatiale rentable et pratiquement illimité.

La première partie de la thèse est consacrée à l'étude de la contrôlabilité des voiles solaires. Le principal défi pour évaluer leur contrôlabilité réside dans les contraintes spécifiques imposées à l'ensemble de contrôle. Une voile solaire ne peut générer de force que dans des directions situées à l'intérieur d'un cône convexe et est incapable de créer une force dirigée vers le Soleil. Les méthodes traditionnelles de vérification de la contrôlabilité sont mises en défaut en raison de ces contraintes physiques. Une condition alternative est proposée, qui permet notamment d'identifier les directions non-atteignables dans le fibré tangent associé à la variété d'état du système. Ces résultats théoriques sont applicables à tout système périodique avec une contrainte conique sur son ensemble de contrôle.

Pour vérifier cette condition, un problème d'optimisation est formulé, permettant une vérification effective. La solution s'appuie sur une approche par somme de carrés en optimisation convexe, ainsi que sur le caractère polynomial trigonométrique de la dynamique. Une contribution significative de cette étude est la détermination d'une exigence minimale en termes de propriétés optiques que la voile doit satisfaire, à même de faciliter la conception d'une telle voile pour des missions spatiales. Cette méthodologie est étendue à tout type d'orbite périodique et de propulsion pour le maintien à poste.

La deuxième contribution de cette thèse est un algorithme conçu pour calculer le contrôle optimal permettant de déplacer la voile selon une direction prescrite de l'espace des phases. L'algorithme utilise l'optimisation convexe pour obtenir un contrôle admissible mais sous-optimal en tant qu'initialisation. Ensuite, un problème de contrôle optimal est résolu visant à maximiser le déplacement dans la direction souhaitée. En analysant la dynamique hamiltonienne du système, une fonction de commutation est identifiée, qui régit la structure de la commande. Une borne supérieure sur le nombre de zéros de cette fonction est établie, qui permet une mise en œuvre efficace d'un code de tir multiple couplé à une continuation différentielle.

Un scénario original de mission d'occultation du Soleil est finalement analysé à l'aide de techniques de contrôle optimal. La Terre est utilisée pour occulter le Soleil, et non sa couronne qui est beaucoup moins brillante mais physiquement importante à étudier (en lien, notamment, avec les tempêtes géomagnétiques). La riche géométrie de la zone d'occultation du Soleil ainsi que la connaissance de la dynamique du problème restreint à trois corps au voisinage du point de Lagrange considéré sont autant d'atouts pour proposer une stratégie d'observation efficace, soulignant l'intérêt des voiles solaires pour ces futures missions.

Mots-clés : contrôle optimal, mécanique spatiale, contrôlabilité, voiles solaires, optimisation convexe.

Abstract

This thesis focuses on the optimal control of solar sails, which are spacecraft propelled by the pressure of solar radiation. Solar sails generate propulsive force by reflecting and absorbing photons, making them a cost-effective and practically unlimited means of space propulsion.

The first part of this thesis is dedicated to the controllability study of solar sails. The primary challenge in assessing their controllability arises from the specific constraints imposed on the control set. Due to the nature of solar radiation pressure, a solar sail can only generate force whose directions belong to a convex cone, and is unable to create a force directed towards the Sun. Traditional methods for evaluating controllability are inadequate due to these specific constraints. To address this challenge, an alternative condition is proposed, which involves identifying forbidden directions in the tangent bundle associated with the system state manifold. These theoretical results are applicable to any periodic system with a conical constraint on its control set.

To verify this condition, an optimization problem is formulated, enabling an effective assessment. The solution utilizes the theory of squared functional systems and the ability to express the dynamics by means of trigonometric polynomials. A significant contribution of this study is the determination of a minimum requirement in terms of optical properties that satisfy the necessary local controllability condition. This minimum angle provides valuable insights into the optical constraints of solar sails, facilitating their design for space missions. Furthermore, this methodology is expanded so as to be applicable to any periodic orbit and any type of propulsion for station-keeping purposes.

The second contribution of this thesis is an algorithm designed to compute the optimal control inputs for steering the sail towards a desired direction within the phase space. The algorithm employs convex optimization to obtain an admissible yet suboptimal control as an initial input. Subsequently, an optimal control problem is solved to maximize the displacement in the desired direction. By analyzing the Hamiltonian dynamics of the system, the relevant switching function that governs the structure of the solution is identified. Additionally, an upper bound on the number of zeros of this function is established, enabling the efficient implementation of a multiple shooting code using differential continuation.

Finally, an original scenario of a Sun occultation mission is analyzed using optimal control techniques.

The Earth is used to occult the Sun, but not its corona that is much less bright but physically important to study (in relation, *e.g.*, to geomagnetic storms). The rich geometry of the sun occultation zone together with the knowledge of the dynamics of the three-body restricted problem in the vicinity of Lagrange points is used to propose an efficient observation strategy. These results highlight the interest of solar sails for these future missions.

Keywords: optimal control, space mechanics, controllability, solar sails, convex optimization.

Acknowledgments

First of all, I would like to acknowledge my dearest directors Jean-Baptiste Caillau, Lamberto Dell'Elce, and Jean-Baptiste Pomet. I am very grateful that the circumstances allowed me to meet the McTAO team. Thank all three of you for being much more than just thesis directors to me. Jean-Baptiste (C), for everything that I learned and for your help with so many things during these three years, from growing as a scientific researcher to becoming a French citizen. Jean-Baptiste (P), for being so involved, spending time on our endless discussions and explanation of differential geometry to me, even though you officially became my director only a couple of weeks before my defense. And finally, Lamberto, for raising my confidence, for teaching me so much that it's impossible to list it, for always being there whenever I needed, and for having been my true mentor. Thank all three of you for your advices and encouragements throughout these years, I am very proud of having you as my thesis directors.

I also want to acknowledge the members of my jury: Bernd Dachwald, Dan J. Scheers, and Emmanuel Trélat for reading and discussing my manuscript and providing me with valuable feedback. I appreciate the insightful exchanges we had during various conferences. I would like to express my gratitude to Ariadna Farrès for our multiple fruitful meetings, our collaborative work, and your support. Pascal Morin played a crucial role in making this PhD possible: thank you for this and for supporting me during my master. I'm thankful to Massimo Casasco and Samir Bennani from ESA for our discussions, your time and involvement in my work. Additionally, I'd like to thank Lorenzo Niccolai and Ludovic Rifford for the participation in my thesis committee and for offering advice on my work.

Another special thanks to Slava Turyshev, who invited me to my very first solar sail workshop, where I met the community. I'm also grateful for making possible to visit NASA JPL and for your valuable advice, support and inspiration.

I acknowledge my excellent interns, Paul Chambroux and Tommy Calendini, for their motivation and the quality of their work. They made my first supervisory experience so much easier.

A huge thank you to Valeryia Sauchanka and Ali Gharib, who were always there for me and played important roles in my personal growth over the years. I would also like to acknowledge Marie Yakimovich, Elizaveta Belous and Nicolás

Vattuone for your friendship and the adventures we shared. Thanks to the entire Biocore-McTAO team for making Inria such a pleasant place to work (especially the after-work gatherings): Marielle Péré, Clotilde Djuikem, Bruno Assis, Juan Carlos Arceo, Odile Burckard, Frank De Veld, Antonin Bavoil, Ignacio Fierro, Adel Annabi, David Morgado, Walid Djema and the others.

Thanks a lot to my Parisian family who came to support me during this important day and to whom I am so grateful for being part of my life: Tristan Venot, Luc Bruchet, Luc Brémaud, Poeiti Dorado, Clément Lutringer, Auxane Haffreingue, Hermès McGriff, Gonzague Lenfant.

And finally, I would like to say a special thanks to my parents, my brother and my grandmother, Ina, Aliaksandr, Artsiom and Tatsiana, all with the same last name as me, for everything, and in particular for traveling thousands of kilometers by car from Minsk, Belarus to Nice, France, just to share this particular moment with me. I hope so much that in the very close future Minsk - Nice or any other trip will be easy again and I will be able to go home whenever I want to see my family that I love so much. Бясконцы дзякуй вам.

Funding

This work was partially funded by the European Space Agency's Discovery programme under contract 4000134950/21/NL/GLC/my. The view expressed in this work can in no way be taken to reflect the official opinion of the European Space Agency.

Contents

List of acronyms

AU	astronomical unit
AD	automatic differentiation
CRTBP	circular restricted three-body problem
DAE	differential-algebraic equation
DFT	discrete Fourier transform
FFT	fast Fourier transform
GVE	Gauss variational equations
IVP	initial value problem
JAXA	Japan Aerospace Exploration Agency
JPL	Jet Propulsion Laboratory
JWST	James Webb Space Telescope
LARC	Lie algebra rank condition
LMI	linear matrix inequalities
OCP	optimal control problems
ODE	ordinary differential equation
PMP	Pontryagin's maximum principle
SRP	solar radiation pressure
STLC	small-time locally controllable
TPBVP	two-point boundary value problem

List of thesis-related publications

Journal papers and papers under revision

A. Herasimenka, L. Dell'Elce, J.-B. Caillau and J.-B. Pomet. Controllability properties of solar sails. *Journal of Guidance, Control, and Dynamics* 46 (2023), no. 5, 900–909.

A. Herasimenka, L. Dell'Elce, J.-B. Caillau and J.-B. Pomet. Optimal control of a solar sail. HAL preprint no. 04158202, 2023.

J.-B. Caillau, L. Dell'Elce, A. Herasimenka and J.-B. Pomet. On the controllability of nonlinear systems with a periodic drift. HAL preprint no. 03779482, 2022.

Conference papers

A. Herasimenka, L. Dell'Elce, J.-B. Caillau and J.-B. Pomet. Impact of optical properties on the controllability of solar sails. International Conference on Astrodynamics Tools and Techniques, (2021).

A. Herasimenka, L. Dell'Elce, J.-B. Caillau and J.-B. Pomet. Controllability test for fast-oscillating systems with constrained control. Application to solar sailing. European Conference and Control (2022), 2143-2148. Proceedings of ECC22, London, July 2022.

A. Herasimenka, A. Farrés and L. Dell'Elce. Station-keeping under conical constraint on the control force. HAL preprint no. 04156856, 2023.

A. Herasimenka, A. Farrés and L. Dell'Elce. Controllability of satellites on periodic orbits with cone-constraints on the thrust direction. Space Flight Mechanics Meeting, (2023).

L. Dell'Elce, A. Herasimenka, A. J. Rosengren, N. Baresi. Efficient numerical solution of the low-thrust Lambert problem. Space Flight Mechanincs Meeting (SFMM), 2023.

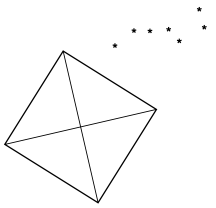

Introduction

"In those days interplanetary voyages were an everyday occurrence, and interstellar travel not uncommon. Rockets took tourists to the wondrous sites of Sirius, or financiers to the famous stock exchanges of Arcturus and Aldebaran. But Jinn and Phyllis, a wealthy leisured couple, were distinguished in their cosmos for their originality and a few grains of poetry. They wandered over the universe for their pleasure — by sail.

Their ship was a sort of sphere with an envelope — the sail — which as miraculously fine and light and moved through space propelled by the pressure of light-radiation. Such a machine, left to its own devices in the vicinity of a star (though far enough away for the field of gravity not to be too powerful), will always move in a straight line in the opposite direction of the star..."

Those are the first lines of the book "Planet of the Apes" [5], written by Pierre Boulle in 1963. In this captivating novel, Boulle introduces the concept of a spacecraft propelled through space by the pressure of light-radiation, creating a mesmerizing vision of solar sailing. Arthur C. Clarke, a notable science fiction writer, also explored the idea of solar sailing in his book "The Wind from the Sun: Stories of the Space Age" [15]. Within this collection of stories, Clarke delves into the captivating journeys and adventures made possible by solar sailing.

Thus, the concept of solar sails has intrigued not only scientists and engineers but also writers and artists, igniting imaginations and revolutionizing space exploration. The idea of utilizing light pressure, akin to sailboats, for travel in space with free and perpetual propulsion has captured the collective dreams of many.

The history of solar sails dates back to James Clerk Maxwell's publication of his theory of electromagnetic fields and radiation in 1861-1864, which demonstrated that light possesses a momentum and can exert pressure on objects. As early as 1903, Konstantin Tsiolkovsky proposed the use of sunlight pressure to propel spacecraft, envisioning the potential of utilizing enormous mirrors made of thin sheets to achieve cosmic velocities in his work "The Exploration of Cosmic Space by Means of Reaction Devices."

In the 1970s, space agencies began considering solar sails for space exploration,

eventually leading to the launch of the first sails into space. With progress in materials and technology, alternative propulsion methods have gained traction in space missions. Traditional, heavy, chemically propelled satellites are expensive and time-consuming to design, build, and launch. In contrast, small, lightweight satellites not only offer new possibilities for space missions but also enable universities, private companies, and research institutes to launch their own spacecraft for various scientific objectives. Solar sails, along with other low-thrust satellite technologies, are instrumental in enabling these projects.

Thanks to their continuous acceleration provided by light, these sails are capable of gathering a lot of energy by passing close to the Sun. Coupled with their relatively low cost, small light sails that can travel quickly and cover large distances are the key to further space exploration.

Although Pierre Boulle accurately pictured the fascination with space sailing, he was mistaken about the maneuverability of solar sails. Fortunately, solar sails are not limited to moving in a straight line, nor do they require three stars to navigate in multiple directions as depicted in the book. However, controlling a solar sail is indeed a challenging task due to the primary constraint of solar radiation pressure (SRP), namely the sail can only generate a force that goes in the direction opposite to the Sun, not towards it. When photons reach the sail surface, they are either absorbed or reflected, exerting a force in a specific direction based on the incoming rays and the optical properties of the material. From a control perspective, solar sails are control-constrained systems, meaning that their control options are limited to a convex cone that contains all possible thrust directions. In layman's terms, solar sails can only be "pushed" away from the Sun. Nevertheless, by leveraging the gravitational fields of the Sun and other celestial bodies, solar sails are capable of executing various maneuvers.

Given these constraints, the first part of the thesis addresses the question: "Can solar sails generate an arbitrary change of their unperturbed orbit?" This question revolves around the controllability property, which refers to the system capability to move to any desired point of the phase space. Analyzing controllability involves examining the existence of non-reachable regions, which is crucial for mission design. However, studying solar sails using classical geometric control theory is not obvious because of the specific constraints imposed by the limited set of available forces. To address this challenge, the thesis proposes novel necessary or sufficient conditions of controllability for periodic systems whose control set is not a neighborhood the origin (the origin belongs to the boundary of the set). These conditions rely on periodicity of the uncontrolled motion of such systems. The controllability conditions are applicable to any system with conical constraints on its control set and are not restricted to solar sailing.

In addition to this theoretical contribution, an effective numerical approach is presented to verify these conditions. The proposed algorithm combines convex optimization techniques with the theory of positive trigonometric polynomials

to assess the controllability condition for solar sails in orbit around a celestial body. The main outcome of this study is the establishment of minimum optical property requirements for a solar sail to be controllable. These requirements can be utilized in preliminary mission design. After achieving results for solar sails, the methodology is extended beyond simple Keplerian motion and can be applied to other satellite systems. A case study featuring the James Webb Space Telescope (JWST) serves as an illustration of this contribution.

The second part of the thesis focuses on the optimal control of solar sails. Once the controllability condition is established, the following question arises: "How can a solar sail be effectively controlled?" Despite the existence of an extensive literature on solar sail control, there are still gaps in fully understanding the design of optimal trajectories around celestial bodies generated by the SRP. By studying the dynamics of solar sails, it is possible to derive optimality conditions for controlling their motion, drawing upon mathematical tools such as the Pontryagin's maximum principle (PMP). Through a comprehensive analysis of the system dynamics, various solution structures are explored, and a constraint on the number of control arcs is identified. An appropriate switching function is introduced to predict the solution structure and facilitate shooting with multiple arcs. The initial estimate for the algorithm is derived using convex optimization, ensuring the feasibility of the solutions. To achieve precise results, advanced numerical techniques such as differential continuation, callback functions, and implicit maximization of the Hamiltonian are employed to conduct simulations. These insights help to refine the strategies and techniques for achieving optimal control of solar sails in various mission scenarios.

The manuscript is structured as follows. Chapter 1 provides an introduction to solar sailing, including historical background on early missions and their outcomes, as well as gives some insight about future missions enabled by sails. It also explains the principle of SRP, and recalls some equations of the two and three-body problems that will be used throughout the thesis. Chapter 2 is dedicated to the study of controllability. Firstly, it introduces the theoretical contribution regarding the controllability of general control-affine systems with conical constraints on the control set. Next, it presents an efficient methodology for analyzing the controllability of solar sails. Finally, the proposed algorithm is extended to encompass non-Keplerian motion. Chapter 3 discusses the results obtained in the field of optimal control for solar sails. It introduces a tool for designing optimal trajectories for SRP-actuated systems. Lastly, Chapter 4 offers a preliminary analysis of a Sun occultation mission employing solar sails. In the scope of this thesis, this mission is significant because of its unique characteristics. Since several observations are required to study the Sun corona, having a propellantless sail able to take advantage not only of three-body dynamics inside the penumbra generated by the occulter, but also of the solar radiation pressure outside penumbra is particularly interesting.

Chapter 1

Dynamics of solar sails

Introduction

Although solar sailing is no longer a new concept, there have been relatively few missions that have actually been launched into space, and even fewer of them have carried scientific goals beyond simple deployment demonstrations, due to technological challenges. One notable mission often misconstrued as the first solar sail is IKAROS[1], developed by the Japan Aerospace Exploration Agency (JAXA). While it remains one of the earliest successful missions, the concept of solar sailing was actually considered as far back as 1976 at the Jet Propulsion Laboratory (JPL) for the Halley's Comet rendezvous [33]. However, one of the earliest mission that played a significant role in paving the way for future endeavors was Znamya[2] , launched in 1993 by Roscosmos, the Russian space agency, even though it faced technical difficulties and was not entirely successful.

Subsequently, the Planetary Society emerged with solar sailing as one of its main projects. In 2005, they conducted the Cosmos 1 mission[3] , which aimed to test solar sail technology. The spacecraft weighed 100 kg and incorporated eight triangular solar blades, each 15 m long, resulting in a total surface area of 600 m^2. Unfortunately, the Cosmos 1 did not reach its intended orbit due to a rocket failure.

It was not until May 2010 that JAXA successfully launched the IKAROS mission (Interplanetary Kite-craft Accelerated by Radiation Of the Sun), marking a significant milestone in solar sail missions. IKAROS featured a square sail, whose photo is shown in Figure 1.1, with an area of 196 m^2 (14 m $\times$ 14 m) made of a thin film material and weighing 2 kg, attached to a 310 kg satellite. The mission achieved its goal of concept demonstration by deploying the sail and performing attitude control through the manipulation of the sail's reflectivity using a liquid

[1] global.jaxa.jp/projects/sas/ikaros

[2] en.wikipedia.org/wiki/Znamya_(satellite)

[3] en.wikipedia.org/wiki/Cosmos_1

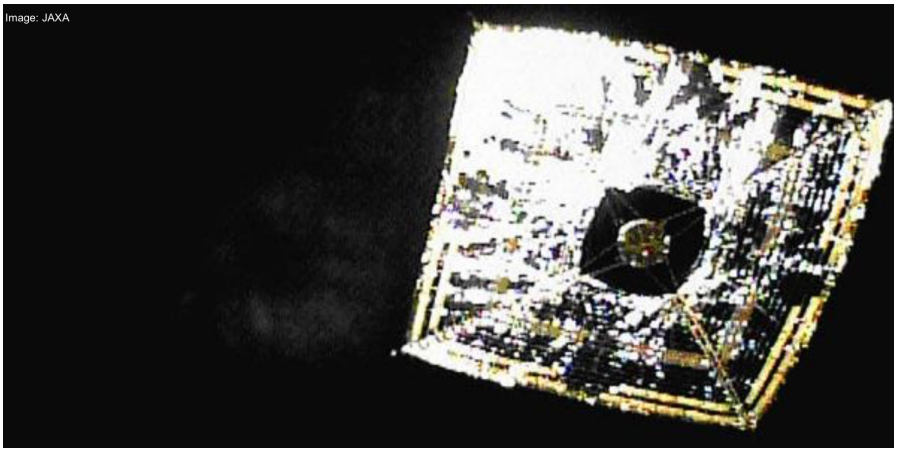

Figure 1.1: IKAROS solar sail launched in 2010 by Japan Aerospace Exploration Agency (JAXA), picture taken by a camera ejected from the satellite.

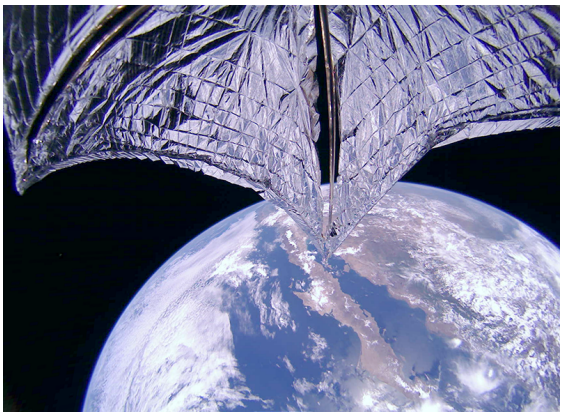

Figure 1.2: LightSail 2 selfie with the deployed solar sail.

crystal device.

Later, in 2015, the Planetary Society continued its solar sail exploration with the LightSail 1 mission[4] , deploying a 32 m^2 sail aboard a 3U CubeSat. Building upon this success, LightSail 2 was launched in 2019 with the same configuration, using solar radiation pressure to alter its orbit before ultimately reentering the Earth's atmosphere in 2022. Figure 1.2 shows a picture taken after deployment.

NASA also played a significant role in the development of the technology, although their sailing route was marked by several failures of various nature. In 2008, they launched their first solar sail mission called NanoSail-D[5]. This mission consisted of a 3U cubesat weighing 4 kg with a 10 m^2 square sail. However,

[4] planetary.org/sci-tech/lightsail
[5] nasa.gov/mission_pages/smallsats/nanosaild.html

NanoSail-D was unfortunately lost due to a problem with the launch vehicle during stage separation. Undeterred by this setback, NASA proceeded with the NanoSail-D2 mission, which was successfully deployed in 2010 as a part of the FASTSAT satellite. NanoSail-D2 spent an impressive 240 days in orbit, demonstrating the long-duration capabilities of solar sails. Another notable solar sail mission by NASA was the Sunjammer project[6], named in honor of Arthur C. Clarke's story. Sunjammer was intended to have a massive solar sail with a total surface area of 1200 m^2 and a remarkably low mass of only 32 kg. Unfortunately, the mission was cancelled after its initial launch plans in 2015. Additionally, NASA had planned an ambitious solar sail mission called Solar Cruiser[7], which aimed to launch in 2025 towards the Lagrange point L1. The mission's objective was to study solar magnetic fields using a coronagraph and gradually adjust its orbit inclination. However, this mission was also cancelled in 2022.

Lastly, the NEA-Scout mission[8] by NASA was launched in 2022 as part of the Artemis 1 mission. NEA-Scout aimed to perform reconnaissance of the asteroid 2020 GE using an 86 m^2 solar sail. Unfortunately, no communication was received from the satellite, and it is considered lost. These missions by NASA highlight their involvement and interest in advancing solar sail technology for various scientific purposes, despite the challenges and setbacks encountered along the way.

While numerous solar sails have been launched and demonstrated successful functioning, as summarized in Table 1.1, only a select few have gone beyond concept demonstrations to carry out meaningful scientific objectives. Presently, solar sailing has evolved beyond mere deployment and attitude control, offering new possibilities in mission design. Projects like NEA-Scout and JAXA's OKEANOS mission [49], are witness of such goals. OKEANOS, for instance, which combines ion thrusters with a solar sail, aimed to perform rendezvous and landing on Jupiter Trojan asteroids.

Solar sailing revolutionizes space missions by eliminating the need for propellant, enabling new types of missions that were previously considered too costly from a control perspective. A prime example is performing station-keeping maneuvers around unstable orbits, which pose significant challenges as active control is required to maintain proximity to the desired trajectory. One such mission scenario is the Sun occultation mission discussed in Chapter 4, where the goal is to observe the solar corona by occulting the Sun's disk with a natural body [2]. However, there are no natural periodic orbits suitable for this type of observation, and using chemical propulsion would be prohibitively expensive, limiting the number of feasible observations. In this context, solar sailing proves to be exceptionally advantageous as it allows the spacecraft to perform multiple observation cycles without sacrificing efficiency, limited only by the materials and

[6] nasa.gov/mission_pages/tdm/solarsail/index.html

[7] science.nasa.gov/heliophysics/programs/solar-cruiser

[8] nasa.gov/content/nea-scout

Name	Operator	Launch date	Purpose	Result	Reason
Znamya 2	Roscosmos	1992	Deployment	Success	
Cosmos 1	Planetary Society	2005	Deployment	Failure	Vehicle failure
NanoSail-D	NASA	2008	Deployment	Failure	Vehicle failure
NanoSail-D2	NASA	2010	Deployment	Success	
IKAROS	JAXA	2010	Attitude control	Success	
LightSail 1	Planetary Society	2015	Deployment	Success	
LightSail 2	Planetary Society	2019	Change of orbit	Success	
NEA-Scout	NASA	2022	Reconnaissance of an asteroid	Failure	Deployment failure

Table 1.1: Summary of some launched solar sail missions

endurance of the spacecraft.

A mission aimed at observing Sun's poles also presents a compelling opportunity for solar sailing. Except for the Ulysses[9] spacecraft, no other spacecraft has been sent to explore these regions due to the significant propulsion challenges associated with changing the orbit's inclination. Nevertheless, solar sails are uniquely suited for such missions because, as the satellite approaches the Sun, the effect of SRP becomes more prominent and extends beyond mere perturbation. The proximity to the Sun amplifies the force exerted by the sunlight on the solar sail, enhancing its maneuverability and allowing for more significant changes in the satellite's trajectory. It makes solar sail propulsion an outstanding opportunity to overcome the challenges of achieving the desired orbit inclination at the Sun's poles.

Another significant advantage of solar sails is their capability to provide substantial velocity changes, known as Δv, reaching magnitudes of several tens of kilometers per second [61]. This opens up new possibilities for missions to explore the outer solar system and even venture beyond it, ushering in a new era of space exploration. The paper [61] introduces the concept of Sundiver, which represents a novel approach to solar sail propulsion. The Sundiver vehicles are smallsats that utilize innovative materials, enabling them to achieve remarkable performance in terms of area-to-mass ratio (with a minimum of 50 m^2/kg) and high velocities.

[9] esa.int/Science_Exploration/Space_Science/Ulysses_overview

This innovative design opens up possibilities for fast and efficient propulsion using solar sails. By utilizing a spiral trajectory that brings the spacecraft closer to the Sun, with current sail materials, velocities of around 7 astronomical unit (AU) per year can be achieved. (AU is the average distance between the Earth and the Sun, approximately 149.6 million kilometers). The Sundiver concept aims at achieving exceptionally high velocities, with a target range of 20-25 AU per year.

Since NASA's pioneering mission to Jupiter with the launch of Pioneer 10 in 1972, only five other spacecraft have ventured beyond the orbit of Jupiter. Planning, launching, and reaching destinations in the outer solar system using chemical propulsion can take decades due to the slow and expensive nature of these missions. However, lightweight and compact sailcrafts have the potential to revolutionize mission design in terms of speed and cost-efficiency. The scientific community emphasizes the importance of space missions to the outer solar system for expanding our knowledge of the vast region. These missions could involve exploring challenging-to-reach asteroids, investigating the atmospheres of Uranus and Neptune, or probing the plumes emanating from various moons.

An example of such a captivating target for solar sail missions is Saturn's moon Enceladus, which has garnered significant interest among scientists due to its potential for harboring extraterrestrial life [28]. Enceladus is an intriguing moon with a subsurface water ocean, which has been confirmed through observations of plumes erupting from its south pole [53]. These plumes contain a mix of water vapor, organic compounds, and other volatile materials, providing tantalizing hints of potential habitability.

Exploring Enceladus and investigating its subsurface ocean present exciting possibilities for astrobiological studies. By deploying a solar sail-powered spacecraft to this enigmatic moon, scientists could conduct detailed analysis and sample collection within the plume region. Probing the composition of the plumes, including the presence of organic molecules and the potential for chemical signatures indicative of biological activity, would provide invaluable insights into the potential habitability of Enceladus' ocean [54, 62].

The rich history of solar sail missions illustrates the progress made in developing and refining this innovative propulsion technology. Each mission has provided valuable insights for scientists and engineers, and as technology advances and our knowledge deepens, solar sails have the potential to change significantly space exploration by offering efficient and sustainable means of spacecraft propulsion in the future.

1.1 Solar radiation pressure model

Solar light propagates through space as photons, which are massless elementary particles that travel at the speed of light, denoted as $c = 2.998 \times 10^8$ m/s. Although photons have no mass, they possess both energy and momentum. The phenomenon

of radiation pressure arises from the exchange of momentum between an object and the incoming flux of photons. The momentum of a photon is given by [19, Chap. 12]:

$$\frac{hf}{c},$$

where f represents the frequency of the electromagnetic wave in Hertz, and

$$h = 6.626 \times 10^{-34} \mathrm{J} \cdot \mathrm{s}$$

is the Planck constant. The Sun's photosphere, its outer shell that radiates light, behaves as a black body emitter, producing radiation across the entire electromagnetic spectrum. The intensity of solar radiation pressure at the surface of the Sun can be expressed as:

$$\Phi_0 = \sigma T^4 = 5.670 \times 10^{-8} \times 5777^4 = 63.15 \times 10^6 \text{ W/m}^2.$$

Here, $\sigma = 5.670 \times 10^{-8} \frac{\mathrm{W}}{\mathrm{m^2 K^4}}$ is the Stefan-Boltzmann constant, and $T = 5777$ K is the temperature of the Sun's photosphere. Sun radius is approximately 696000 km. Considering that the solar flux diminishes with the square of the distance, at the average Earth-Sun distance of 1 AU, the solar radiation intensity becomes:

$$\Phi_{SR} = \Phi_0 \frac{\text{Sun radius}}{r_\oplus} = 1367 \text{ W/m}^2$$

where $r_\oplus$ is the average distance from the Earth to the Sun. This value represents the solar radiation intensity reaching 1 AU.

Finally, a simple model for the SRP acting on a sail located at a distance r from the Sun is described by Montenbruck and Gill in [43, Chap. 3]. The formula for the pressure is given by:

$$P_{SR} = \frac{\Phi_{SR}}{c} \left(\frac{r_\oplus}{r} \right)^2,$$

A flat sail with surface A and mass m is considered in this work. The resulting force depends on various optical and geometrical properties of the sail and it is obtained by summing up the force contributions of the incoming, reflected, and thermal radiations, namely f_a, f_r, and f_e. In addition, the force given by the reflected radiation is divided into specular and diffuse components, f_{rs} and f_{ru}, respectively.

Each force component has different magnitude and direction, that can be identified through the Sun-sail direction, denoted as $\hat{s}$ and the unit vector normal to the sail having a positive component along $\hat{s}$, $\hat{n}$. We assume that both sides of the sail have the same optical properties, so only the (non-oriented) direction of the normal to the plane representing the plane will describe its attitude.[10]

[10] This assumption is not mandatory for the analysis in this chapter. We can also assume that the sail is constrained to always face the Sun with the same side, what actually happens in practice.

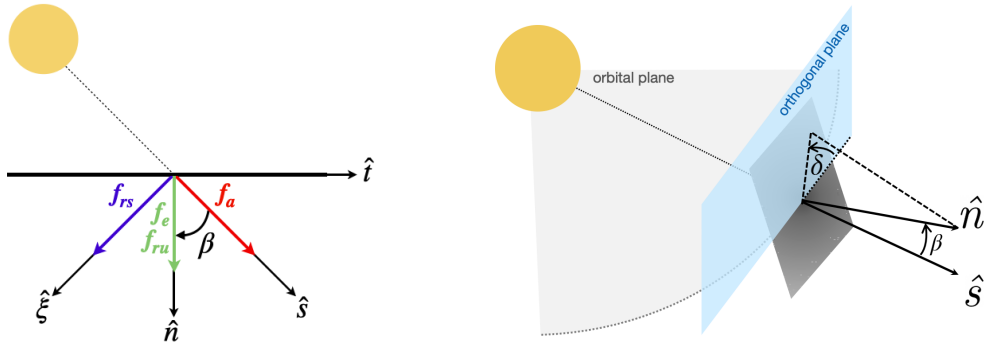

(a) Schematic representation of SRP.

(b) Orientation angles β and δ of the solar sail.

Figure 1.3: Components of the SRP force and orientation of th.

We also assume that it is possible to control the attitude, and that the actual control will be the force generated by this attitude (see Equation (1.3)). In this model, $\hat{n}$ belongs the projective plane $\mathbb{R}P^2$ that one can describe as the union of one open hemisphere (whose axis is $\hat{s}$) with a circle whose antipodal points are identified (subset of directions perpendicular to $\hat{s}$). Fixing some basis $\hat{e}_1, \hat{e}_2$ of $\{\hat{s}\}^\perp$ in order that $(\hat{s}, \hat{e}_1, \hat{e}_2)$ is a direct orthogonal frame, one defines coordinates $(\beta, \delta) \in (-\pi/2, \pi/2) \times \mathbb{R}$ for $\hat{n}$ in the open hemisphere part setting as usual (see Figure 1.3b)

$$\hat{n} = \sin\beta(\cos\delta\hat{e}_1 + \sin\delta\hat{e}_2) + \cos\beta\hat{s}.$$

This is not a chart[11] as no δ, even restricted to $\mathbb{R}/\pi\mathbb{Z}$, can be uniquely associated with the direction $\hat{s}$. (See also Remark 1.) The angle β is the so-called solar-sail *cone angle*.

As shown in Figure 1.3a, let us introduce the direction of specular reflection given by $\hat{\xi}$, and the unit tangent vector $\hat{t}$ lying in the plane generated by $\hat{s}$ and $\hat{n}$. The force due to the incoming radiation, f_a, is directed along $\hat{s}$. The force provided by the specularly reflected radiation, f_{rs}, points along $\hat{\xi}$ and is caused by photons that are reflected symmetrically with respect to the normal of the sail, thus yielding an exchange of momentum. Diffuse reflection stems from the sail surface roughness, which causes photons to be uniformly reflected in all directions, yielding a component of the force toward the direction normal to the sail, $\hat{n}$. Finally, as the absorbed photons are re-radiated in all directions, the force f_e is generated, which is orthogonal to the sail surface and points again along $\hat{n}$. We follow [40, Chap. 2] and express the unit vectors $\hat{s}$ and $\hat{\xi}$ in terms of $\hat{n}$ and $\hat{t}$,

$$\hat{s} = \cos\beta\,\hat{n} + \sin\beta\,\hat{t}, \quad \hat{\xi} = \cos\beta\,\hat{n} - \sin\beta\,\hat{t},$$

[11] One actually retrieves the universal cover of the pointed open hemisphere by restricting to (β, δ) in $(0, \pi/2) \times \mathbb{R}$.

so the above-presented forces can be expressed as [55]:

$$\begin{aligned} f_a &= \varepsilon \cos\beta\, \hat{s} = \varepsilon\, \cos\beta(\cos\beta\, \hat{n} + \sin\beta\, \hat{t}), \\ f_{rs} &= \varepsilon\rho s \cos\beta\, \hat{\xi} = \varepsilon\, \rho s\, \cos\beta(\cos\beta\, \hat{n} - \sin\beta\, \hat{t}), \\ f_{ru} &= \varepsilon\, B_f\, \rho(1-s)\cos\beta\, \hat{n}, \\ f_e &= \varepsilon\,(1-\rho)\frac{\varepsilon_f B_f - \varepsilon_b B_b}{\varepsilon_b + \varepsilon_f}\cos\beta\, \hat{n}. \end{aligned} \tag{1.1}$$

In Equation (1.1),

$$\varepsilon = \frac{AP_{SR}}{m}, \tag{1.2}$$

which combines optical and physical parameters of the sail (area A and mass m), has small magnitude depending on the distance from the Sun, $\rho \in [0,1]$ is the fraction of reflected radiation to total amount of radiation illuminating the sail, $s \in [0,1]$ is the fraction of specularly reflected radiation to total reflected radiation, ε_b and ε_f are the back and front surface emissivity coefficients, respectively, and B_b and B_f are back and front non-Lambertian coefficients, respectively. Tables 1.2 and 1.3 summarize optical and physical parameters relevant to solar sail modeling, and offer some of their values for known solar sail missions.

The SRP force is found as:

$$f_{SRP} = f_a + f_{rs} + f_{ru} + f_e.$$

Let us use the notations used in [42]:

$$b_1 = 1 - \rho s, \quad b_2 = 2\rho s, \quad b_3 = B_f\rho(1-s) + (1-\rho)\frac{\varepsilon_f B_f - \varepsilon_b B_b}{\varepsilon_f + \varepsilon_b}.$$

With these, the SRP force reads (note that because of the radial symmetry, its norm is independent of δ)

$$f_{SRP} = \varepsilon\cos\beta \begin{pmatrix} (b_1+b_2)\cos^2\beta + b_3\cos\beta + b_1\sin^2\beta \\ b_2\sin\beta\cos\beta\sin\delta + b_3\sin\beta\sin\delta \\ b_2\sin\beta\cos\beta\cos\delta + b_3\sin\beta\cos\delta \end{pmatrix}.$$

Remark 1. *In our modeling, the magnitude of the SRP is continuous with respect to $\hat{n}$, going to zero when the Sun direction is contained in the sail plane (orthogonality of $\hat{s}$ and $\hat{n}$), but its direction is not: when going through $\hat{s} \perp \hat{n}$, the illuminated side of the sail (a thickless 2D object embedded into 3D space) is changed and the orientation of $\hat{n}$ is changed to opposite ($\beta = \pm\pi/2$ being changed to $-\beta$, still defining the same direction—a perpendicular to $\hat{s}$—in the projective plane). The resulting force, going to zero in such cases, is continuous but not*

Notation	Parameter	Range of values
Optical properties		
ρ	reflectivity	$[0,1]$
s	specular reflectivity	$[0,1]$
$\varepsilon_f, \varepsilon_b$	front and back emissivity	$[0,1]$
B_f, B_b	front and back non-Lambertian coefficients	$[0,1]$
Physical properties		
A	area	$\mathbb{R}^+$
m	mass	$\mathbb{R}^+$

Table 1.2: Summary of optical and physical parameters

Solar sail	Area [m^2]	Mass [kg]	Area-to-mass ratio	Reflectivity ρ
IKAROS	196	307	0.6	0.85
LightSail 2	32	5	6.4	0.82
NanoSail-D2	10	4	2.5	not available
Sunjammer	1200	32	37.5	0.90
Sundiver	not available	not available	≥ 50	not available

Table 1.3: Summary of parameters of different solar sails

smooth. This singularity is inherent to the modeling and would be removed in a more realistic approach describing the sail as a genuine 3D object. This lack of smoothness is nonetheless not crucial here since, as will be clear from the optimality analysis in Section 3.1, an optimal force will have discontinuities, being either zero or with $\beta \in (-\beta^*, \beta^*)$ and $0 < \beta^* < \pi/2$ (if we exclude the ideal case for which $\beta^* = \pi/2$). So flips of illuminated side will not be encountered.

1.2 Parametrization of the control set

Changing the sail attitude, *i.e.* the normal vector $\hat{n}$, allows to control the direction and magnitude of the resulting SRP. A reliable inference of optical coefficients is indeed mandatory to accurately estimate the mapping $f_{SRP}(\hat{n})$. To carry out our analysis, solar sail dynamics is conveniently modeled as a nonlinear

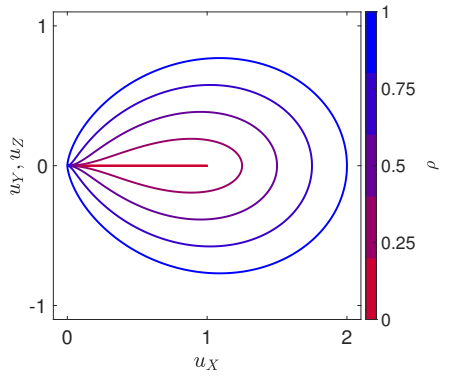

(a) Control sets for different reflectivity coefficients and $s = 1$.

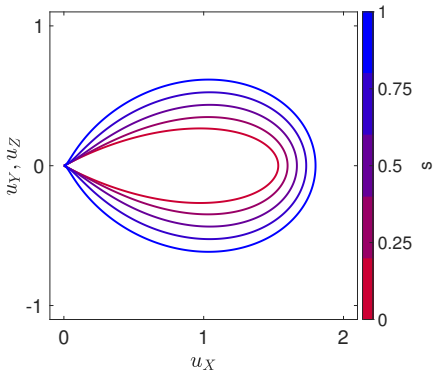

(b) Control sets for different specular reflectivity coefficients and $\rho = 0.8$.

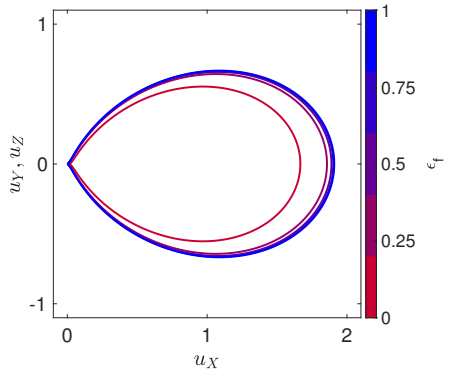

(c) Control sets for different front emissivity coefficients.

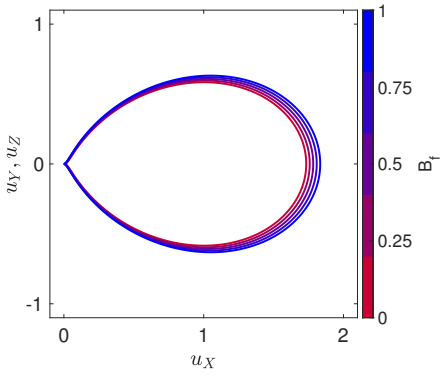

(d) Control sets for different front non-Lambertian coefficients.

Figure 1.4: Deformation of the control set with respect to the various optical properties of the sail.

control-affine system (see Section 1.3), where the control variable is homogeneous to the renormalized force. The control set $U \subset \mathbb{R}^3$ is so given by:

$$U = \left\{ u = \frac{f_{SRP}(\hat{n})}{\varepsilon} \in \mathbb{R}^3,\ \hat{n} \in \mathbb{R}P^2 \right\}. \tag{1.3}$$

It is a closed surface of revolution with axis $\hat{s}$ that bounds a domain of $\mathbb{R}^3$. Up to the scaling factor ε, this surface is the image of the projective plane by the mapping f_{SRP}. As a result, the surface minus the origin is parametrised by (β, δ) in $(-\pi/2, \pi/2) \times \mathbb{R}$, while the origin corresponds to the image of the circle of directions orthogonal to $\hat{s}$. Figure 1.4 shows the intersection of U with the plane generated by $\hat{n}$ and $\hat{s}$ for various optical properties. The resulting curve now bounds a two-dimensional domain, non-convex unless the sail is ideal ($\rho = s = 1$, so the sail is perfectly reflective, a first extreme case). In addition to ideal sails, another

extreme case can be identified: contrary to perfectly reflective sails, perfectly absorptive surfaces are the worst-case scenario ($\rho = 0$, f_e neglected) because SRP is systematically parallel to $\hat{s}$, as shown in red in Figure 1.4a. Although sails are designed to be as close to ideal as possible, partial absorption of the energy is unavoidable in real-life applications, and also optical properties exhibit degradation in time. Hence, the fraction of reflected radiation decreases with the lifetime of the satellite as discussed in [21, 47]. Another significant optical coefficient that plays a crucial role in determining the control set is the specular reflectivity, s, as illustrated in Figure 1.4b. The red set represents a sail with a rough surface (corresponding to $s = 0$), where light is diffusely reflected in all directions. This results in a smaller control set, even for a high reflectivity value of $\rho = 0.8$. In Figures 1.4c and 1.4d, the impact of other optical coefficients, namely emissivity and non-Lambertian coefficients, is shown. These coefficients have a small but noticeable effect on the shape and convexity of the control set. (The ideal solar sail is the only exception, exhibiting a vertical tangency at its vertex.)

1.3 Space mechanics

In this section, we will outline some equations of space mechanics that will be used throughout this work. Because various mission scenarios are considered in this manuscript, ranging from missions in orbit around a celestial body to station-keeping around periodic orbits in three-body problems, both equations of motion of the perturbed two-body problem and of the circular restricted three-body problem (CRTBP) are introduced herein.

According to Newton's law of universal gravitation, every particle in the universe attracts every other particle with a force that is proportional to the product of their masses and inversely proportional to the square of the distance between their centers, namely

$$F = -G\frac{m_1 m_2}{\|r\|^3} r$$

Starting from there, it is possible to derive equations of motion for N bodies.

1.3.1 Two-body problem

The two-body problem tackles the relative motion of two bodies in space under the influence of their mutual gravitational attraction, neglecting any other external perturbation. In this problem, we consider two bodies with masses m_1 and m_2, denoted as the primary body and the secondary body, respectively. The positions of these bodies are represented by vectors r_1 and r_2.

The force acting on the secondary body due to the primary body can be calculated using Newton's law of universal gravitation. According to this law,

the force F_2 on the secondary body is given by:

$$F_2 = -G\frac{m_1 m_2}{\|r_2 - r_1\|^3}(r_2 - r_1)$$

where G is the gravitational constant. This force acts in the direction of the vector $(r_1 - r_2)$ and its magnitude is inversely proportional to the cube of the distance between the two bodies.

Applying Newton's second law of motion, we can derive the dynamics of the secondary body. By considering the acceleration of the secondary body as $\frac{d^2 r_2}{dt^2}$, the equation becomes:

$$\frac{d^2 r_2}{dt^2} = -G\frac{m_1}{\|r_2 - r_1\|^3}(r_2 - r_1)$$

This equation describes the motion of the secondary body under the gravitational influence of the primary body.

In the context of space missions, we often encounter scenarios where one of the bodies is a planet or a large celestial object, and the other body is a satellite or a spacecraft with a much smaller mass compared to the planet. In such cases, we can neglect the influence of the satellite on the planet and consider the motion of the satellite relative to the planet.

To incorporate the effect of satellite propulsion, we introduce a control term u that represents the propulsive force exerted by the satellite. The acceleration of the satellite is then given by εu, where ε is a parameter that accounts for the magnitude of the propulsive force relative to the gravitational force.

By rewriting the equation of motion for the secondary body with the inclusion of the control term, denoting the relative position vector as $r = r_2 - r_1$ and relative velocity v, we obtain:

$$\begin{cases} \dfrac{\mathrm{d}\, r}{\mathrm{d}\, t} = v \\ \dfrac{\mathrm{d}\, v}{\mathrm{d}\, t} = -\dfrac{\mu}{\|r\|^3} r + \varepsilon\, u \end{cases} \tag{1.4}$$

where $\mu = G(m_1 + m_2)$. This equation represents the motion of the satellite relative to the planet in the presence of both gravitational and propulsive forces.

An interesting property of this equation is that when the control term u is zero, the motion of the satellite follows a Keplerian trajectory that is a conic section. When the initial state is such that the mechanical energy of the system is negative, the trajectory is a periodic elliptical orbit. In this work, we are interested in perturbations of such orbits.

Equation (1.4) can be expressed in different coordinate systems, allowing for the parametrization of various planet-centered periodic orbits. Integrals of motion derived from Equation (1.4) when $u = 0$ provide valuable insights into

the characteristics of these orbits and enable the exploitation of perturbations techniques.

1.3.2 Integrals of motion of the two-body problem

Kepler's problem is superintegrable, so that it is characterized by five integrals of motions. A vectorial representation of these constants is offered by Milankovitch elements, which consist of the specific angular momentum $h = r \times v$ and the eccentricity vector $e = \frac{1}{\mu}(v \times h) - \frac{r}{\|r\|}$, , where v denotes the velocity vector. This representation yields valuable geometric insight and no singularity, but it is redundant since the two vectors are constrained to be orthogonal. The magnitude of the eccentricity vector gives us the eccentricity of the orbit. If $\|e\| = 0$, the orbit is circular, and as $\|e\|$ approaches 1, the orbit becomes more elongated. To simplify the notation and avoid confusion, we will introduce a scalar notation for eccentricity. From now on, we denote the magnitude of eccentricity as e, which is defined as the norm or magnitude of the eccentricity vector $e := \|e\|$.

Among various representations of elliptic orbits based on integrals of motion, classical Keplerian elements are arguably the most popular choice. They consists of semi-major axis $a = \frac{|h|^2}{\mu(1-e^2)}$, eccentricity, and three angles orienting the orbital plane and perigee in space, namely the longitude of the ascending node, the orbital inclination, and the argument of periapsis. These elements are singular for circular and equatorial orbits. By calculating these elements, we obtain a complete description of the satellite's orbit in terms of its shape, orientation, and position relative to the central body. However, to fully describe the state of the satellite, an additional element is required. In this study, our primary utilization involves the true anomaly $f \in \mathbb{S}^1$.

In this work, we introduce a set of Keplerian-like orbital elements, which leverages on the axial symmetry of the problem with respect to the Sun's direction. To this purpose, consider a reference frame $\mathcal{S}$ with origin at the center of the planet, $\hat{X}$ axis towards $\hat{s}$, $\hat{Y}$ lies in the plane of the planet's orbit around the Sun and is orthogonal to $\hat{X}$, and $\hat{Z}$ is chosen to form a right-hand frame. Figure 1.5 represents the vectors h, e and $\hat{N}$, which denote the angular momentum, eccentricity and ascending node vectors respectively. Let γ_1, γ_2, γ_3 be Euler angles orienting the eccentricity vector according to a X-Y-X rotation as depicted in Figure 1.5, so that γ_2 is the angle between the angular momentum of the orbit and the Sun direction, and γ_3 is the argument of periapsis with respect to the reference plane orthogonal to the Sun's direction. Hence, the set of elements that we use consists of $\gamma_1, \gamma_2, \gamma_3, a, e, f$.

Considering the relatively small magnitude of SRP compared to other forces, it is treated as a perturbation in the orbital motion of a satellite. Therefore, the dynamics of the satellite can be described by the Gauss variational equations (GVE), which characterize the variations of orbital parameters caused by external

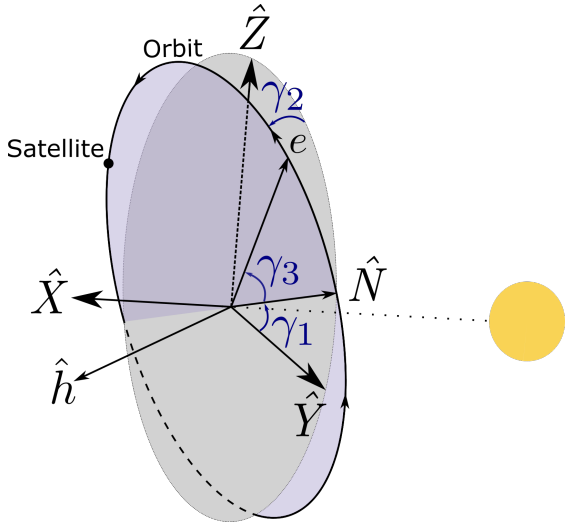

Figure 1.5: Euler angles γ_i orienting the orbit according to a $\hat{X}$-$\hat{Y}$-$\hat{X}$ rotation with respect to the reference frame $\mathcal{S}$. Here, h and e denote the angular momentum and eccentricity vectors.

perturbations. The GVE provide a mathematical framework to model the effect of SRP on the satellite's orbit and predict its evolution over time. Let us denote $I = (\gamma_1, \gamma_2, \gamma_3, a, e)^T \in \mathcal{M}$ the slow state, since its variation over one period of f is considered small. Here, $\mathcal{M}$ denotes a set of elliptic orbits in the chosen coordinates, whose topology is a subset of $\mathbb{R}^5$. Thus, dynamics of the system $(I, f) \in \mathcal{M} \times \mathbb{S}^1$ subject to a perturbation u is given by GVE:

$$\begin{cases} \dfrac{\mathrm{d}\, I}{\mathrm{d}\, t} = \varepsilon \sqrt{\dfrac{a\,(1-e^2)}{\mu}} G(I,f)\, R(I,f)\, u \\ \dfrac{\mathrm{d}\, f}{\mathrm{d}\, t} = \omega(I,f) + \varepsilon\, G_f(I,f)\, R(I,f)\, u \end{cases} \tag{1.5}$$

where components of $u \in U$ are in the reference frame $\mathcal{S}$,

$$R(I,f) = R_X(\gamma_3 + f) R_Y(\gamma_2) R_X(\gamma_1)$$

is the rotation matrix from $\mathcal{S}$ to local-vertical local-horizontal frames[12], $\omega(I,f)$, $G_f(I,f)$ and $G(I,f)$ are given by

$$\omega(I,f) = \sqrt{\frac{\mu}{a\,(1-e^2)^3}} (1 + e\cos f)^2,$$

[12]Here, $R_A(\varphi)$ denotes the rotation matrix of angle φ about the axis $\hat{A}$.

$$G(I,f) = \begin{pmatrix} 0 & 0 & \dfrac{\sin(\omega+f)}{\sin i\ (1+e\cos f)} \\ 0 & 0 & \dfrac{\cos(\omega+f)}{1+e\cos f} \\ -\dfrac{\cos f}{e} & \dfrac{2+e\cos f}{1+e\cos f}\dfrac{\sin f}{e} & \dfrac{\cos(\omega+f)}{1+e\cos f} \\ \dfrac{2\,a\,e}{1-e^2}\sin f & \dfrac{2\,a\,e}{1-e^2}(1+e\cos f) & 0 \\ \sin f & \dfrac{e\cos^2 f+2\cos f+e}{1+e\cos f} & 0 \end{pmatrix}$$

$$G_f(I,f) = \begin{pmatrix} \dfrac{\cos f}{e} & -\dfrac{2+e\cos f}{1+e\cos f}\dfrac{\sin f}{e} & 0 \end{pmatrix}$$

GVE will be used especially for controllability analysis and optimal control of solar sails, when a satellite orbiting around a planet or an asteroid is studied.

1.3.3 Circular restricted three-body problem

The restricted three-body problem studies the motion of a particle subject to the interactions with two celestial bodies with masses m_1 and m_2, *e.g.*, Sun and Earth. By particle, we mean an object with negligible mass compared to m_1 and m_2. To simplify the analysis, we assume that the relative orbit between the two attractors is circular. A non-inertial frame is attached to the center of mass of the two celestial bodies, as illustrated in Figure 1.6. The third body in this system represents the spacecraft. Such a configuration is called CRTBP. To facilitate the analysis, it is common to normalize the time and length units. This is achieved by choosing a length unit equal to the distance between the centers of mass of the two attractors, and a time unit such that the binary orbit has period 2π. In the synodic frame, the position of the two massive bodies are thus $(-\eta, 0, 0)$ and $(1-\eta, 0, 0)$, respectively, where η is the mass ratio given by

$$\eta = \frac{m_2}{m_1 + m_2}.$$

Position and velocity of the spacecraft are denoted by $r = (r_x, r_y, r_z)$ and $v = (v_x, v_y, v_z)$, respectively. The state of the spacecraft is described by the vector $x = (r_x, r_y, r_z, v_x, v_y, v_z)$. Additionally, the thrust exerted by the spacecraft is denoted as εu, where ε represents a small parameter related to the magnitude of the thrust and u is the control input. Thus, the controlled motion of the spacecraft in this three-body system is described by a control-affine dynamical system, which

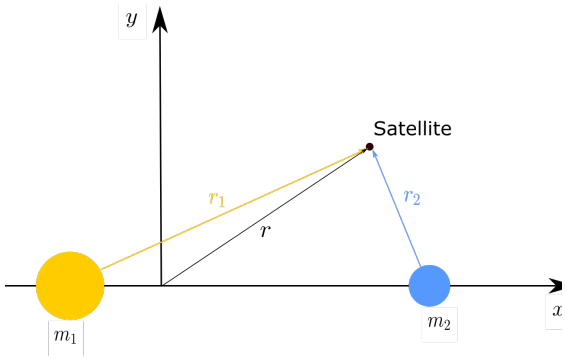

Figure 1.6: Circular restricted three-body problem configuration.

takes into account the gravitational forces exerted by the two masses and the control force, namely

$$\frac{\mathrm{d}\,x}{\mathrm{d}\,t} = f(x) + \varepsilon B u, \qquad x \in \mathbb{R}^6, \qquad u \in U \tag{1.6}$$

Here, $f(x)$ denotes the drift of the CRTBP, namely

$$f(x) = \begin{pmatrix} v_x \\ v_y \\ v_z \\ \left(-\frac{1-\eta}{\|r_1\|^3} - \frac{\eta}{\|r_2\|^3} + 1\right) r_x - \left(\frac{1}{\|r_1\|^3} - \frac{1}{\|r_2\|^3}\right)(1-\eta)\eta + 2v_y \\ \left(-\frac{1-\eta}{\|r_1\|^3} - \frac{\eta}{\|r_2\|^3} + 1\right) r_y - 2v_x \\ \left(-\frac{1-\eta}{\|r_1\|^3} - \frac{\eta}{\|r_2\|^3}\right) r_z \end{pmatrix}$$

$$B(X) = \begin{pmatrix} 0 & 0 & 0 & 1 & 0 & 0 \\ 0 & 0 & 0 & 0 & 1 & 0 \\ 0 & 0 & 0 & 0 & 0 & 1 \end{pmatrix}^T$$

where $\|r_1\|$ and $\|r_2\|$ are distances between the satellite and the two main bodies:

$$\|r_1\| = \sqrt{(r_x + \eta)^2 + r_y^2 + r_z^2},$$
$$\|r_2\| = \sqrt{(r_x - 1 + \eta)^2 + r_y^2 + r_z^2}.$$

In the context of the CRTBP, there are five equilibrium points known as Lagrange points or libration points. These points are unique locations where the

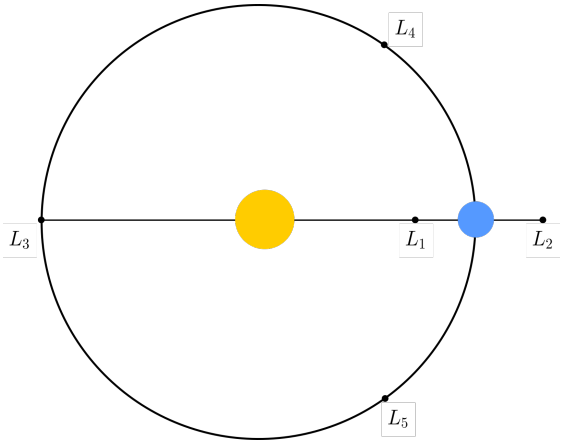

Figure 1.7: Lagrange points of a CRTBP.

combined gravitational forces of two massive bodies create a situation where a third body experiences zero net velocity and acceleration. Consequently, a spacecraft positioned precisely at one of these Lagrange points will maintain a stable position relative to the rotating reference frame. The positions of these Lagrange points can be determined by examining the equations of motion in the CRTBP system. By setting the control input (u) and the derivatives of the state variables ($\dot{x}$, $\dot{y}$, $\dot{z}$, $\ddot{x}$, $\ddot{y}$, $\ddot{z}$) to zero in the governing equations given by Equation (1.6), we can identify the points where the spacecraft experiences zero net acceleration. Figure 1.7 illustrates the locations of the Lagrange points in a CRTBP system. These points are denoted as L_1, L_2, L_3, L_4, and L_5. Each Lagrange point has specific geometric properties and characteristics. For instance, L_1, L_2, and L_3 are collinear with the two massive bodies, while L_4 and L_5 form an equilateral triangle with L_3.

The Lagrange points and their vicinity offer the presence of periodic orbits, such as the Halo orbits, Lyapunov orbits, and other families of orbits. These orbits are of particular interest, especially for observation missions and scientific exploration. As an example, the JWST is located in a Halo orbit around the L_2 Lagrange point, allowing it to maintain a stable position and conduct its observations effectively. These Lagrange points and their associated orbits provide valuable opportunities for space missions to study celestial objects and conduct various scientific investigations.

Chapter 2

Controllability of solar sails

Trajectory design and station-keeping of solar sails about a celestial body can be formulated as control problems with positivity constraints. Specifically, for a non-ideal sail model, the force generated by the solar radiation pressure is contained in a pointed convex cone of revolution with the axis in the sun–satellite direction. Therefore, classical approaches to infer controllability based on the Lie algebra rank condition do not apply to these problems. This study offers a novel condition to decide on controllability of control systems with positivity constraints. Both global and local results are given in this work. The proposed condition is effective because it can be verified by solving an auxiliary convex optimization problem for which reliable numerical methods are available. A crucial ingredient of this approach is the theory of positive trigonometric polynomials. The practical interest of this condition is the assessment of a minimum requirement on the optical properties of the sail, which may be of use for mission design purposes. This chapter is based on four papers. The first one, [9], details theoretical results on controllability for general cone-constrained controlled systems. Second paper, published in Journal of Guidance, Control, and Dynamics, [31], presents the methodology that we propose to verify controllability condition of solar sails. Finally, two conference papers, one presented at the European Control Conference in 2022 [30], and the second at the 9th International Conference on Astrodynamics Tools and Techniques in 2023 [32], further investigates numerical verification of the proposed condition for solar sails and other system, expanding the results beyond Keplerian orbits.

Introduction

A major difficulty in assessing the controllability of an SRP-actuated system is that the sail cannot generate a force with a positive component toward the direction of the Sun, so that classical tools of geometric control theory cannot be used. Most known controllability sufficient conditions assume that the vector fields are bracket generating (full rank of the distribution spanned by the Lie algebra they generate), which is indeed necessary, and prove controllability under an additional assumption on the drift vector field; this occurs, for instance if the drift vector field is zero [38], or if all orbits of the drift vector field are periodic, or if the drift vector field is Poisson stable [3]. See also textbooks like [34] or [1]. These results however require that zero belongs to the interior of the convex hull of U. The requirement in terms of the Lie brackets is shown to be verified by solar sails, unless a fully absorptive surface model of the sail is considered. However, the control set is not a neighborhood of the origin, since negative controls can not be generated. This aspect is particularly critical when considering a non-ideal sail model, for which the sail is assumed to be flat but not perfectly reflective. In this case the control set is contained inside a strictly convex cone of revolution, whose angle depends on the optical properties of the sail.

Solar sails are just a particular example of non-linear systems with periodical drift vector field and whose controls are constrained to a convex set that contains the origin, but is not necessary a neighborhood of zero. The present chapter investigates controllability in the case where zero is in U, but is not contained in the interior of its convex hull (the results are still valid if U happens to be a neighborhood of zero, but would be obtained in a simpler way from known results in that case). This chapter proposes a novel sufficient condition to asses local controllability in prescribed time of such a system, relying on periodicity of its orbits. It is important to emphasize that the formulated condition is applicable for any system satisfying the aforementioned control constraints. Once the sufficient condition for local-controllability is proposed, another result gives a condition for certification of local non-controllability of a system. In other words, the condition implies that the system is not locally controllable in the prescribed time and, consequently, there exist a non-reachable half-space of neighborhood of its state vector.

Second contribution of the chapter consists in a controllability check for non-ideal sails in planet-centered orbits. This requirement is aimed at assessing whether a non-ideal solar sail with given optical parameters is capable of decreasing or increasing all possible functions of the Keplerian integrals of motion (*e.g.* Keplerian or equinoctial orbital elements) over an orbital period. In other words, we propose a methodology allowing to verify if a solar sail can change the geometry and orientation of an orbit in any arbitrary way given its optical properties. Given some physical parameters, a convex cone containing all possible directions of the

SRP force is first defined. Then, the necessary controllability condition that we propose is verified by means of a worst-case optimization problem characterized by a finite number of design variables and a two-parameter family of inequality constraints, namely, the clock angle of the convex cone associated to the control set and the true anomaly of the sail. Numerical solution of this semi-infinite problem is achieved by leveraging on the formalism of squared functional systems [44, Chap. 17][22, Chap. 3] and on the trigonometric nature of GVE to exactly enforce inequality constraints for all values of the true anomaly and clock angle. No discretization is performed to solve the problem numerically. Eventually, the semi-infinite problem is recast into a finite-dimensional convex programming problem with a finite number of linear matrix inequalities (LMI) and an unique, well-defined solution. Non-satisfaction of the condition entails local non-controllability of the system for the given value of the cone angle (and, consequently, of the optical properties) and orbital conditions. Hence, a fine numerical analysis covering the entire phase space of orbital elements is carried out to determine the minimum cone angle for a large range of orbits. It is shown that a universal (namely, planet-independent) minimum cone angle exists that satisfies the condition for all orbits. Its value is about 60 degrees (note that 0 and 90 degrees correspond to fully-absorptive and perfectly-reflective sails, respectively). The result suggests that the sail does not necessary have to be ideal to satisfy the requirement. The methodology is based only on the conical hull of the control set, regardless of the specific source of non-ideality of the sail (e.g., specular reflection, diffuse reflection, or re-emitted radiation [40, Chap. 2]). This result can be used to provide insight into the controllability of the sail during its lifetime, owing to the degradation of its optical properties discussed in [21], and may support the design of real-life missions by serving as a minimal requirement to be satisfied.

After giving the results on solar sailing, we propose to generalize the giving methodology for any periodical orbit and for any type of satellites with conical constraints on the thrust directions. This results can be used for design of a station-keeping mission around any periodical orbit.

2.1 Partial state of the art on controllability of nonlinear systems

2.1.1 Notations and definitions

Consider a nonlinear control-affine system :

$$\dot{x} = F_0(x) + u_1 F_1(x) + \cdots + u_m F_m(x), \quad u = (u_1, ..., u_m) \in U, \tag{2.1}$$

with $x \in M$, where M is a smooth manifold[1] of dimension n, the control set U is a subset of $\mathbb{R}^m$, the vector field F_0 is the drift of the system and the vector fields F_i, $1 \leq i \leq m$ are the control vector fields.

Definition 2 (Local controllability along a trajectory [17]). *Let $(\bar{x}, \bar{u}) : [t_0, t_1] \longrightarrow M \times \mathbb{R}^m$ be a trajectory of the control system (2.1). The control system is locally controllable along the trajectory $(\bar{x}, \bar{u})$ if, for every $\varepsilon > 0$, there exists $\eta > 0$ such that, for every $(a, b) \in \mathbb{R}^n \times \mathbb{R}^n$ with $|a - \bar{x}(t_0)| < \eta$ and $|b - \bar{x}(t_1)| < \eta$, there exists a trajectory $(x, u) : [t_0, t_1] \longrightarrow M \times \mathbb{R}^m$ such that*

$$x(t_0) = a, x(t_1) = b,$$
$$|u(t) - \bar{u}(t)| \leq \varepsilon, t \in [t_0, t_1].$$

Two particular cases are when the reference trajectory is either an equilibrium point or a periodic trajectory, so that $\bar{x}(t_0) = \bar{x}(t_1) = a$ and the property is about joining pair of points in a neighborhood of a. The general property around a trajectory of reference is used in [9, Section 3] or [31, 32]. Note that local properties of this kind are both weaker and stronger that global controllability: the latter is stronger because it requires that any two points in the state space can be joined, while the former has stronger requirements on the transfer time (one period if we work around a periodic solution) and on the control (close to the reference control).

Definition 3 (Global controllability [17]). *The control system (2.1) is globally controllable, if and only if for every $(a, b) \in \mathbb{R}^n \times \mathbb{R}^n$ there exists t_0, t_1 and $u \in L^\infty((t_0, t_1); \mathbb{R}^n)$ such that the solution of system*

$$\dot{x} = F_0(x) + u_1 F_1(x) + \ldots + u_m F_m(x), \; x(t_0) = a,$$

satisfies

$$x(t_1) = b$$

and $u(t)$ in U for t in $[t_0, t_1]$.

A classical approach to study controllability of these systems is to evaluate Lie brackets of the vector fields. Before its statement, let us introduce some notations.

Definition 4 (Lie brackets). *Consider two smooth vector fields F_1 and F_2. The Lie bracket of F_1 and F_2 is another smooth vector field denoted $[F_1, F_2]$. Considering vector fields as first order differential operators, one has:*

$$[F_1, F_2] = F_1 F_2 - F_2 F_1.$$

[1] It can be the whole $\mathbb{R}^n$ or an open subset, or a more general object which is diffeomorphic to an open subset of $\mathbb{R}^n$ locally (*i.e.* via local coordinates) but not globally, in general; an example of such M can be a sphere, or a torus, or the set of elliptic orbits in the Kepler problem, as defined in Chapter 1, where local coordinates are orbital elements, so there are many possible choices of such coordinates, well known not to parametrize *all* elliptic orbits. Notions from differential geometry like manifolds, vector fields, Lie brackets, and classical manifolds like projective spaces are used in this thesis without re-defining them, we refer to classical textbooks like [59, Volume 1].

Using local coordinates, and if F_1 and F_2 are given by

$$F_1 = F_1^i \frac{\partial}{\partial x^i}, \quad F_2 = F_2^i \frac{\partial}{\partial x^i},$$

the formula for $[F_1, F_2]$ is:

$$[F_1, F_2] = \sum_{i,j} \left(F_1^i \frac{\partial F_2^j}{\partial x^i} - F_2^i \frac{\partial F_1^j}{\partial x^i} \right) \frac{\partial}{\partial x^j}.$$

Definition 5 (Lie algebra rank condition (LARC))**.** *The so called Lie algebra rank condition requires the rank of the vector space generated by the vector fields of the system themselves and their Lie brackets to be equal to the dimension of the state space at all points.*

The LARC is necessary for controllability, at least in the real analytic case, but sufficiency requires additional conditions.

2.1.2 An example: non-controllability of a perfectly absorptive solar sail

Although we will not study it further, let us apply the Lie brackets technique to the perfectly absorptive model, and show its non-controllability. Consider System (1.4). If a perfectly absorptive model of the sail is studied, *i.e.* $\rho = 0, B_b = B_f = 0$, optical coefficients are $b_1 = 1, b_2 = 0, b_3 = 0$. Thus, the force is $f_{SRP} = \varepsilon \cos\beta \hat{s}$, leading to the control term aligned with the solar vector:

$$u = \cos\beta \hat{s}$$

For Lie brackets computation, only directions of vector fields matter. Thus, by putting System (1.4) for a perfectly reflective sail under form of Equation (2.1) we come up with vector fields given by

$$F_0 = v_x \frac{\partial}{\partial r_x} + v_y \frac{\partial}{\partial r_y} + v_z \frac{\partial}{\partial r_z} - \frac{r_x}{\|r\|^3} \frac{\partial}{\partial v_x} - \frac{r_y}{\|r\|^3} \frac{\partial}{\partial v_y} - \frac{r_z}{\|r\|^3} \frac{\partial}{\partial v_z}$$
$$F_1 = s_x \frac{\partial}{\partial v_x} + s_y \frac{\partial}{\partial v_y} + s_z \frac{\partial}{\partial v_z},$$

where $r = (r_x, r_y, r_z)$, $v = (v_x, v_y, v_z)$ and $\hat{s} = (s_x, s_y, s_z)$. For notation purposes only, let us denote the vector fields:

$$v\frac{\partial}{\partial r} = v_x \frac{\partial}{\partial r_x} + v_y \frac{\partial}{\partial r_y} + v_z \frac{\partial}{\partial r_z}, \qquad s\frac{\partial}{\partial v} = s_x \frac{\partial}{\partial v_x} + s_y \frac{\partial}{\partial v_y} + s_z \frac{\partial}{\partial v_z}$$
$$\frac{r}{\|r\|^3}\frac{\partial}{\partial v} = \frac{r_x}{\|r\|^3}\frac{\partial}{\partial v_x} + \frac{r_y}{\|r\|^3}\frac{\partial}{\partial v_y} + \frac{r_z}{\|r\|^3}\frac{\partial}{\partial v_z}$$
$$F_{sr} = s\frac{\partial}{\partial r},\ F_{rr} = r\frac{\partial}{\partial r},\ F_{vr} = v\frac{\partial}{\partial r},\ F_{sv} = s\frac{\partial}{\partial v},\ \ldots$$

Finally, by denoting $\hat{s} \cdot r$ a scalar product of two vectors $\hat{s}$ and r, computation of Lie brackets gives the following results:

$$F_0 = v\frac{\partial}{\partial r} - \frac{r}{\|r\|^3}\frac{\partial}{\partial v} = F_{vr} - \frac{1}{\|r\|^3}F_{rv}; \qquad F_1 = s\frac{\partial}{\partial v} = F_{sv};$$

$$F_{01} = \Big[F_0, F_1\Big] = -F_{sr};$$

$$F_{001} = \Big[F_0, [F_0, F_1]\Big] = \frac{3\,(\hat{s}\cdot r)}{r^5}\,F^{rv} - \frac{F^{sv}}{\|r\|^3};$$

$$F_{101} = \Big[F_1, [F_0, F_1]\Big] = 0$$

$$\begin{aligned} F_{0001} = \Big[F_0, [F_0, [F_0, F_1]]\Big] &= \frac{1}{\|r\|^3}F_{sr} + \frac{3(v\cdot r)}{\|r\|^5}F_{sv} \\ &+ \Big(\frac{3(\hat{s}\cdot v)}{\|r\|^5} - \frac{15(\hat{s}\cdot r)(v\cdot r)}{\|r\|^7}\Big)F_{rv} \\ &+ \frac{3(\hat{s}\cdot r)}{\|r\|^5}(F_{vv} - F_{rr}) \end{aligned}$$

All subsequent iterations are linear combinations of the previous vector fields. Thus, Lie brackets of System (1.4) when a perfectly absorptive sail is considered, generate only 5 independent vector fields if $\hat{s} \cdot r \neq 0$:

$$F^{sr},\ F^{sv},\ F^{rv},\ F^{vr},\ F^{vv} - F^{rr}\,.$$

Dimension of the state being equal to 6, the System is not bracket generating, according to LARC. Moreover, rank deficiency implies that an integral of motion exists, which happens to be the projection of the angular momentum h towards $\hat{s}$, namely $\hat{s} \cdot h = \hat{s} \cdot (r \times v) = \det(r, v, \hat{s})$. In fact, Lie derivative of $\hat{s} \cdot h$ with respect to the controlled vector field F_1 is:

$$\begin{aligned} L_{F_1}(\det(r,v,\hat{s})) &= s_x\frac{\partial}{\partial v_x}\det(r,v,\hat{s}) + s_y\frac{\partial}{\partial v_y}\det(r,v,\hat{s}) + s_z\frac{\partial}{\partial v_z}\det(r,v,\hat{s}) \\ &= s_x(-r_y s_z + r_z s_y) + s_y(r_x s_z - r_z s_x) + s_z(-r_x s_y + r_y s_x) \\ &= 0 \end{aligned}$$

Lie derivative of a tensor field denotes its change along the flow defined by a vector field. Given that $L_{F_1}(\hat{s} \cdot h) = 0$ and $L_{F_0}(\hat{s} \cdot h) = 0$, it demonstrates that $\hat{s} \cdot h$ is constant along any solution for any control.

Computation of Lie brackets shows that LARC does not hold for a perfectly absorptive sail with $\rho = 0$, in which case an integral of motion exists. Nevertheless, it is an over-conservative solar sail model and not very relevant for our study, since we are interested in real-life sails.

2.1.3 Classical results on controllability

The following theorem gives classical conditions considered to study controllability of periodical systems.

Theorem 6 ([3]). *System* (2.1) *is globally controllable if*
(i) *the vector field* F_0 *is Poisson stable,*
(ii) *the family* $\{F_0, F_1, \ldots, F_m\}$ *is bracket generating, and*
(iii) *the convex hull of the control set* U *is a neighborhood of* 0 *in* $\mathbb{R}^m$.

is stated precisely in this form in the recent textbook [34] (Chapter 4, Theorem 5) or in the original reference, that mentions techniques due to [35]. It has been rather widely used, for instance to prove controllability prior to solving an optimal control problem, see *e.g.* [11].

Recall that, for a complete vector field F_0 on M, a point $x \in M$ is said to be (positively) *Poisson stable* for F_0 if there exists a sequence of positive times $(t_n)_n \to \infty$ such that $\exp(t_n F_0)(x) \to x$ when $n \to \infty$, and the vector field itself is said to be Poisson stable if there is a dense subset of such points. It turns out that many physical dynamical systems have this property; this makes the following result quite useful.

We suppose that (i) holds. For the solar sailing example, even a stronger assumption of F_0 being periodical with period 2π can be used. Once we assume (ii) for a realistic solar sail (not a perfectly absorptive model), we investigate the condition (iii) which fails, zero being the boundary of U, typically the case where U is included in a non trivial convex cone with vertex at the origin, strictly convex at the origin. These positivity constraints come naturally in many physical systems, not only solar sails, see *e.g.* [32]. This situation may of course defeat controllability, as evidenced by a very simple academic example of the form of System (1.5) with $I \in \mathcal{M} = \mathbb{R}$ and one scalar control u: $\dot{I} = \varepsilon\, u$, $\dot{f} = 1$, $u \in U \subset \mathbb{R}$; conditions (i) and (ii) are satisfied; if $U = [-1, 1]$, (iii) is also satisfied and controllability trivially holds, while it cannot if $U = [0, 1]$ because I cannot decrease.

Here, we are interested in systems where the origin is rather *on the boundary* of U, as in the solar sailing case, see Figure 1.4. To the best of our knowledge, controllability of such systems is not covered in the literature; it is surprising that this setting is rarely considered. We establish a new sufficient condition (Theorem 7) where an additional condition given by Equation (2.2) is required.

2.2 Novel sufficient condition for global controllability of nonlinear systems with conical constraints on the control set

Consider System (2.1) and the associated vector fields $F_0, \ldots, F_m$ on M. Assume that all solutions of $\dot{x} = F_0(x)$ are periodic in time and $T(x)$ denotes

the minimal period of F_0.

Theorem 7. *Assume the conditions (i) to (iii) hold:*
(i) the LARC holds, i.e. $\{F_0, F_1, \ldots, F_m\}$ is bracket generating, at all x in M ,
(ii) the control set U contains the origin, and
(iii) for all $x \in M$,

$$\operatorname{cone}\left(\left\{\sum_{i=1}^{m} u_i \left(\exp(-tF_0)_\star F_i(x)\right),\ u \in U,\ t \in [0, T(x)]\right\} \cup \{F_0(x)\}\right) = T_x M \tag{2.2}$$

where $\exp(-t\,F_0)_\star F_i$ denotes the pushforward[2] *of the vector field F_i by the diffeomorphism $\exp(-t\,F_0)$ and for a set A, $\operatorname{cone}(A)$ is the smallest convex cone containing A. Then, System (2.1) is globally controllable in sens of Definition 3, meaning that for any x_0 and x_1 in M , there is a time $T \geq 0$ and a measurable control $u(.) : [0, T] \to U$ that drives x_0 to x_1.*

Proof. As in [1, Chapter 8] or [34, Chapter 3], we associate to the vector fields $F_0, \ldots, F_m$, the family

$$\mathcal{G} = \{\, F_0 + u_1 F_1 + \cdots + u_m F_m\,,\ (u_1, \ldots, u_m) \in U\}$$

made of all the vector fields obtained by fixing in (2.1) the control to a constant value that belongs to U. We denote by $\mathcal{A}_\mathcal{G}(x)$ the accessible set from x of this family of vector fields in all positive (unspecified) time, *i.e.*, the set of points that can be reached from x by following successively the flow of a finite number of vector fields in $\mathcal{G}$, each for a certain positive time, which is the same as the set of points that can be reached, for the control System (2.1), with piecewise constant controls. Our goal is to show that , under our assumptions, $\mathcal{A}_\mathcal{G}(x)$ is the whole manifold M for any x, which implies controllability.

Define the families $\mathcal{G} \subset \mathcal{G}_1 \subset \mathcal{G}_2 \subset \mathcal{G}_3$ as follows:

$$\begin{aligned}
\mathcal{G}_1 &= \mathcal{G} \cup \{-F_0\}\,,\\
\mathcal{G}_2 &= \{\exp(t\,F_0)_\star X\,,\ X \in \mathcal{G}_1,\, t \in \mathbb{R}\}\,,\\
\mathcal{G}_3 &= \operatorname{cone}(\mathcal{G}_2)\ ,
\end{aligned}$$

where $\operatorname{cone}(\mathcal{G}_2)$ denotes the family made of all vector fields that are linear combinations of the form $\sum_k \lambda_k X_k$ with each X_k in $\mathcal{G}_2$ and each λ_k a nonnegative number, $k \in \mathbb{N}$ (conic combination). One has, for all x,[3]

$$\mathcal{A}_{\mathcal{G}_1}(x) = \mathcal{A}_\mathcal{G}(x) \tag{2.3}$$

because on the one hand condition (ii) implies $F_0 \in \mathcal{G}$, and on the other hand, for any $x \in M$,

$$\exp(-t\,F_0)(x) = \exp\big((-t + k\,T(x))\,F_0\big)(x)$$

[2] If X is a vector field and φ a diffeomorphism, we denote as usual $\varphi_\star X(x) = \varphi'(\varphi^{-1}(x))X(\varphi^{-1}(x))$.

for all positive integers k, but for fixed t and x,$-t+k\,T(x)$ is nonnegative for k large enough. Since F_0 and $-F_0$ now belong to $\mathcal{G}_1$, we have $\exp(t\,F_0)(x) \in \mathcal{A}_{\mathcal{G}}(x)$ for all x in M and all t in $\mathbb{R}$, hence $\exp(t\,F_0)$ is according to [34, Chapter 3, Definition 5 and next Lemma] a "normalizer" of the family $\mathcal{G}_1$: by virtue of Theorem 9 in the same chapter of the same reference, this implies that[3]

$$\mathcal{A}_{\mathcal{G}_2}(x) \subset \overline{\mathcal{A}_{\mathcal{G}_1}(x)} \tag{2.4}$$

where the overline denotes topological closure (for the natural topology on M). Now, [1, Corollary 8.2] or [34, Chapter 3, Theorem 8(b)] tell us that[3]

$$\mathcal{A}_{\mathcal{G}_3}(x) \subset \overline{\mathcal{A}_{\mathcal{G}_2}(x)}\,. \tag{2.5}$$

Now, condition (iii) implies that $\mathcal{G}_3(x) = T_xM$ for all $x \in M$, and this in turn implies that $\overline{\mathcal{A}_{\mathcal{G}_3}(x)} = M$. Together with (2.4)-(2.5), this implies

$$\overline{\mathcal{A}_{\mathcal{G}}(x)} = M,$$

and finally from condition (i) and by virtue of Krener theorem [1, Theorem 8.1], 2.2 implies that

$$\mathcal{A}_{\mathcal{G}}(x) = M.$$

□

Remark 8 (Localization)**.** *Assume that (i) holds everywhere but (iii) is only known to hold at* one *point $x \in M$. Then it also holds at all points in some neighborhood O of x, hence all the assumptions of Theorem 7 hold with M replaced with O, hence controllability holds on O. Localization in general of theorems in the style of [34, Theorem 5, Chapter 4] would only hold on a set that is invariant under the flow of the drift vector field, which is structurally the case of O here. Note that no additional requirement with respect to the control vector fields (in particular completeness) is needed.*

According to Remark 8, we have also proved local controllability. See also [9] for more details.

Condition (iii) is more difficult to check than computing Lie brackets and checking the rank of a family of vector fields. Nevertheless, we propose a numerical methodology verifying the global controllability condition in Section 2.4.4.

[3] In the terminology of [1, Section 8.2], one could state (2.3), (2.4) and (2.5) as: $-X^0$ is compatible with $\mathcal{G}$, the vector fields in $\mathcal{G}_2$ are compatible with $\mathcal{G}_1$, and the vector fields in $\mathcal{G}_3$ are compatible with $\mathcal{G}_2$, respectively.

Reformulation in fast-oscillating coordinates (I, f)

Motivated by the main application of this thesis, which is solar sails, we would like to propose a reformulation of the previous condition (iii) using fast-oscillating coordinates, that can correspond to the orbital elements, following the example of System (1.5). Consider a system with the state $(I, f) \in \mathcal{M} \times \mathbb{S}^1$, the control $u \in U$, where I denotes the slow state vector and f is the fast-oscillating variable:

$$\begin{cases} \dfrac{\mathrm{d}\, I}{\mathrm{d}\, t} = \displaystyle\sum_{i=1}^{m} u_i F_i(I, f) \\ \dfrac{\mathrm{d}\, f}{\mathrm{d}\, t} = \omega(I, f) \end{cases}$$

Here, $F_0 = \omega(I, f)\, \partial/\partial f$ is the drift of the system periodical in f of a period $\int_0^{2\pi} \frac{\mathrm{d}f}{\omega}$, and we use the same notation F_i, $1 \leq i \leq m$, for both the smooth map $\mathcal{M} \times \mathbb{S}^1 \to T\mathcal{M}$ and for the vector field on $\mathcal{M} \times \mathbb{S}^1$ whose projections on the first and second factor of the product are respectively that smooth map and zero. Note that this system intends to be a special occurence of the previous one with $x = (I, f)$; the same notation F_i is used here with a different meaning, without possible confusion since we now on work only in the special setting where the state variables are separeted into $x = (I, f)$, with I constant along the periodic solutions of the drift, that are parameterized by the angle f.

Theorem 9. *Let us assume that System 2.2 satisfies conditions (i)-(ii) of Theorem 7. If, additionally, for any $I \in \mathcal{M}$, there does not exist a nonzero co-vector $p_I \in T_I^*\mathcal{M}$ such that*

$$\left\langle p_I,\ \sum_{i=1}^{m}\ u_i F_i(I, f) \right\rangle \geq 0, \qquad f \in \mathbb{S}^1,\ u \in \operatorname{cone} U,\ \|u\| = 1\,,$$

then System (2.1) *is globally controllable.*

Theorem 9 is equivalent to the condition (iii) of Theorem 7 written in different coordinates, therefore, we are not giving its proof. Here, $\langle \cdot, \cdot \rangle$ denotes duality between co-vectors and vectors (*i.e.* applying a linear form to a vector); note that $u \in U$ from Theorem 7 has been replaced with $u \in \operatorname{cone} U$, $\|u\| = 1$, which is a way to select a nonzero vector in each half-line from the origin containing an element of U; the co-vector p_I represents a linear coordinate function that may only increase at first order.

Global controllability is a strong property that can sometimes result in high requirements for the system design. Taking an example of a solar sail, looking ahead, for different orbital parameters the controllability condition requires high

or less constraints on optical properties of the material used for the satellite's design. For some particular missions, a solar sail can only be constrained to achieve station-keeping around a periodical orbit of reference, without necessarily being able of performing any orbital maneuver. In this case it is more convenient to talk about local controllability, according to Definition 2. In the next section we propose sufficient and necessary conditions for local controllability of such systems.

2.3 Local controllability of systems with conical constraints on the control set

We want to propose a case which clearly contradicts condition (iii) of Theorem 7 or Theorem 9 locally.

Theorem 10. *If, for at least one orbit $I_0 \in \mathcal{M}$, there exists a nonzero co-vector $p_{I_0} \in T^*_{I_0}\mathcal{M}$ such that*

$$\left\langle p_{I_0},\ \sum_{i=1}^{m} u_i F_i(I_0, f) \right\rangle > 0, \qquad f \in \mathbb{S}^1,\ u \in \operatorname{cone} U,\ \|u\| = 1\,, \tag{2.6}$$

then System (2.1) *is not locally controllable along the periodic trajectories with zero control starting from I close to I_0.*

Proof. In a small enough open chart domain around (I_0, p_{I_0}) in the cotangent bundle, under our assumption one can choose coordinates in which the velocity of any admissible curve $I(t)$ starting from I_0 and generated by controls valued in U will lie in the half plane defined by the constant (coordinate) value p_{I_0}:

$$0 \leq \langle p_{I_0}, \dot{I}(t)\rangle = \frac{\mathrm{d}}{\mathrm{d}t}\langle p_{I_0}, I(t)\rangle$$

for small t. As a result, for such times t, in coordinates $\langle p_{I_0}, I(t)\rangle$ remains nonnegative so any admissible curve is confined to some half-space (check Figure 2.1). This clearly defeats local controllability along periodic trajectories (control set to zero) starting from I_0. □

In practice, taking a solar sail as an example, existence of a non-reachable half-space of the neighborhood of the initial condition means that there is a function of the orbital elements (say the semi-major axis) that the sail cannot decrease, or increase, while remaining close to the original orbit (if the thrust is small one period is not long enough to go far).

Orbits in the forbidden half neighborhood might however be reached (*i.e.* global controllability could hold), but only by trajectories that must leave this neighborhood; in practice, this means that the sail we just mentioned could, even

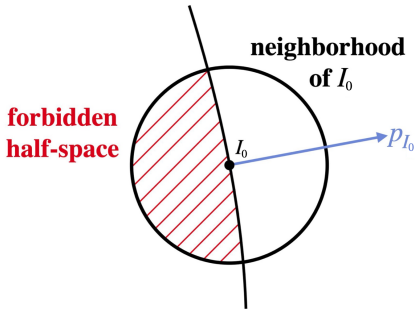

Figure 2.1: Schematic representation of a half-space of the neighborhood of I_0 where motion is (locally) forbidden.

if condition (2.6) holds, be capable of decreasing its semi-major axis, but only at the price of first going "far" from the neighborhood of the initial orbit (by significantly increasing its inclination, for example). For a detailed discussion on the gap between Theorem 10 and the negation of Theorem 7 for general control systems as well as some simple examples of systems satisfying the global controllability property, but not locally controllable, we refer to [9]. Theorem 10 gives a sufficient condition to certify local non-controllability of fast-oscillating systems, whose example are solar sails.

The next section proposes numerical methodology to verify the aforementioned conditions for solar sailing. We also expand the proposed analysis to other types of systems and other scenarios in Section 2.6.

2.4 Numerical methodology for controllability analysis of solar sails

2.4.1 Transformation of the dynamics and convexification of the control set

Condition (i) of Theorem 7 is assumed to be verified for $\rho > 0$. Condition (ii) is satisfied by definition of U. Condition (iii) may be adressed by using Theorem 10. Given some optical properties of the sail and orbital state I, we are interested in determining if Equation (2.6) has any non-trivial solution $p_I \neq 0$. Some manipulations are introduced to facilitate this task. Let us first introduce the following assumptions:

1. Orbital period of the sail is much smaller than the one of the heliocentric orbit of the attractor, so that variations of the Sun direction $\hat{s}$ over a single orbit of the sail are neglected.

2. Solar eclipses are neglected. Targeting a certification of non-controllability,

this assumption is conservative, as controllability can only deteriorate while including eclipses, since no SRP can be generated in the shadow. Eclipses restrain the time period of control of the satellite. As explained later in this section. our results are independent of the semi-major axis of the orbit, which has a major impact on duration of eclipses during the orbital period. Therefore, in order to provide a conservative planet-independent and semi-major-axis-independent result, we suppose the sail being controlled over the whole orbital period.

3. Re-emitted radiation is neglected. In fact, this component of SRP can be reasonably regarded as a disturbance for control purposes.

Consider System (1.5) and orbital parametrization depicted in Figure 1.5. The peculiar choice of Euler angles follows from the symmetry of System (1.5), namely axial symmetry with respect to the axis $\hat{X}$, and it has the main consequence that controllability results are independent of γ_1, which is a rotation about this axis. We also note that $(1 + e\cos f)\, G(I, f)R(I, f)$ is a trigonometric polynomial in f because eclipses were neglected. This has significant advantages for the numerical methodology detailed in Section 2.4.3.

Finally, orbital perturbations (other than SRP) are not included in Equation (1.5) because we are interested in investigating geometric obstructions to the controllability of solar sails regardless of their size.

First, let us denote

$$\tilde{G}(I, f) := (1 + e\cos f)G(I, f)R(I, f).$$

With this notation, the time derivative of I in Equation (2.6) can be replaced as follows:

$$\frac{\mathrm{d}\, I}{\mathrm{d}\, t} = \frac{\varepsilon}{1 + e\cos f}\sqrt{\frac{a\,(1 - e^2)}{\mu}}\tilde{G}(I, f)\, u. \tag{2.7}$$

Because $\dfrac{\varepsilon}{1 + e\cos f}\sqrt{\dfrac{a\,(1 - e^2)}{\mu}}$ is positive, $\tilde{G}(I, f)\, u$ has the same sign as $\dfrac{\mathrm{d}\, I}{\mathrm{d}\, t}$, so that its sign can be studied, instead. The fact that $\tilde{G}(I, f)$ is a second-degree trigonometric polynomial in f offers major benefits when positivity constraints are numerically enforced in Section 2.4.3. This operation has no impact on the sign of Equation (2.6). We also note that System (1.5) is axially symmetric with respect to the Sun-planet direction, since it is independent of γ_1, and that semi-major axis and planetary constant have no impact on the sign of Equation (2.6). Hence, *all outcomes of this controllability study are independent of both the semi-major axis and* γ_1 *(because of symmetry), and they are valid for any attractor*

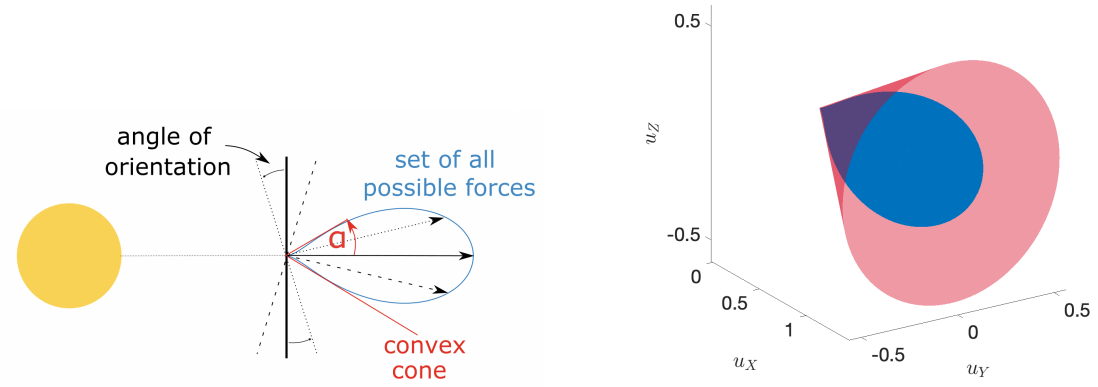

(a) Schematic representation

(b) Three-dimensional representation

Figure 2.2: Approximation of the control set (blue) by a convex cone (red).

(spherical symmetric central body), since magnitude of SRP does not impact the non-controllability condition (which is a geometric obstruction).

Second, the control set U is replaced by its conical hull, $K_\alpha := \text{cone}(U)$, which is a cone of revolution of angle α, as illustrated in Figure 2.2. This approximation makes the problem convex which has a major advantage for numerical computation. Replacing U by K_α has no impact on the closure of the reachable set of the control system.Therefore, non-controllability of the system with controls in K_α implies non-controllability of the system with the original control set, U. Cone angle α can be directly deduced from the optical properties of the sail introduced in Equation (1.1). The relation is obtained by solving:

$$\tan\alpha \;=\; \max_{\beta\in[0,\frac{\pi}{2}]} \frac{\left\|\left(\mathbb{I}-\hat{s}\hat{s}^T\right) f_{SRP}\right\|}{f_{SRP}\cdot\hat{s}} \tag{2.8}$$

The angle β^* solution of Equation 2.8 is [42]

$$\cos\beta^* = \frac{-b_1b_3-2b_2b_3+\sqrt{b_1^2b_3^2-4b_1b_2b_3^2+8b_1^2b_2^2+4b_1b_2^3}}{4b_1b_2+2b_2^2}. \tag{2.9}$$

Thus, angle α of the convex cone can be retrieved from the critical angle β^*:

$$\tan\alpha = \frac{(b_3+b_2\cos\beta^*)\sin\beta^*}{b_1+b_2\cos^2\beta^*+b_3\cos\beta} \tag{2.10}$$

If $B_f = 0$ and we neglect the thermal radiation force, Equation (2.8) simplifies to

$$\alpha(\rho,s) = \tan^{-1}\left(\frac{\rho\,s}{\sqrt{1-\rho^2\,s^2}}\right), \qquad \rho\,s = \frac{\tan\alpha}{\sqrt{1+\tan^2\alpha}}, \tag{2.11}$$

where ρ and s are reflectivity coefficients.

2.4.2 Constructive approach to verify the controllability condition

Hence, Equation (2.6) is finally recast into[4]

$$\begin{aligned} &\text{if } \exists\, p_I \in T^*\mathcal{M},\ p_I \neq 0 \text{ such that} \\ &\quad \left\langle p_I,\ \tilde{G}(I,f)\,u \right\rangle \geq 0, \qquad f \in \mathbb{S}^1,\ u \in K_\alpha,\ \|u\| = 1. \end{aligned} \tag{2.12}$$

A practical check of the feasibility Problem (2.12) is carried out by solving the auxiliary optimization problem

$$\begin{aligned} \max_{J,\ \|p_I\| \leq 1} \quad & J \quad \text{s.t.} \\ & \left\langle p_I,\ \tilde{G}(I,f)\,u \right\rangle \geq J, \\ & f \in \mathbb{S}^1,\ u \in \partial K_\alpha,\ \|u\| = 1 \end{aligned} \tag{2.13}$$

The constraint $\|p_I\| \leq 1$ is preferred to $\|p_I\| = 1$ to preserve convexity of Problem (2.13). Problem (2.13) is convex and semi-infinite, because inequality constraints need to be enforced on two infinite sets, namely for all true anomalies between 0 and 2π and for all u on the surface of the cone. Evaluating inequalities in the interior of the cone is not necessary because dynamics is affine in u. If J^*, solution of Problem (2.13), is positive, (2.12) is verified: then, as discussed in the previous section, for the cone angle α, there is an obstruction to local controllability around the orbit I. Conversely, when condition (iii) of Theorem 7 holds at I[5], both J^* and the associated minimizer p_I must be zero.

A question of interest for mission design purposes is to identify minimal optical requirements that satisfy the necessary condition. This can be achieved by solving

$$\begin{aligned} \min_{\alpha} \quad & \alpha \qquad \text{s.t.} \\ & J^*(\alpha) = 0 \end{aligned} \tag{2.14}$$

where $J^*(\alpha)$ denotes solution of Problem (2.13) for a given α. This angle can then be mapped into minimal requirements for the reflectivity of the sail via Equation (2.11). We select a specific orbit I_0 and solve Problem (2.13) for various values of α in order to identify the minimum angle solution of Problem (2.14). We aim to find the smallest angle that does not meet the sufficient condition for non-controllability. Figure 2.3 illustrates an example of this process applied to a

[4]Hereafter, duality product between a co-vector and a vector corresponds to a product between a row vector p_I and a matrix $\tilde{G}(I,f)\,u$

[5]In practice, of course, the check can only be made at a single point, while the condition must hold for all I to ensure global controllability.

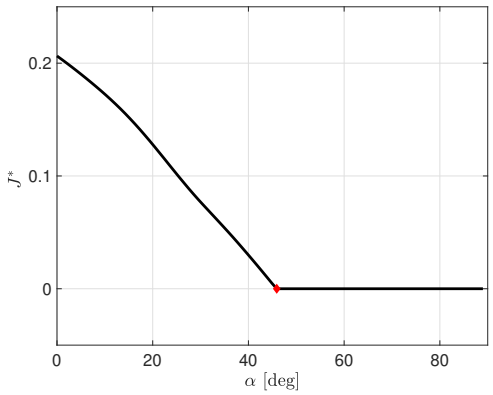

Figure 2.3: Example of the solution of Problems (2.13) (black curve) and (2.14) (red dot). Here, $\gamma_2 = 50\,\text{deg}$, $\gamma_3 = 40\,\text{deg}$, and $e = 0.7$.

specific orbit. The detailed algorithm for obtaining these solutions is provided in Section 2.4.3. The diamond marker highlights the minimum cone angle, which is the solution to Problem (2.14) for the specific value of I used in this simulation. Consequently, any control set with a convex cone opening angle smaller than α_{min} renders the system uncontrollable. Our condition allows for the certification of non-controllability. On the other hand, for angles larger than α_{min}, we cannot certify controllability within our methodology. However, employing an alternative approach to verify condition (iii) of Theorem (7) in Section 2.4.4 indicates that, in practice, α_{min} represents the minimum requirement on the control set for the system to be controllable.

2.4.3 Optimization problem

Numerical solution of Problem (2.13) is achieved by using the formalism of positive trigonometric polynomials [44, 22] to enforce positivity constraints for all values of f and u without introducing any relaxation or discretization of the problem.

Let δ be an angle parametrizing control vectors on the surface of the cone, as shown in Figure 2.4. Therefore, u on the surface of the cone can be expressed as:

$$u = \begin{bmatrix} \cos\alpha \\ \cos\delta \ \sin\alpha \\ \sin\delta \ \sin\alpha \end{bmatrix}$$

where α is fixed. According to Equation (2.13), positivity of the following

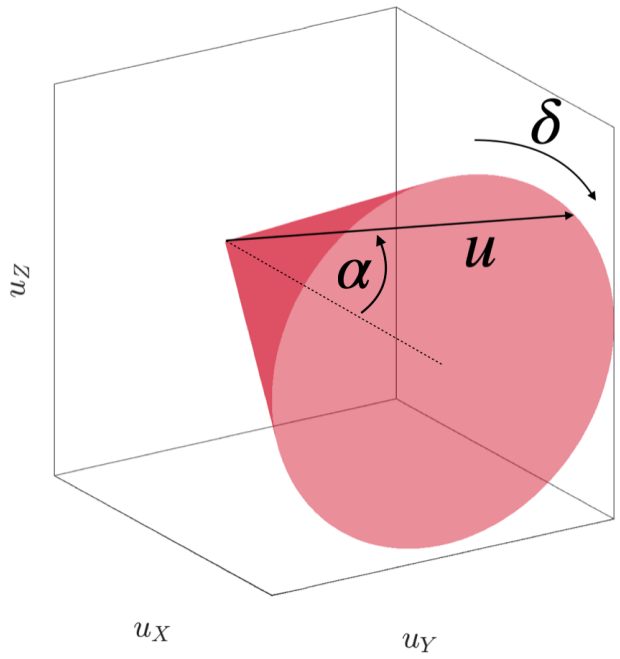

Figure 2.4: Parametrization of the control vector.

constraint must be verified:

$$p_I^T \tilde{G}(I,f)u - J \geq 0 \quad f \in \mathbb{S}^1, \quad u \in \partial K_\alpha. \tag{2.15}$$

Inspection of $\tilde{G}(I,f)u$ reveals that Equation (2.15) is a bivariate trigonometric polynomial of second degree in f and first degree in δ. Let $\langle \cdot, \cdot \rangle_H$ be the Hermitian product of two complex-valued vectors, *i.e.*,

$$\langle a, b \rangle_H = \langle \mathrm{Re}(a), \mathrm{Re}(b) \rangle + \langle \mathrm{Im}(a), \mathrm{Im}(b) \rangle ,$$

and denote

$$\begin{aligned} \Phi(f,\delta) &= \left[1,\ \mathrm{e}^{i\delta}\right]^T \otimes \left[1,\ \mathrm{e}^{if},\ \mathrm{e}^{2if}\right]^T \\ &= \left[1,\ \mathrm{e}^{if},\ \mathrm{e}^{2if},\ \mathrm{e}^{i\delta},\ \mathrm{e}^{if}\mathrm{e}^{i\delta},\ \mathrm{e}^{2if}\mathrm{e}^{i\delta}\right]^T \end{aligned}$$

the basis of bivariate trigonometric polynomials of degree 2 in f and 1 in δ, respectively (here, $\otimes$ denotes Kronecker's product). The left-hand term of Equation(2.15) can be reformulated as

$$\begin{aligned} \left\langle p_I,\ \tilde{G}(I,f)\, u \right\rangle - J &= p_I^T \left(\sum_{l=-1}^{1} \sum_{k=-2}^{2} \widetilde{Gu}^{(k,l)} \mathrm{e}^{i\,k\,f}\, \mathrm{e}^{i\,l\,\delta} \right) - J \\ &= \left\langle \Phi(f,\delta),\ \widetilde{Gu}\, p_I - e_1 J \right\rangle_H \end{aligned}$$

where $\widetilde{Gu}^{(k,l)}(I)$ is the kl-th coefficient of the Fourier transform[6] of $\tilde{G}(I,f)u$, and $e_1 = [1,0,0,0,0,0]^T$.

The formalism of squared functional systems outlined in [44, Chap. 17] and [22, Chap. 3] allows to recast the continuous positivity constraints into LMI. The corresponding squared functional system of $\Phi(f,\delta)$ is $\mathcal{S}^2(f,\delta) = \Phi(f,\delta)\Phi^H(f,\delta)$, where $\Phi^H(f,\delta)$ denotes conjugate transpose of $\Phi(f,\delta)$. Let N be the dimension of $\Phi(f,\delta)$ (6 in our application) and $\Lambda_H : \mathbb{C}^N \to \mathbb{C}^{N\times N}$ is a linear operator mapping coefficients of polynomials in $\Phi(f,\delta)$ to the squared base, so that application of Λ_H on $\Phi(f,\delta)$ yields

$$\Lambda_H(\Phi(f,\delta)) = \Phi(f,\delta)\Phi^H(f,\delta)$$

and define its adjoint operator $\Lambda_H^* : \mathbb{C}^{N\times N} \to \mathbb{C}^N$ as

$$\left\langle Y,\ \Lambda_H\left(\widetilde{Gu}\right)\right\rangle_H \equiv \left\langle \Lambda_H^*(Y),\ \widetilde{Gu}\right\rangle_H, \quad Y \in \mathbb{C}^{N\times N}, \quad \widetilde{Gu} \in \mathbb{C}^N.$$

Theory of squared functional systems postulated by Nesterov [44, Chap. 17] proves that trigonometric polynomial is non-negative if and only if a Hermitian positive semidefinite matrix Y exists such that $\widetilde{Gu} = \Lambda_H^*(Y)$. Dumitrescu extends this theory for multivariate trigonometric polynomials in [22, Chap. 3] and shows that all nonnegative bivariate trigonometric polynomials can be written as sum-of-squares. This equivalence does not hold anymore for three or more variables.

Thus, $\left\langle \Phi(f,\delta), \widetilde{Gu}\right\rangle_H$ is non-negative for all $f \in \mathbb{S}^1$ and for all $u \in K_\alpha$ if and only if a Hermitian positive semidefinite matrix Y exists such that $\widetilde{Gu} = \Lambda_H^*(Y)$, namely

$$\left\langle \Phi(f,\delta),\ \widetilde{Gu}\right\rangle_H \geq 0,\ f \in \mathbb{S}^1,\ u \in K_\alpha \iff \exists Y \succeq 0 :\ \widetilde{Gu} = \Lambda_H^*(Y)$$

In fact, it holds in this case that

$$\begin{aligned}\left\langle \Phi(f,\delta),\ c\right\rangle_H &= \left\langle \Phi(f,\delta),\ \Lambda_H^*(Y)\right\rangle_H = \left\langle \Lambda_H(\Phi(f,\delta)),\ Y\right\rangle_H,\\ &= \left\langle \Phi(f,\delta)\Phi^H(f,\delta),\ Y\right\rangle_H = \Phi^H(f,\delta)\, Y\, \Phi(f,\delta) \geq 0\end{aligned}$$

For trigonometric polynomials Λ^* is given by

$$\Lambda_H^*(Y) = \begin{bmatrix} \operatorname{tr}(\langle Y,\ T_{00}\rangle) \\ \vdots \\ \operatorname{tr}(\langle Y,\ T_{kl}\rangle) \\ \vdots \\ \operatorname{tr}(\langle Y,\ T_{21}\rangle) \end{bmatrix} \quad k = 0,1,2,\ l = 0,1.$$

[6] We note that $\tilde{G}^{kl} = \overline{\tilde{G}^{(-k,--l)}}$ because $\tilde{G}(I,f)u$ is real valued.

where T_j $j = 0, 1, 2$ are the elementary Toeplitz matrices with ones on the j-th diagonal and zeros elsewhere and T_{kl} are obtained from a Kronecker product of such matrices, *e.g.*,

$$T_0 = \begin{pmatrix} 1 & 0 \\ 0 & 1 \end{pmatrix}, \quad T_1 = \begin{pmatrix} 0 & 1 & 0 \\ 0 & 0 & 1 \\ 0 & 0 & 0 \end{pmatrix},$$

$$T_{10} = T_0 \otimes T_1 = \begin{pmatrix} 0 & 1 & 0 & 0 & 0 & 0 \\ 0 & 0 & 1 & 0 & 0 & 0 \\ 0 & 0 & 0 & 0 & 0 & 0 \\ 0 & 0 & 0 & 0 & 1 & 0 \\ 0 & 0 & 0 & 0 & 0 & 1 \\ 0 & 0 & 0 & 0 & 0 & 0 \end{pmatrix}$$

Finally, the inequality in Equation (2.15) is rewritten as an LMI:

$$\begin{aligned} & \left\langle p_I,\ \tilde{G}(I, f)\, u \right\rangle - J \geq 0,\ f \in \mathbb{S}^1,\ u \in \partial K_\alpha \\ \iff \quad & \exists\, Y \succeq 0 \ \text{ such that } \ \widetilde{Gu}\, p_I - e_1 J = \Lambda_H^*(Y) \end{aligned}$$

where $Y \in \mathbb{C}^{6\times 6}$ is a Hermitian matrix to be determined. Hence, the finite-dimensional counterpart of Problem (2.13) is

$$\begin{aligned} \min_{J,\, \|p_I\| \leq 1,\, Y \in \mathbb{C}^{6\times 6}} \quad & J \quad \text{s.t.:} \\ & Y \succeq 0 \\ & \Lambda_H^*(Y) = \widetilde{Gu}\, p_I - e_1 J \end{aligned} \tag{2.16}$$

Problem (2.16) consists of a convex programming with 27 design variables (scalar J, $p_I \in \mathbb{R}^5$, and $Y \in \mathbb{C}^{6\times 6}$ symmetric), the ball-constraint $|p_I| \leq 1$, and a single LMI of a 6×6 matrix. The computational time to solve this problem is extremely modest. Eventually, solution of Problem (2.14) is carried out by means of a simple bisection algorithm, which does not require the evaluation of derivatives of the non-smooth function $J^*(\alpha)$ (we note that Problem (8) has trivial solution $J = 0$, $p_I = 0$ for $\alpha > \alpha_{min}$). The CVX software [27, 26] is used to solve the convex Problem (2.16). Fourier coefficients of $\tilde{G}(I, f)$, which is a second-degree trigonometric polynomial in f, are evaluated by means of the fast Fourier transform (FFT) algorithm. We stress that there is no relaxation of Problem (2.16) with respect to Problem (2.13). Remarkably, enforcement of the constraint for all values of f and u is exact and stems from the trigonometric nature of $\tilde{G}(I, f)u$.

2.4.4 Validation by means of another methodology

As mentioned earlier, the previous methodology enables certification of non-controllability for solar sails that do not meet the minimum requirement. However, it does not necessarily provide proof of the controllability for other cases. Therefore, we propose a different algorithm for the evaluation of the condition for controllability of solar sails, proposed in [30]. Recall Theorem 7 and its condition (iii). We want to check the evaluation of condition (iii) at a fixed single point $I \in \mathcal{M}$.

First, let us consider motion given by Equation (1.5) and (2.7). Since we want to verify if a sail can move in the neighborhood of the initial orbit given by I, it is interesting ot rewrite System (1.5) in terms of displacement of the slow state elements along the orbit, denoted $\delta I = I - I_0$. As mentioned earlier, SRP has a very small magnitude, this is why it is usually considered as a perturbation. Thus, we neglect the ε-terms of the equation of f:

$$\frac{\mathrm{d}\, f}{\mathrm{d}\, t} = \omega(I, f),$$

Therefore, dynamics of δI is given by:

$$\begin{aligned} \frac{\mathrm{d}\delta I}{\mathrm{d}f} &= \frac{1}{\omega(I,f)} \frac{\mathrm{d}\, I}{\mathrm{d}\, t} = \frac{\varepsilon}{\omega(I,f)} \sqrt{\frac{a\,(1-e^2)}{\mu}} G(I,f)\, u(f) \\ &= \varepsilon \frac{a\,(1-e^2)^2}{\mu(1+e\cos f)^3} \widetilde{G}(I,f)\, u(f) \end{aligned} \tag{2.17}$$

Since we are interested, again, in directions of the displacement for controllability purposes, we can neglect its positive multiplying coefficient following the example of Equation (2.7):

$$\varepsilon \, \frac{a\,(1-e^2)^2}{\mu(1+e\cos f)^3} \geq 0, \quad \forall f \in \mathbb{S}^1.$$

We also neglect the changes on slow variables over one orbital period so that I will be assumed *constant* $I := \bar{I}$.

Proposition 11. *Let $e_0, \ldots, e_n$ in $T_I\mathcal{M}$ be the vertices of an n-simplex containing 0 in its interior; condition (iii) holds if and only if, for all $k \in \{0, \ldots, n\}$, the accessory convex control problem with state δI valued in $T_I\mathcal{M}$*

$$\frac{\mathrm{d}\delta I}{\mathrm{d}f} = \tilde{G}(\bar{I}, f)\, u(f), \quad u(f) \in \mathrm{cone}(U), \tag{2.18}$$

$$\delta I(0) = 0, \quad \delta I(2\pi) \text{ parallel to } e_k, \tag{2.19}$$

is feasible.

Proof. Negating condition (iii) is equivalent to asserting the existence of p_I in $T_I^*\mathcal{M}$, nonzero, such that

$$\left\langle p_I, \tilde{G}(\bar{I}, f)\, u(f) \right\rangle \leq 0, \quad f \in \mathbb{S}^1, \quad u \in U.$$

In this inequality, one can replace U by its conical hull. Moreover, it is still equivalent that

$$\left\langle p_I, \int_0^{2\pi} \tilde{G}(\bar{I}, f)\, u(f)\, \mathrm{d}f \right\rangle \leq 0 \tag{2.20}$$

for all u in $\mathscr{L}^\infty(0, 2\pi)$ valued in cone(U). Indeed, one implication is obvious by linearity and positivity of the integral, while the converse is true since the Dirac measure at any f in $[0, 2\pi]$ can be approximated by a sequence of $\mathscr{L}^\infty$ functions valued in cone(U). Finally, since the simplex generated by $e_0, \ldots, e_n$ is a neighborhood of the origin in $T_I\mathcal{M}$, negating the existence of a nonzero p_I in $T_I^*\mathcal{M}$ such that (2.20) holds takes us back to condition (iii), and says the following: for all k in $\{0, \ldots, n\}$, there is an essentially bounded control valued in the conical hull of U such that

$$\int_0^{2\pi} \tilde{G}(\bar{I}, f)\, u(f)\, \mathrm{d}f = e_k,$$

which is the expected set of $n + 1$ feasibility conditions. □

One way to check these conditions is to consider, for each k in $\{0, \ldots, n\}$, the accessory convex optimal control problem

$$\frac{1}{2} \int_0^{2\pi} |u(f)|^2\, \mathrm{d}f \to \min$$

under constraints (2.18)-(2.19). We show that each of these problems can be accurately approximated by a convex mathematical program. These finite dimensional problems are obtained by approximating $K_\alpha := \text{cone}(U)$ by a polyhedral cone and truncating the Fourier series of the control. See also Section 3.2 for a similar approach on a slightly different problem (displacement maximization in a given direction) and with a different motivation.

Discretization of the accessory problem

A conservative discretization of the accessory control problems is achieved in two steps. First, K_α is approximated by the polyhedral cone $K_\alpha^g \subset K$ generated by g vertices $V_1, \ldots, V_g$ chosen in ∂K_α: admissible controls are given by a conical combination of the form

$$u(f) = \sum_{j=1}^{g} \nu_j(f) V_j, \quad \nu_j(f) \geq 0, \quad f \in \mathbb{S}^1, \quad j = 1, \ldots, g.$$

Second, an N-dimensional basis of trigonometric polynomials, $\Phi(f) = \left(1, e^{if}, e^{2if}, \ldots, e^{(N-1)if}\right)$, is used to model functions ν_j as

$$\nu_j(f) = (\Phi(f)|c_j)_H$$

where $c_j \in \mathbb{C}^N$ are complex-valued coefficients (serving as design variables of the finite-dimensional problem), and $(\cdot|\cdot)_H$ is the Hermitian product on $\mathbb{C}^N$.

Positivity constraints on the functions ν_j define a semi-infinite optimization problem; these constraints, again, are enforced by leveraging on the formalism of squared functional systems outlined in [44] which allows to recast continuous positivity constraints into LMI. For an admissible control u valued in K_α^g, one has

$$\int_0^{2\pi} \sum_{i=1}^{3} u_i(f)\tilde{G}_i(\bar{I}, f)\,\mathrm{d}f = \sum_{j=1}^{g} \left(L_j c_j + \bar{L}_j \bar{c}_j\right)$$

with $L_j(\bar{I})$ in $\mathbb{C}^{n\times N}$ defined by

$$L_j(\bar{I}) = \frac{1}{2}\sum_{i=1}^{3} \int_{\mathbb{S}^1} V_{ij}\tilde{G}_i(\bar{I}, f)\Phi^H(f)\,\mathrm{d}f,$$

where $\Phi^H(f)$ denotes the Hermitian transpose of $\Phi(f)$ and where $V_j = (V_{ij})_{i=1,\ldots,m}$. We note that the components of $L_j(I)$ are Fourier coefficients of the function $\sum_{i=1}^{3} V_{ij}\tilde{G}_i(\bar{I}, f)$. The discrete Fourier transform (DFT) can be used to approximate $L_j(\bar{I})$. Since vector fields F_i are smooth, truncation of the series is justified by the fast decrease of the coefficients. Finally, for a control u valued in K_α^g with coefficients ν_j that are truncated Fourier series of order $N-1$, the L^2 norm over $\mathbb{S}^1$ is easily expressed in terms the coefficients c_j using orthogonality of the family of complex exponentials:

$$\begin{aligned}\frac{1}{2}\int_{\mathbb{S}^1} |u(f)|^2\ \mathrm{d}f &= \frac{1}{2}\sum_{j,l=1}^{g}\sum_{k=0}^{N-1} V_l^T V_j\left(\bar{c}_{lk}c_{jk} + c_{lk}\bar{c}_{jk}\right)\\ &= \sum_{l,j=1}^{g} V_l^T V_j (c_j|c_l)_H.\end{aligned}$$

As a result, for every vertex e_k, the finite-dimensional convex programming approximation is

$$\begin{aligned}\min_{c_j\in\mathbb{C}^N,\ Y_j\in\mathbb{C}^{N\times N}} &\sum_{j,l=1}^{g} V_j^T V_l (c_j|c_l)_H \quad \text{subject to}\\ &\sum_{j=1}^{g}\left(L_j c_j + \bar{L}_j\bar{c}_j\right) = e_k\\ &Y_j \succeq 0, \quad \Lambda^*(Y_j) = c_j, \quad j = 1,\ldots,g.\end{aligned} \tag{2.21}$$

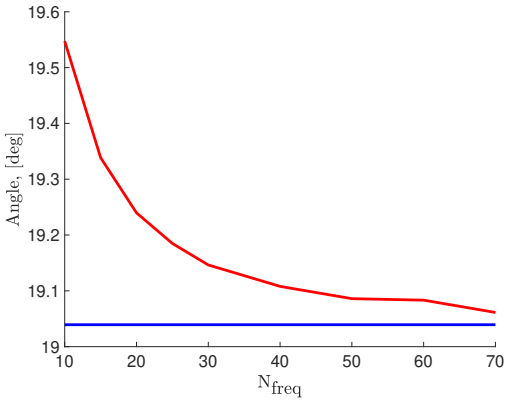

Figure 2.5: Convergence of the results obtained with two algorithms as a function of the number of harmonics used to estimate the control action (in red). The exact minimum angle obtained with the methodology detailed earlier is depicted in blue.

Proposition 12. *If, for all $k = 0, \dots, n$, problem* (2.21) *admits a solution, then condition (iii) of Theorem 6 holds.*

Proof. Let $k = 0, \dots, n$, and choose g vertices $V_1, \dots, V_g$ in ∂K_α. Any solution of (2.21) generates a control valued in $K_\alpha^g \subset K_\alpha = \text{cone}(U)$, that is a feasible control for constraints (2.18)-(2.19). Apply Proposition 11 to conclude.

□

Finally, Proposition 12 allows to check if the sail with given optical properties is controllable along the initial orbit $I \in \mathcal{M}$. By reformulating the problem in the same way as Problem (2.14), we can for a given orbit I find the minimum angle α satisfying the controllability requirement. Although both proposed methodologies in this Section verify controllability properties differently, we can compare the obtained result in term of the minimum cone angle $\alpha_{\min}$ necessary for controllability for a given orbit I.

Figure 2.5 shows that the α_{min} estimated with this second algorithm for a specific orbit converges to the value obtained with the methodology presented earlier in this chapter as the degree of the trigonometric polynomials of the control action is increased. The estimation of the second algorithm is conservative (namely, it overestimates α_{min}) because an interior polyhedral approximation of the convex cone is used. We stress that the methodology outlined in Section 2.4.3 outperforms the one in this section since the exact solution of Problem (2.13) is achieved by solving a low-dimensional convex program without any relaxation.

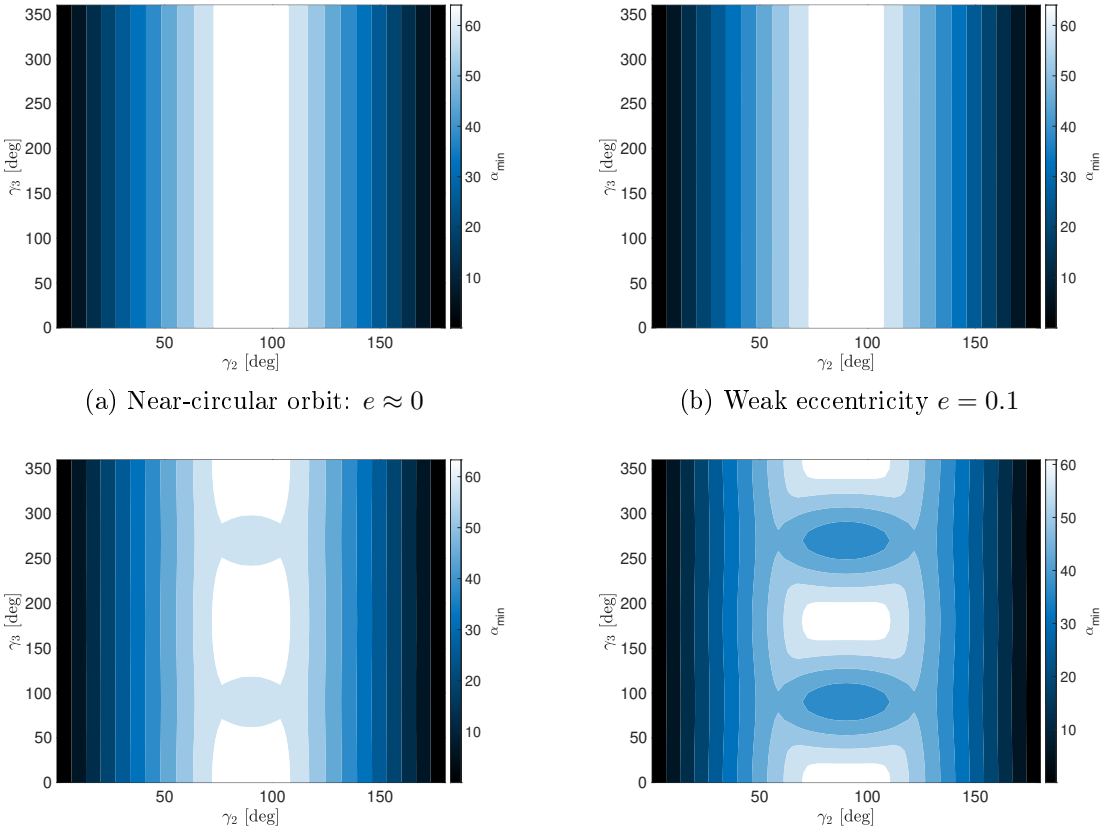

(a) Near-circular orbit: $e \approx 0$

(b) Weak eccentricity $e = 0.1$

(c) Elliptic orbit with $e = 0.5$

(d) High eccentricity $e = 0.9$

Figure 2.6: Results for different geocentric orbits

2.5 Results for solar sails around a body

2.5.1 Minimal requirement for different orbital configurations

This section presents some results achieved for solar sail using the algorithm presented in Section 2.4.2 and 2.4.3. Figure 2.6 shows the minimum cone angle satisfying the condition as a function of γ_2 and γ_3 for various values of eccentricity (we recall that semi-major axis and γ_1 have no influence on this angle). The minimal angle is symmetric with respect to $\gamma_2 = 90\,\text{deg}$ because $\left\langle p_I,\ \tilde{G}(e, \gamma_2, \gamma_3, f)\, u \right\rangle = \left\langle -p_I,\ \tilde{G}(e, \pi - \gamma_2, \gamma_3, f)\, u \right\rangle$. Solution is independent of γ_3 for circular orbits, as expected. Sensitivity with respect to γ_3 remains moderate even for larger eccentricities. The minimal angle approaches zero as $\sin(\gamma_2) \to 0$. In this case, $\hat{s}$ is aligned with the angular momentum of the orbit. On the other hand, for $\gamma_2 = 90\,\text{deg}$, the Sun is in the orbital plane.

Figure 2.7a and 2.7b represent α_{min} as function of γ_3 or γ_2, respectively, for various values of eccentricity. Results confirm strong dependency of α_{min} on γ_2,

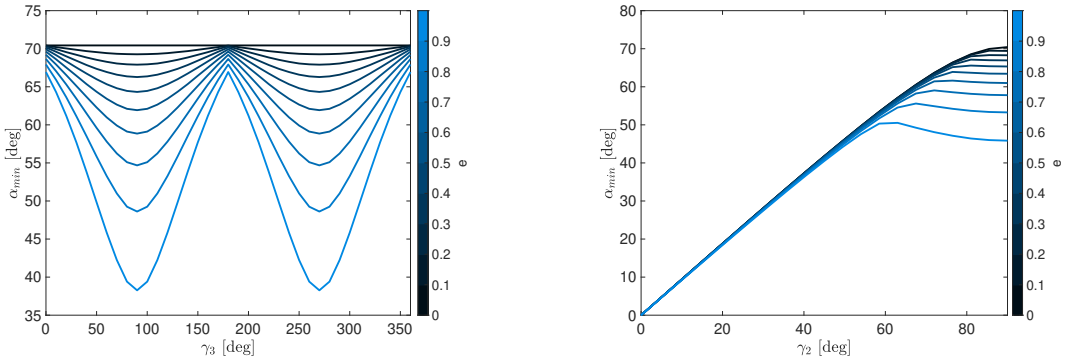

(a) γ_2 fixed at 90 [deg]

(b) γ_3 fixed at 120 [deg]

Figure 2.7: Minimum cone angle as a function of Euler angles.

and γ_3 for large eccentricity. Hence, controllability of near circular orbits requires more reflective sails with respect to high-eccentric orbits. Finally, we stress that the minimum angle α exists for all orbits, and it is systematically smaller than 90 deg, which means that the sail has not to be ideal to make System (1.5) controllable. To compare with a real solar sail, optical properties of the NASA reference model [29] (designed to support Near-Earth Asteroid Scout (NEA-Scout) and Lunar Flashlight solar sail missions) correspond to a cone angle of 58.6 deg. This value is sufficient to satisfy the proposed condition for most planet-centered orbits, except for highly inclined ones.

2.5.2 Station-keeping example

The determination of α_{min} entails practical consequences in the design of solar-sail maneuvers by imposing minimal requirements on its reflectivity. For example, consider the scenario where a solar sail is used to carry out station-keeping of a lunar orbiter. The objective is to maintain the sail in the proximity of the nominal orbit $I_0 = (150\,\text{deg}, 60\,\text{deg}, 0\,\text{deg}, 2R_{Moon}, 0.01)$, where R_{Moon} denotes the equatorial radius of the Moon. Initial conditions are perturbed and the motion of the sail is subject to non-spherical gravitational harmonics up to order and degree 2. A simple local-optimal feedback controller that instantaneously minimizes the rate of change of the error function $e(t) = |I(t) - I_0|$, is used to carry out the maneuver. The reference orbit has $\alpha_{min} = 52\,\text{deg}$, which corresponds to a minimum reflectivity coefficient of $\rho = 0.79$. Figures 2.8a and 2.8b depict the evolution of semi-major axis and error function for a poorly and a highly-reflective sail, namely specular reflectivity equal to 0.5 and 0.9, respectively. At the beginning of the maneuver, both sails are able to decrease the error. This is because the direction of $I(t) - I_0$ points inside the reachable half-space of the poorly-reflective sail. Once $I(t) - I_0$ is in the unreachable space, the poorly-reflective sail

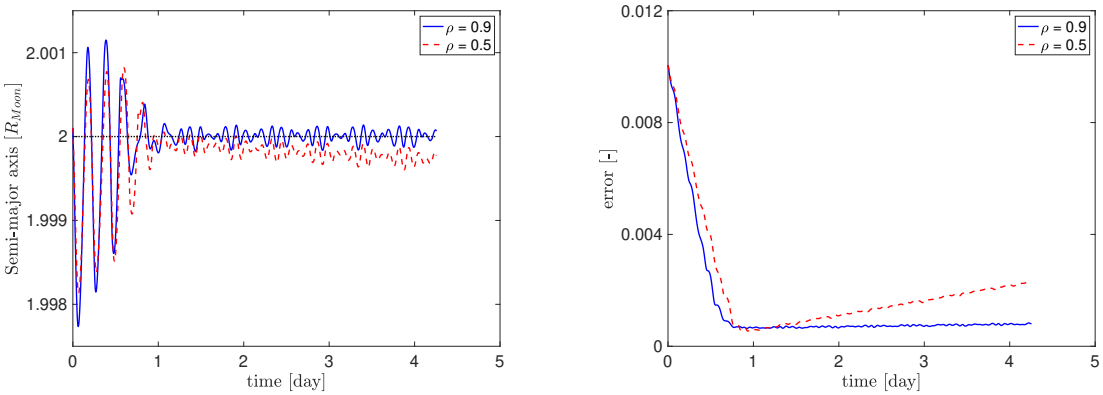

(a) Trajectory of the semi-major axis. Black dashed dot is the reference value.

(b) Evolution of the error function.

Figure 2.8: Implementation of a station-keeping algorithm using a locally-optimal control law.

starts drifting away from the reference, and its error function increases, whereas the highly-reflective sail is able to keep its state in the proximity of I_0. Because external perturbations are included, controllability of the highly reflective sail could be jeopardized if its surface-to-mass ratio is not large enough ($20\,\mathrm{m}^2/\mathrm{kg}$ in this example), but the poorly-reflective sail will not be able to stabilize the system regardless its size.

2.5.3 A comment on heliocentric orbits

Consider now a sail in a heliocentric orbit. This scenario can be a case for interplanetary transfers, for example. The same equations with two major corrections are used to model the problem. First, the rotation matrix R in Equation (1.5) is removed, since the local vertical local horizontal frame is used, and $\hat{s}$ is aligned with the radial direction. Moreover, the problem has central symmetry, so that results do not depend on any orbital element except for the eccentricity. For a perfectly absorptive solar sail, the dynamical system is not bracket generating, because the control is radial, as proved in [4]. The integral of motion related to this rank deficiency is the magnitude of the angular momentum. For a non-ideal sail, the system becomes bracket generating as soon as a tangential component appears: even for very weakly reflective sails.

Using the methodology of Section 2.4.3 to solve the optimization problem indicates that even a very poorly reflective sail (*i. e.*, $0 < \rho \ll 1$) is locally controllable over one orbital period. Specifically, the necessary condition is satisfied as soon as the sail is capable of producing even a weak force orthogonal to the radial vector. Therefore, the minimum cone angle α_{min} approaches zero. However, interplanetary transfers are often envisaged on a fraction of an heliocentric orbit,

so that the proposed methodology is not very useful to analyze mission scenarios of interplanetary transfers: any non-completely absorptive sail yields a controllable system, but the time necessary to achieve maneuvers can be extremely long to make this result of no practical use.

2.6 Generalization of the methodology to non-Keplerian orbits

Due to specific mission goals, many satellites are subject to cone constraints on the thrust direction. For example, James Webb Space Telescope, launched on December 25, 2021 toward a Halo orbit around the Sun-Earth L_2 libration point, has a thermal shield that must prevent the telescope and other instruments from overheating [52]. Therefore, it is constrained to always keep its attitude such that the angle between the normal to the shield and the Sun direction is smaller than 53 deg. It results in conical constraints for the propulsion directions. Using chemical propulsion to perform small impulsive corrections of the trajectory or a low-thrust satellite with very specific constraints on the control does not always allow to do any desirable maneuver, as we showed in this chapter.

For solar sails analysis, in the previous sections of this chapter, we considered elliptic Keplerian orbits, and we formulated a convex optimization problem aimed at assessing whether some functions of the integrals of motion could not be decreased after one orbital period. Existence of such functions implies that there is a half-space of the neighborhood orbit's coordinates (orbital elements) where motion is locally forbidden. We strongly relied on the super-integrability of the Kepler problem. Now, we extend the previous methodology to infer local controllability of station-keeping satellites for *any* periodic orbit, regardless the dynamical system at hand. Given the projection of the nominal orbit on a surface of section, the methodology aims at verifying if a half space of such projection exists where the motion is forbidden after one orbital period. Variation of parameters is used to achieve a convex optimization problem that investigates the existence of obstructions to variations of local integrals of motion. Conical constraints are enforced again by leveraging on the formalism of positive polynomials postulated by Nesterov [44], so that a finite-dimensional formulation of the convex program is achieved. Halo orbit in the CRTBP is eventually considered in the case study, but we emphasize again that the methodology is developed for a generic locally-integrable system.

2.6.1 Necessary condition for local controllability

Consider the equations of motion given by Equation (1.6):

$$\frac{\mathrm{d}\,x}{\mathrm{d}\,t} = f(x) + Bu, \qquad x \in \mathbb{R}^6, \quad u \in K_\alpha,\ \|u\| \leq \varepsilon \tag{2.22}$$

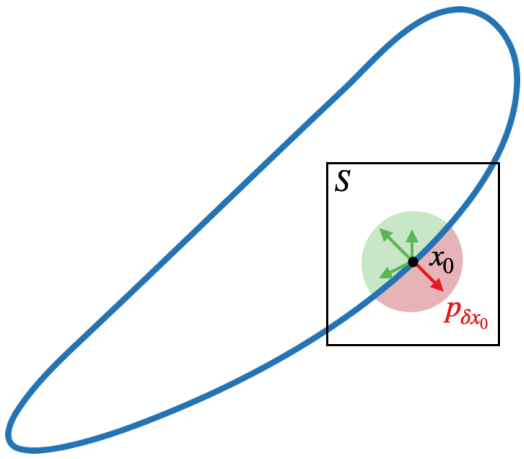

Figure 2.9: Forbidden half-space of δx_0 generated by $p_{\delta x_0}$

Here, K_α is a cone of revolution characterized by an opening angle α, ε is thrust magnitude, which is assumed to be small. Again, thrust magnitude does not play any role for the controllability analysis since it has no influence on possible directions of thrust, and

Given the conical constraint on the thrust vector, $u \in K_\alpha$, we are interested in determining if System (2.22) is locally controllable. Specifically, given a periodical (uncontrolled) reference orbit $y(t)$ of period T and a surface of section $S(x)$, and denoting x_0 the coordinates of the orbit at the crossing of $S(x)$, namely

$$\begin{cases} \dfrac{\mathrm{d}\, y}{\mathrm{d}\, t} = f(y) \\ y(0) = y(T) = x_0 \\ S(x_0) = 0 \end{cases}$$

we are interested in determining if controls in K_α are capable of moving the crossing point on $S(x)$ in an open neighborhood of x_0 after a period T, as shown in Figure 2.9. To this purpose, we introduce a necessary condition on α for the given orbit in order to have local controllability under the constraint $u \in K_\alpha$.

Denoting by $\Phi(t, x_0)$ the state transition matrix of the system, and by $\delta x_0 \in T_{x_0} S$ a perturbation of the initial state x_0, uncontrolled linearized motion in proximity of the periodic orbit is governed by

$$\delta x(t) = \Phi(t, x_0)\delta x_0. \tag{2.23}$$

Linearization of Equation (2.22) gives:

$$\frac{\mathrm{d}\,\delta x}{\mathrm{d}\,t} = \left.\frac{\partial f}{\partial x}\right|_{y} \delta x + Bu. \tag{2.24}$$

Recalling that $\dfrac{\mathrm{d}\,\Phi}{\mathrm{d}\,t} = \dfrac{\partial f}{\partial x}\,\Phi$, differentiation of Equation (2.23) and substitution in Equation (2.24) yields the classical variation of parameters

$$\frac{\mathrm{d}\,\delta x_0}{\mathrm{d}\,t} = \Phi^{-1}(t, x_0)\, B\, u, \quad \delta x_0 \in T_{x_0}S, \quad u \in K_\alpha. \tag{2.25}$$

Similarly to what is done in the previous sections, the necessary condition for local controllability of the satellite is written in terms of possible displacements of the system on the Poincaré map, *i.e.* by verifying if the state can be moved in any arbitrary direction of the tangent space $T_{x_0}S$ after one orbital period. Negation of this condition implies the existence of a not accessible half-space in the neighborhood of x_0, as shown in Figure 2.9. Since the interior thrust directions of K_α can be approximated by combinations of vectors on the boundary of the cone, ∂K_α, we propose to solve the following problem in order to verify the necessary condition:

if $\exists\ p_{\delta x_0} \in T^*_{x_0}S,\ p_{\delta x_0} \neq 0$ such that

$$\left\langle p_{\delta x_0},\ \frac{\mathrm{d}\,\delta x_0}{\mathrm{d}\,t} \right\rangle \geq 0, \qquad \forall\ u \in \partial K_\alpha, \|u\| = 1,\ t \in [0, T)$$

then System (2.22) is not locally controllable in one orbit.

If $p_{\delta x_0}$ solution of Problem (2.12) exists, then the linear functional

$$V(t, u) = \left\langle p_{\delta x_0},\ \Phi^{-1}(t, x_0)\, B(y(t))\, u \right\rangle$$

cannot be decreased for any $u \in K_\alpha$ and $t \in [0, T)$, hence motion is forbidden in the half-space with normal $p_{\delta x_0}$, and the satellite cannot move in any direction pointing inside this half-space after one orbital period. Absence of forbidden directions for control of satellites is crucial for station-keeping.

2.6.2 Convex optimization problem to verify the necessary condition

A practical check of the necessary condition is carried out by solving

$$\begin{aligned} \max_{J,\ \|p_{\delta x_0}\| \leq 1} \quad & J \quad \text{s.t.} \\ & \left\langle p_{\delta x_0},\ \Phi^{-1}(t, x_0) B(y(t)) u \right\rangle \geq J, \\ & \forall\ u \in \partial K_\alpha,\ \|u\| = 1,\ t \in [0, T]. \end{aligned} \tag{2.26}$$

Problem (2.26) is convex and semi-infinite, because inequality constraints need to be enforced for all u on the surface of the cone and for all time between

0 and the period T. Evaluating inequalities in the interior of the cone is not necessary because dynamics is affine in u. If J^*, solution of Problem (2.26), is strictly positive, then the necessary condition is not satisfied and the system is not locally controllable for the given α and x_0. The constraint $\|p_{\delta x_0}\| \leq 1$ is preferred to the equality condition $\|p_{\delta x_0}\| = 1$ to preserve the convexity properties of Problem (2.26).

Again, as was highlighted in Section 2.4.2, for the mission design purposes, it is interesting to know which is the minimum α angle of the thrust cone satisfying the necessary condition. Therefore, we can formulate a problem identical to Problem (2.14) that can be efficiently solved by means of a simple bisection method.

2.6.3 Discretization of the optimization problem

Numerical solution of Problem (2.26) is achieved by:

1. Parametrizing K_α by means of an angle δ, as shown in Figure 2.4.

2. Given that u is trigonometric in δ, with a change of variables

$$t \in [0, T], \quad \varphi = \frac{2\pi}{T} t,$$

using Fourier transform for Equation (2.25):

$$\Phi^{-1}(\varphi, x_0)\, B\, u = \sum_{l=-1}^{1} \sum_{k=-d}^{d} C^{(k,l)} \mathrm{e}^{ik\varphi} \mathrm{e}^{il\delta},$$

where $C^{(k,l)}$ is the kl-th coefficient of the Fourier transform of $\Phi^{-1}(\varphi, x_0)\, B\, u$ and d the degree of truncation of the series in φ. Note that u is already a bivariate trigonometric polynomial of degree 1 in δ and d in φ. Thus, the inequality from Equation (2.26) becomes:

$$\begin{aligned} &\left\langle p_{\delta x_0},\ \Phi^{-1}(\varphi, x_0) B u \right\rangle \geq J \\ \iff & p_{\delta x_0}^T \left(\sum_{l=-1}^{1} \sum_{k=-d}^{d} C^{(k,l)} \mathrm{e}^{ik\varphi} \mathrm{e}^{il\delta} \right) - J \geq 0 \end{aligned}$$

In the example of a Halo orbit given later, we decide to truncate the Fourier series at $d = 30$, as the convergence of the coefficients is enough to find the minimum cone angle, as shown in Figure 2.10;

3. Using the formalism of positive polynomials [44, 22] to enforce positivity constraints.

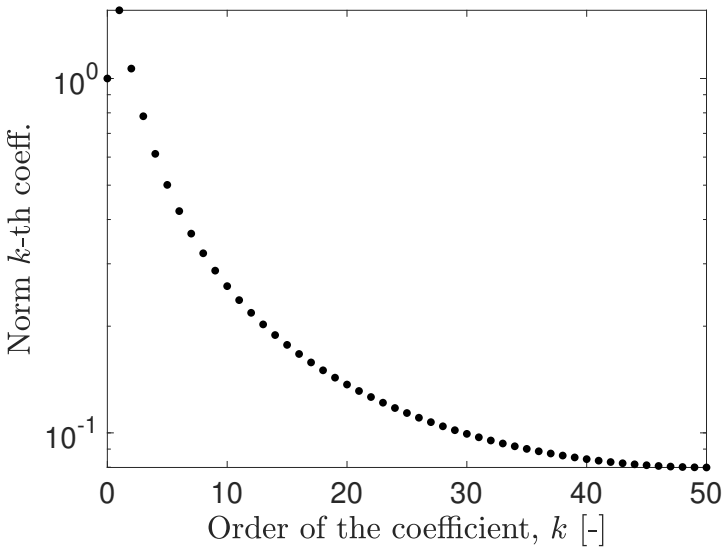

Figure 2.10: Convergence of Fourier coefficients

Consider the basis of bivariate trigonometric polynomials of degree d in φ and 1 in δ:

$$\begin{aligned}\mathcal{P}(\varphi,\delta) &= \left[1,\ \mathrm{e}^{i\delta}\right]^T \otimes \left[1,\ \mathrm{e}^{i\varphi},\ \mathrm{e}^{2i\varphi},\dots,\ \mathrm{e}^{di\varphi}\right]^T \\ &= \left[1,\ \mathrm{e}^{i\varphi},\ \mathrm{e}^{2i\varphi},\dots,\ \mathrm{e}^{di\varphi},\ \mathrm{e}^{i\delta},\ \mathrm{e}^{i\varphi}\mathrm{e}^{i\delta},\ \mathrm{e}^{2i\varphi}\mathrm{e}^{i\delta},\dots,\ \mathrm{e}^{di\varphi}\mathrm{e}^{i\delta}\right]^T\end{aligned}$$

and C vector of coordinates of the polynomial in the basis. Its corresponding squared functional system is $\mathcal{S}^2(\varphi,\delta) = \mathcal{P}(\varphi,\delta)\mathcal{P}^H(\varphi,\delta)$. Let N be the dimension of $\mathcal{P}(\varphi,\delta)$ ($N = 2\times(d+1)$ in our application). Using once again the theory of squared functional systems alows to write:

$$\langle \mathcal{P}(\varphi,\delta),\ C\rangle_H \geq 0,\ (\varphi,\delta)\in\mathbb{T}^2,\ u\in K_\alpha \quad\Longleftrightarrow\quad \exists Y\succeq 0:\ C=\Lambda_H^*(Y).$$

Finally, the inequality in Equation (2.26) is rewritten as an LMI:

$$\begin{aligned}&\left\langle p_{\delta x_0},\ \Phi^{-1}(\varphi,x_0)Bu\right\rangle - J\geq 0,\ (\varphi,\delta)\in\mathbb{T}^2,\ u\in\partial K_\alpha \\ \Longleftrightarrow\quad &\exists\ Y\succeq 0\ \text{ such that }\quad C\,p_{\delta x_0} - e_1 J = \Lambda_H^*(Y)\end{aligned}$$

where $Y\in\mathbb{C}^{N\times N}$ is defined as in Section 2.4.3. Hence, the finite-dimensional counterpart of Problem (2.26) is

$$\begin{aligned}\min_{J,\,\|p_{\delta x_0}\|\leq 1,\,Y\in\mathbb{C}^{62\times 62}}\quad & J \quad \text{s.t.:} \\ & Y\succeq 0 \\ & \Lambda_H^*(Y) = C\,p_{\delta x_0} - e_1 J\end{aligned} \tag{2.27}$$

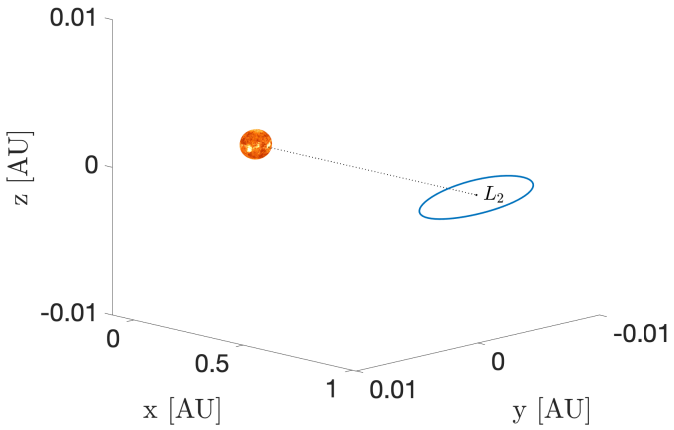

Figure 2.11: Halo orbit used for the simulation. Size of the Sun is schematical.

Solution of Problem (2.14) is carried out by means of a simple bisection algorithm, which does not require the evaluation of derivatives of the non-smooth function $J^*(\alpha)$ (we note that Problem (8) has trivial solution $J = 0,\ p_{\delta x_0} = 0$ for $\alpha > \alpha_{min}$). The CVX software [27, 26] is used to solve the convex Problem (2.27). Fourier coefficients of $\Phi^{-1}(\varphi, x_0)\, B\, u$ are evaluated by means of the FFT algorithm. The only relaxation of Problem (2.27) with respect to Problem (2.26) is truncation of the Fourier series. No discretization was done to approximate u on the surface of the cone.

2.6.4 Case study

Let us consider a periodical Halo orbit situated around Sun-Earth L2 point, as shown in Figure 2.11. It is the same point where James Webb Space Telescope were sent. We suppose that a satellite has to perform station-keeping around this orbit. The given satellite can produce either small impulsions using chemical propulsion or low-thrust engines, and has a conical constraint on the directions of the thrust. Our goal is to determine what is the maximum conical constraint that can be imposed on the propulsion, *i.e.* what is the minimum cone angle for thrust directions that allows local controllability after one orbital period. To find out the minimum requirement, we apply the proposed methodology on the given periodical Halo orbit. Initial data of the orbit is $x_0 = (1.0083, 5.15 \times 10^{-19}, 0.0010, 1.3714 \times 10^{-16}, 0.0102, -4.1015 \times 10^{-17})$ in AU according to the Sun-centered reference frame.

The results given by Figure 2.12 show that the minimum thrust cone angle $\alpha = 43$ deg exists, and is a necessary requirement for local controllability of a station-keeping satellite using low-thrust or small chemical impulsions. The

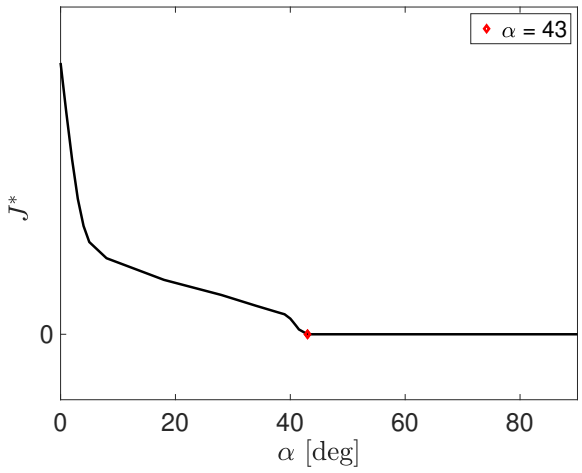

Figure 2.12: Solution of Problems (2.26) (black curve) and $\alpha_{\min}$ denoted in red.

results mean that a satellite with thrust directions limited by a cone of less than 43 degrees, cannot move its state toward a half-space of the initial configuration neighborhood, and, therefore, cannot perform station-keeping on the orbit of reference. For instance, such a satellite may be unable to increase its velocity in the y-direction or decrease its z-position after completing one orbital period. As a result, it lacks local controllability within a single orbital period. It is possible that global controllability could still be achieved, implying that the satellite needs to deviate from the initial orbit to execute the required maneuver and then return. However, this would likely necessitate a significant amount of propellant or may not be feasible using low-thrust engines.

Conclusion

In conclusion, this chapter makes two main contributions. Firstly, it establishes sufficient conditions for the controllability of affine control systems with a drift, where all solutions exhibit periodic behavior. These conditions extend beyond previous results by encompassing control sets whose convex hull is not a neighborhood of the origin. The conditions are expressed in terms of pushforwards along the flow of the drift, providing a novel approach that avoids reliance on Lie brackets. Furthermore, this approach also implies local controllability of a time-varying linear approximation with constrained controls. The chapter presents both global and local results.

Secondly, the chapter introduces a novel methodology to assess the local controllability of nonideal solar sails in orbit around celestial bodies. This methodology utilises a semi-infinite convex optimisation problem, leveraging the

formalism of bivariate polynomials and the rational trigonometric nature of the governing equations. By evaluating the sign of the polynomial, the methodology identifies potential noncontrollability, indicating inaccessible half-spaces within the neighborhood of the current state vector in the orbital element set. Extensive analysis reveals the existence of a minimum reflectivity requirement for the sail to satisfy the necessary condition for controllability in any orbit. Remarkably, the research demonstrates that local controllability properties hold universally (namely, regardless the planetary constant and the surface-to-mass ratio of the sail) for nonideal sails, provided a sufficient amount of incoming radiation is reflected. These findings have significant implications for mission analysis in station-keeping applications and transfer maneuvers involving solar sails.

To further advance this research, a proposed generalisation of the methodology can be applied to non-Keplerian orbits, specifically for the analysis of satellite station-keeping with cone-constrained thrust. As an example, we consider the case of a Halo orbit around the L2 Lagrangian point, taking inspiration from the requirements of the James Webb Space Telescope to maintain a specific attitude towards the Sun. The minimum requirement presented in this study is applicable to both low-thrust and chemical propulsion systems, with the condition that small impulses are utilised to ensure the satellite remains on its designated orbit. By extending the methodology to non-Keplerian orbits, a broader range of satellite missions can benefit from the local controllability assessment.

Chapter 3

Optimal control of solar sails

This chapter presents a methodology for solving the optimal control problem of solar sails to maximize the displacement in a given direction over one orbit. We introduce a convex relaxation to address the non-convexity of the control set and provide necessary conditions for the problem. Our approach combines convex optimization and shooting, with a bounded polyhedral cone approximation for the set of admissible controls. We formulate the control problem as a semidefinite program, allowing for efficient solution using convex optimization algorithms. Differential continuation and multiple shooting are employed to connect the solutions on the bounded cone and the original control set. A callback procedure handles changes in the control structure. We incorporate the implicit equation defining the control into the shooting procedure to address the absence of an explicit expression for the maximization problem. The methodology is demonstrated with a numerical example of a solar sail maneuver. The results validate the effectiveness of our approach in achieving optimal control and adapting to changes in the solution structure. The proposed methodology provides a systematic and efficient approach for spacecraft maneuvers using solar sails. This chapter is based on the paper whose preprint is available [?] and that studies specifically optimal control for solar sailing application.

Introduction

The possibility to use SRP as an inexhaustible source of propulsion has attracted the interest of researchers in the last decades, therefore leading to several contributions on the guidance and control of solar sails. Specifically, a large body of literature focuses on the mathematical formulation and numerical solution of optimal control problems (OCP) to find minimum-time interplanetary transfer trajectories using optimization techniques with locally-optimal control laws [39, 14], indirect methods [57], neural networks [20] or even a dynamical approach [24]. In addition, several contributions investigate locally-optimal steering laws to maximize the instantaneous rate of change of a desired orbital element, with particular focus on the increase of the semi-major axis for orbit-raising [41] or decrease of the perigee altitude for de-orbiting applications [16]. Classical feedback algorithms are also used to find sub-optimal trajectories, as for instance the Q-law algorithm in [46]. Direct methods are often preferred to find the numerical solution of OCP for solar-sail transfers [12, 50, 51]. This is due to the fact that direct methods do not require an initial guess of the adjoint variables, as opposed to indirect techniques, which - for this reason - have been used in few studies [37, 60, 45, 58, 13].

In Section 3.1 we introduce the optimal control problem of interest in this chapter: it consists in maximizing the displacement of the sail in a given direction over one orbit. A characteristic feature of this problem is the non-convexity of its control set; we define a suitable convex relaxation and review existence and necessary conditions of the original problem, giving precise bounds of the number of switchings of the control. A tailored method of resolution that combines convex optimization and shooting is presented in Section 3.2. While a bounded polyhedral cone allows to approximate the set of admissible controls, a semi-infinite formulation of the control problem is proposed. Using a sum-of-squares approach *à la Nesterov*, this problem is recast as a semi-definite program on the cone of SDP matrices. For such a program, there are efficient convex optimization algorithms with guaranteed convergence properties. The resulting solution is expected to provide an initial guess for shooting. In particular, we rely on the SDP step to capture the switching structure of the optimal control on a bounded cone. Then the solution on this cone is connected to the solution on the original non convex control set by means of differential continuation, coupled with multiple shooting. As the structure of the control may change during continuation (appearance or disappearance of control subarcs), a callback procedure is used to monitor the process and restart it with an updated shooting function. An additional difficulty comes from the fact that there is no explicit expression of the control that maximizes the Hamiltonian coming from Pontryagin maximum principle applied to the problem. This issue is accommodated by incorporating the equation implicitly defining the control into the shooting procedure. The last section is devoted to the

numerical treatment by the described approach of an example coming from the Jet Propulsion Lab: a non-ideal solar sail is considered, and the target is to increase the inclination of the initial orbit. Convex optimization turns to provide a very precise solution to initialize the continuation. A change of structure is nonetheless observed during the early steps of homotopy as the number of arcs drops from three 5 to 3, and the callback is used to eventually obtain the zero-bang-zero optimal control of the sail.

3.1 Control over one orbital period

3.1.1 Optimal control formulation

Consider the same orbital parametrization as in Section 2.4. Dynamics are given by Equation (1.5) and (2.7). We are interested in moving solar sail in the desired direction after one orbital period. Therefore, it is interesting to rewrite System (2.7) in terms of displacement of the slow state elements, as was done in Section 2.4.4 in Equation (2.17). Let us introduce notation $' := \mathrm{d}/\mathrm{d}f$, so that Equation (2.17) can be rewritten as:

$$\delta I' = \varepsilon \check{G}(I, f)u$$

with

$$\check{G}(I, f) := \frac{a\,(1-e^2)^2}{\mu(1+e\cos f)^3}\widetilde{G}(I, f).$$

The goal is to maximize the size of the displacement in a given direction fixed by a unit vector, d_I, so that the final value of δI is parallel to d_I. This problem can be written in Mayer form as follows (note the simple form of the dynamics, given by an explicit integral, as the right-hand side does not depend on δI in our approximation):

$$\max_{u(f)\in U} (\delta I(2\pi)|d_I) \quad \text{subject to} \quad \begin{aligned} &\delta I' = \varepsilon \sum_{i=1}^{3} u_i \check{G}_i(I, f), \\ &\delta I(0) = 0, \\ &\delta I(2\pi) \text{ parallel to } d_I. \end{aligned} \tag{3.1}$$

Building upon results in [30, 9], we have access to an effective test (related to the convex SDP approximation discussed in Section 3.2) to check that it is indeed possible to move in the direction d_I after one revolution. So we assume in the sequel that the problem is controllable.

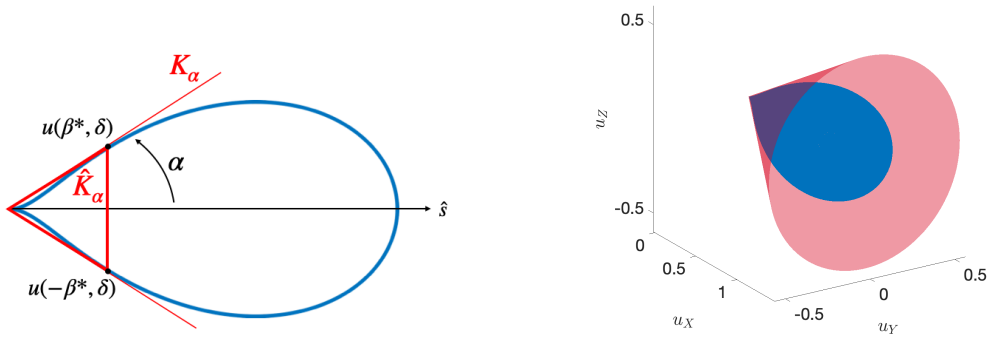

(a) Definition of the convex cone K_α, the bounded cone $\hat{K}_\alpha$ and the critical angle β^*.

(b) View in 3D.

Figure 3.1: Convexification of the control set (in blue) by a convex cone (in red).

3.1.2 Existence and necessary conditions for optimality

We first consider the relaxation of (3.1) obtained by replacing the control set U by its convex hull: $u(f) \in \mathrm{conv}(U)$ (see Figure 3.1). As the control set is now compact and convex, and since we have assumed controllability using controls valued in $U \subset \mathrm{conv}(U)$, Filippov theorem entails that

Proposition 13. *The relaxed problem has a solution.*

Let K_α be the convex cone generated both by U and by its convex hull, α denoting the half-angle at the cone vertex. To formulate the necessary optimality conditions for the problem on $\mathrm{conv}(U)$ we introduce the costate $p_{\delta I}$ of δI, a covector of dimension 5. The Hamiltonian associated with the dynamics is

$$H(I, f, p_{\delta I}, u) = \varepsilon p_{\delta I} \check{G}(I, f) u. \tag{3.2}$$

Remember that I is a constant, and note that the Hamiltonian does not depend on the state δI because of the very simple form of the dynamics. (The ODE defines a mere quadrature, here.) Clearly, $p_{\delta I}$ is constant and transversality conditions write

$$(p_{\delta I} | d_I) = -p^0 \|d_I\|^2 = -p^0 \tag{3.3}$$

where p^0 is the nonpositive multiplier associated with the cost. In particular, $p_{\delta I}$ is not zero, since otherwise both p^0 and $p_{\delta I}$ would vanish. By homogeneity in $(p^0, p_{\delta I})$ there are two cases: (i) the abnormal case ($p^0 = 0$) when $(p_{\delta I}|d_I) = 0$ and where one can normalize setting $\|p_{\delta I}\| = 1$; (ii) the normal case ($p^0 < 0$) when $(p_{\delta I}|d_I) > 0$ and where one can normalize setting $(p_{\delta I}|d_I) = 1$. Let us set $\psi := p_{\delta I} \check{G}(I, f)$.

Lemma 14. *For any I, the matrix formed by $\check{G}(I,f)$ and $\partial\check{G}(I,f)/\partial f$ has maximum rank for all $f \in [0,2\pi]$.*

Proof. This computation is actually equivalent to the rank condition that can be verified in terms of Lie brackets (and, *e.g.*, Cartesian coordinates) in [8] (check Lemma 1). □

As a result, the zeros of the dimension three covector ψ (as a function of the true anomaly f) are isolated on $[0,2\pi]$. Indeed, the previous lemma implies that ψ and $\mathrm{d}\psi/\mathrm{d}f$ cannot vanish simultaneously as then, $p_{\delta I}$ would be orthogonal to all columns of $\check{G}(I,f)$ and of its derivative, so $p_{\delta I}$ would be zero (a contradiction). So there are only finitely many such zeros on $[0,2\pi]$, defining a locus of codimension greater than one in the (I,f) space. For the sake of simplicity, we assume in the sequel that ψ actually never vanishes. For a detailed discussion on the associated singularities of the dynamics, see [10].

The polar cone K_α^0 is the set of directions having a nonpositive scalar product with those in K_α. The drop-shaped curve obtained when intersecting the control set with a plane is parametrized by the angle β alone, and $\beta^* \in (0,\pi/2)$ is the parameter associated with the tangency point of this curve with its conical hull (see Figure 3.1a), defined in Equation (2.9). Thus, angle α of the convex cone can be retrieved from the critical angle β^* using Equation (2.10).

In the sequel, we recall and complete the analysis from [42], providing precise bounds on the number of switchings on the control.

Proposition 15. *An optimal control u verifies the following: (i) when ψ belongs to the interior of K_α^0, u is zero; (ii) when ψ does not belong to K_α^0, the coordinates (β,δ) of the control verify the following relations:*

$$\frac{\sin\beta(b_1+3b_2\cos^2\beta+2b_3\cos\beta)}{\big(\cos^2\beta(b_2\cos\beta+b_3)-\sin^2\beta(2\,b_2\cos\beta+b_3)\big)}=\frac{\sqrt{\psi_2^2+\psi_3^2}}{\psi_1},\ \beta\in(-\beta^*,\beta^*), \tag{3.4}$$

and

$$\delta=\pi/2-\arg(\psi_2+i\psi_3)\ \mathit{mod}\ \pi. \tag{3.5}$$

Moreover, any optimal control is made of finitely many subarcs corresponding to case (i) or (ii), and has at most 8 switchings (transverse contacts with ∂K_α^0) over one period.

Proof. According to PMP and to the expression (3.2) of the Hamiltonian, for almost all true anomaly f an optimal control must be a maximizer of the scalar product $(\psi|u)$ for u in $\mathrm{conv}(U)$. Clearly, when ψ belongs to the interior of the polar cone of K_α, this scalar product is negative for any nonzero u, so $u=0$ is the only maximizer. Conversely, when ψ belong to the open complement of K_α^0,

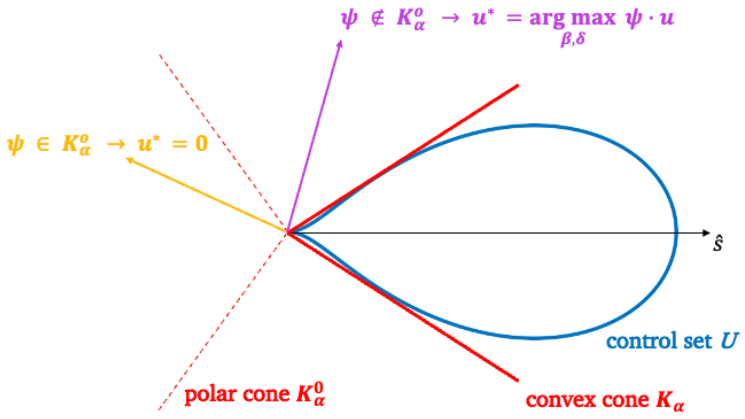

Figure 3.2: Geometrical interpretation of the PMP.

maximizers must annihilate the gradient of the Hamiltonian with respect to the chosen coordinates of the control,

$$\frac{\partial H}{\partial \beta} = 0, \quad \frac{\partial H}{\partial \delta} = 0,$$

which gives the expressions in alternative (ii) of the statement. See Figure 3.2 for the geometrical interpretation. Moreover, ψ belongs to the boundary of K_α^0 if and only if $\psi_1 \cos\alpha + \sqrt{\psi_2^2 + \psi_3^2}\,\sin\alpha = 0$, implying that

$$\psi_1^2 \cos^2\alpha - (\psi_2^2 + \psi_3^2)\sin^2\alpha = 0. \tag{3.6}$$

Every component of ψ is trigonometric in f, and this (nontrivial) equation results in a trigonometric polynomial of degree 4. As it has isolated zeros, there are finitely many zeros (at most eight, see Remark 17) defining isolated contacts with ∂K_α^0. □

Remark 16. *Equation* (3.4) *defines the optimal solution* β *as an implicit function of* ψ *and optical parameters of the sail, notably,* b_1, b_2, b_3*. This relation becomes explicit when considering an ideal solar sail model, what is widely used in the literature for different preliminary analysis design. In this case,* $b_1 = b_3 = 0$*, and* $b_2 = 2$*. Therefore, Equation* (3.4) *becomes:*

$$6\,\psi_1 \sin\beta \cos^2\beta = \sqrt{\psi_2^2 + \psi_3^2}\left(2\cos^2\beta\cos\beta - 4\sin^2\beta\cos\beta\right), \quad \beta \in (-\beta^*, \beta^*),$$

leading to the classical well-known near-optimal steering law for an ideal sail[40]:

$$\beta = \tan^{-1}\left(\frac{-3 + \sqrt{9 + \frac{\psi_2^2+\psi_3^2}{\psi_1^2}}}{4\frac{\psi_2^2+\psi_3^2}{\psi_1^2}}\right)$$

Remark 17. *Roots of a trigonometric polynomial can be found using companion-matrix methods [6]. Consider the degree* 4 *polynomial*

$$\mathcal{T}(f) = \sum_{j=0}^{4} a_j \cos(jf) + \sum_{j=1}^{4} b_j \sin(jf).$$

Fourier-Frobenius companion matrix elements are

$$B_{jk} = \begin{cases} \delta_{j,k-1}, & j = 1, \ldots, 7,\ k = 1, \ldots, 8, \\ (-1)\dfrac{h_{k-1}}{a_4 - ib_4}, & j = 8,\ k = 1, \ldots, 8, \end{cases} \tag{3.7}$$

where δ_{jk} *are the Kronecker functions such that* $\delta_{jk} = 0$ *if* $j \neq k$ *and* $\delta_{jj} = 1$*, and* h_k *are*

$$h_k = \begin{cases} a_{4-k} + ib_{4-k}, & k = 0, \ldots, 3, \\ 2a_0, & k = 4, \\ a_{k-4} - ib_{k-4}, & k = 5, \ldots, 8. \end{cases}$$

The roots of $\mathcal{T}(f)$ *are obtained from eigenvalues* z_k *of the matrix defined in Equation* (3.7) *as*

$$f_{k,m} = arg(z_k) - i\log(|z_k|)\ mod\ (2\pi), \quad k = 1, \ldots, 8.$$

Real-valued roots of $\mathcal{T}(f)$ *are such that* $|z_k| = 1$*. Therefore, this technique allows to find roots of the switch function and, thus, find out the structure of the solution for a given costate. It is important to stress that the trigonometric polynomial is of degree* 4*, which means that the switching function can have at most* 8 *roots.*

Corollary 18. *The original optimal control problem* (3.1) *has a solution.*

Proof. The relaxed problem has at least one solution (Proposition 13), and any control solution actually belongs to U by virtue of Proposition 15. Such controls must be optimal for the original problem, whence existence. □

3.2 Solution using convex optimization and continuation

3.2.1 Convex approximation for a reliable initial guess

In order to use indirect shooting methods for solving optimal control problem, we need first a reliable initial guess for the costate $p_{\delta I}$. We propose an approximation by a convex mathematical program similar to the one used in [30] for controllability check purposes. To this end, define the bounded cone $\hat{K}_\alpha$ obtained by truncating the K_α at its tangency points with U (check Figure 3.3a). This cone

is bounded by a disk denoted D_α. This new control set is a subset of the convex hull of U, in order that any solution of

$$\max_{u(f)\in\hat{K}_\alpha} (\delta I(2\pi)|d_I) \quad \text{subject to} \quad \begin{array}{l} \delta I' = \varepsilon \sum_{i=1}^{3} u_i \check{G}_i(I,f), \\ \delta I(0) = 0, \\ \delta I(2\pi) \text{ parallel to } d_I, \end{array} \tag{3.8}$$

will define an admissible control for the convex relaxation of the original control problem. Note that existence holds for this new problem (Filippov again, as $\hat{K}_\alpha$ is convex and bounded) and that any solution will also have a bang-bang structure. A similar analysis to the one of Section 3.1.2 on $\mathrm{conv}(U)$ indeed allows to prove that

Proposition 19. *An optimal control u of problem (3.8) on $\hat{K}_\alpha$ verifies the following: (i) when ψ belongs to the interior of K_α^0, u is zero; when ψ does not belong to K_α^0, (ii-a) the control is uniquely determined and belongs to the circle ∂D_α, unless (ii-b) ψ is colinear to the axis $\hat{s}$ of the cone K_α in which case the control still belongs to the ∂D_α but is not uniquely determined, as shown in Figure 3.3b. Moreover, any optimal control is made of finitely many subarcs corresponding to case (i) or (ii-a) over one period.*

Proof. As $\hat{K}_\alpha$ and K_α have the same polar cone, (i) is clear. Conversely, when ψ belongs to the open complement of K_α^0, the colinearity condition $\psi \wedge \hat{s} = 0$ boils down to checking a polynomial condition in f and has only isolated zeros corresponding to case (ii-b). When ψ is not colinear to $\hat{s}$, the unique maximizer of $(\psi|u)$ for u in $\hat{K}_\alpha$ indeed belongs to the circle ∂D_α, which is case (ii-a). □

This structure being analogous to that of solutions of the original problem, one hopes to retrieve a reasonable approximation to be used to initiate a differential continuation (see Section 3.2.2). In particular, we note that the original problem (3.1) on U and problem (3.8) on $\hat{K}_\alpha$ share the same switching function associated with contacts with ∂K_α^0 and given by (3.6).

Consider the following discretization of (3.8): the control set $\hat{K}_\alpha$ is approximated by a polyhedral cone $\hat{K}_\alpha^g \subset \hat{K}_\alpha$ generated as the convex hull of g vertices $V_1, \ldots, V_g$ chosen in $\partial\hat{K}_\alpha$, as shown on Figure 3.4. (Note that the 3D cone $\hat{K}_\alpha$ is not finitely generated.) Any control in $\hat{K}_\alpha^g$ is given by a bounded conical combination

$$u(f) = \sum_{j=1}^{g} \nu_j(f) V_j, \quad \nu_j(f) \geq 0, \quad \sum_{j=1}^{g} \nu_j(f) \leq 1, \quad f \in \mathbf{S}^1, \quad j = 1, \ldots, g.$$

The functions ν_j are modeled using an N-dimensional basis of trigonometric

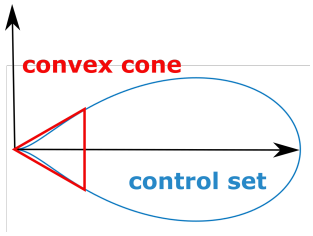

(a) Approximation of the control set by a cone bounded at the points of tangency.

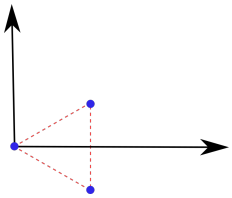

(b) Optimal solution will be given by two controls on the boundary of the cone or a zero. Controls on the boundary of the cone are actually situated on a circle, illustrated here by two dots projected on the two-dimensional plane.

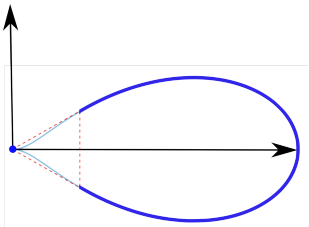

(c) Possible optimal solutions on the real control set.

Figure 3.3: Approximation of the control set by a convex cone.

polynomials, $\Phi(f) = \left(1, e^{if}, e^{2if}, \ldots, e^{(N-1)if}\right)$:

$$\nu_j(f) = \left(\Phi(f) \mid c_j\right)_H$$

with $c_j \in \mathbf{C}^N$ complex-valued coordinates of ν_j in $\Phi(f)$. To enforce the positivity constraint, similarly to Section 2.4.4, we leverage on the formalism of squared functional systems outlined in [44]. For an admissible control u valued in $\hat{K}^g_\alpha$, one has

$$\int_0^{2\pi} \sum_{i=1}^{3} u_i(f) \check{G}_i(I, f)\, \mathrm{d}f = \sum_{j=1}^{g} \left(L_j c_j + \bar{L}_j \bar{c}_j\right)$$

with $L_j(I)$ in $\mathbf{C}^{5\times N}$ defined by

$$L_j(I) = \frac{1}{2} \sum_{i=1}^{3} \int_{\mathbf{S}^1} V_{ij} G_i(I, f) \Phi^H(f)\, \mathrm{d}f,$$

where $V_j = (V_{ij})_{i=1,\ldots,3}$. We note that the components of $L_j(I)$ are Fourier coefficients of the function $\sum_{i=1}^{3} V_{ij} \check{G}_i(I, f)$. $L_j(I)$ are approximated using the DFT. Since vector fields $\check{G}_i$ are smooth, truncation of the series is justified by the fast decrease of the coefficients. Finally, for a control u valued in $\hat{K}^g_\alpha$, coefficients ν_j are truncated Fourier series of order $N-1$. As a result, for a given vector d_I,

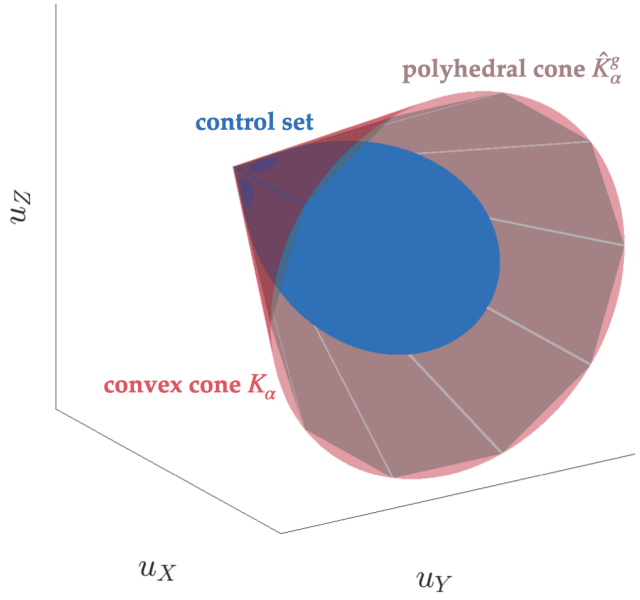

Figure 3.4: Approximation of the convex cone K_α by a polyhedral cone $\hat{K}_\alpha^g$.

the SDP approximation is

$$\max_{c_j \in \mathbf{C}^N,\ Y_b, Y_j \in \mathbf{C}^{N\times N}} (\delta I | d_I) \quad \text{subject to} \quad \begin{aligned} &\delta I = \varepsilon \sum_{j=1}^{g} \left(L_j c_j + \bar{L}_j \bar{c}_j \right) \text{ parallel to } d_I \\ &Y_j \succeq 0, \quad \Lambda^* (Y_j) = c_j, \quad j = 1, \ldots, g, \\ &Y_b \succeq 0, \quad \Lambda^* (Y_b) = (1, 0, \ldots, 0) - \sum_{j=1}^{g} c_j. \end{aligned}$$

The Lagrange variable of the discretization of the equality constraint that δI is parallel to d_I from the convex program is expected to be a fair approximation of the costate $p_{\delta I}$ of (3.8). More importantly, it is hoped that the bang-bang control structure associated with this $p_{\delta I}$ is indeed the same as for the solution of the problem defined on $\hat{K}_\alpha$.

3.2.2 Multiple shooting, differential continuation and callback

Homotopy, *aka.* continuation, allows to solve a complex problem by connecting it continuously to a simpler problem. The idea is then to follow the path (assumed to be regular enough) of solutions from the simpler problem towards the targeted one. See, *e.g.*, [25, 64] for applications in optimal control. In our case, a parameter λ defined between 0 and 1 allows to connect the problem with control set the bounded convex cone $\hat{K}_\alpha$ at $\lambda = 0$, to the original problem with the non-convex

drop-like control set U at $\lambda = 1$. In order to be able to solve the problem for $\lambda = 0$, we rely on the solution of the convex program on $\hat{K}^g_\alpha$ to provide an admissible solution. This solution is used not only to compute an educated guess for the initial costate but also to devise the appropriate multiple shooting function. To do so, we use the control structure corresponding to the approximation of $p_{\delta I}$ provided by the convex optimization and described at Proposition 19. This proposition tells us that, when ψ (a function of $p_{\delta I}$ and f) belongs to the open complement of the polar cone K^0_α, the control must be equal to the *dynamical feedback* described in case (ii-a) (apart for some isolated points that correspond to case (ii-b) that we can neglect); we denote $u^0_b(f, p_{\delta I})$ this control. Similarly, for such values of ψ, Proposition 15 for the problem on $\mathrm{conv}(U)$—and actually U, check Corollary 18—, implies that the control must be a solution of (3.4)-(3.5). (While these equations provide an explicit solution for the coordinate δ of the control, β is only implicitly defined and we discuss its actual computation in Section 3.2.3.) We assume that this solution is unique and denote it $u^1_b(f, p_{\delta I})$. Then, for λ in $[0, 1]$ and ψ outside the polar cone, we define

$$u_b(f, p_{\delta I}, \lambda) := (1 - \lambda)u^0_b(f, p_{\delta I}) + \lambda u^1_b(f, p_{\delta I})$$

as the convex combination of the dynamical feedbacks for $\lambda = 0$ and $\lambda = 1$. Conversely, for any λ in $[0, 1]$ and ψ in the interior of the polar cone, the control is set to zero.

For a given λ, one has a finite sequence of arcs with either $u = u_b$ (bang arcs), or $u = 0$ (zero arcs). Contacts with ∂K^0_α are characterized by (3.6) whose left-hand side defines the switching function, denoted $\varphi(f, p_{\delta I})$ (not depending on λ in our particular setting). To this finite sequence of arcs is associated a multiple shooting function in a standard fashion. Assume for instance that the structure is bang-zero-bang. Then the shooting function has three arguments: the (constant) value of the costate, $p_{\delta I}$, and the two switchings times (true anomalies) bounding the central zero arc, f_1 and f_2. (So that $(p_{\delta I}, f_1, f_2)$ belong to $\mathbb{R}^7$.) Plugging $u = u_b(f, p_{\delta I}, \lambda)$ into the dynamics of δI and integrating on $[0, f_1]$ from $\delta I(0) = 0$ allows to compute $\delta I_1 := \delta I(f_1)$. As the control is zero on $[f_1, f_2]$, δI remains constant on the coast arc and we set $\delta I_2 := \delta I_1$. The control $u = u_b(f, p_{\delta I}, \lambda)$ is eventually plugged again on $[f_2, 2\pi]$ to compute $\delta I_f := \delta I(2\pi)$, starting from δI_2. The associated value of the shooting function is obtained by concatenating the left-hand side of the four equations below, forming a vector of dimension $4 + 1 + 2 = 7$ (note that the first colinearity equation indeed has dimension $5 - 1 = 4$):

$$\begin{aligned} \delta I_f \wedge d_I &= 0, \\ (p_{\delta I} | d_I) - 1 &= 0, \\ \varphi(f_1, p_{\delta I}) &= 0, \\ \varphi(f_2, p_{\delta I}) &= 0. \end{aligned}$$

This defines a shooting function $S(\xi, \lambda)$ with, for this bang-zero-bang structure, $\xi := (p_{\delta I}, f_1, f_2)$. Once the first solution for $\lambda = 0$ is obtained, the path of zeros is followed by differential continuation, typically using a parametrization by its curvilinear abscissa:

$$s \mapsto (\lambda(s), \xi(s)) \text{ with } S(\xi(s), \lambda(s)) = 0.$$

We refer, *e.g.*, to [**?**] for the assumptions needed to do so. Note that, according to (3.11), we look for normal extremals (compare with (3.3)).

One important issue in practice is that it might not be possible to reach $\lambda = 1$ because, at some $\lambda(\bar{s})$ in $(0, 1)$, the structure of the solution changes; for instance because one subarcs disappears. It is crucial to be able to detect such a change during homotopy since then, the shooting function has to be redefined according to the new structure. This is achieved using a standard callback mechanism along with differential continuation. On the previous bang-zero-bang example, the continuation is monitored and, at each step of the path following procedure, a simple test is performed: if the exit time of the zero arc, f_2, becomes inferior to the entry time f_1 (this is detected by a sign change on $f_2 - f_1$, as going forward in time makes sense mathematically but is not allowed to obtain admissible trajectories), the continuation is stopped. And restarted at $\lambda(\bar{s})$ with a new shooting function (in this case, a single shooting one, as only one bang arc would be left), using $\xi(\bar{s})$ as initial guess. More elaborated tests can be constructed to detect a new arc appearing, *etc.* In our case, a callback is used to detect a structure change from 5 subarcs to 3 (see Section 3.3). This methodology can readily be extended to any other structure with a finite number of arcs.

3.2.3 Implicit treatment of the Hamiltonian maximization

Regarding the computation of $u_b^1(f, p_{\delta I})$, we know after Proposition 15 that the control is either zero, either solution of (3.4-3.5). The first equation for the coordinate β of u has no closed form solution. There is a preliminary numerical discussion of the number of solutions in [42] (we actually look for a global maximizer of the Hamiltonian over U, which may allow to eliminate some strictly local minimizer that also verify (3.4)) for a particular set of values of the sail parameters. More generally, while maximization of the Hamiltonian often yields an explicit expression of the control as a dynamics feedback function of the state and the costate, it is not always the case. In such a situation, we advocate an implicit treatment of this maximization, incorporating the stationarity equation of the Hamiltonian into the shooting procedure. We sketch below a simple way to do so in a general setting.

Assume that, after applying Pontryagin maximum principle, one has to integrate the following system (x denoting the state, p the costate):

$$\dot{x}(t) = \nabla_p H(x(t), p(t), u(t)), \quad \dot{p}(t) = -\nabla_x H(x(t), p(t), u(t)), \tag{3.13}$$

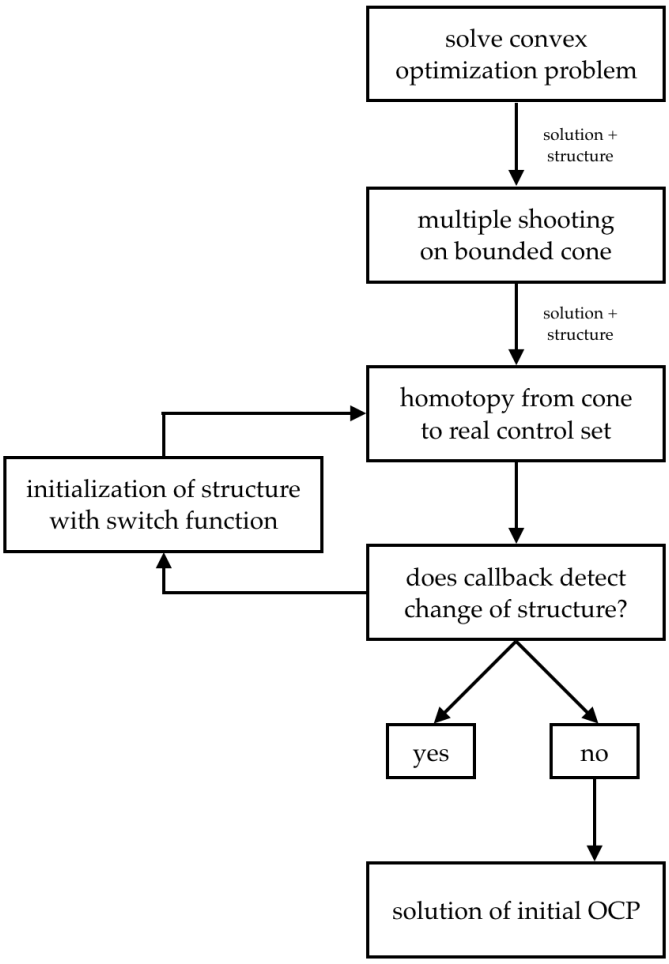

Figure 3.5: Algorithm for solving OCP.

where, at each time t, the m-dimensional control $u(t)$ verifies

$$\nabla_u H(x(t), p(t), u(t)) = 0. \tag{3.14}$$

The last stationarity equation corresponds to an unconstrained situation—whereas a Lagrangian, plus an additional finite dimensional multiplier, should be considered in the presence of constraints—, and defines a semi-explicit differential-algebraic-equation. Assume that the strong Legendre-Clebsch condition holds in an open neighborhood of the reference extremal times the open control set, $\nabla^2_{uu} H \preceq -cI_m$ for some positive constant c. Then the Hamiltonian has a unique maximizer, that satisfies $\nabla_u H = 0$, and the previous differential-algebraic equation (DAE) is of index 1 (differentiating once (3.14) allows to solve for $\dot{u}$). In particular, one can extend the Hamiltonian system (3.13) by adding the equation

$$\dot{u} = -\nabla^2_{uu} H^{-1} (\nabla_{ux} H \cdot \nabla_p H - \nabla_{up} H \cdot \nabla_x H)(x, p, u) := g(x, p, u),$$

with initial condition $\nabla_u H(x(0), p(0), u(0)) = 0$. The new system remains Hamiltonian as is clear setting $\hat{x} := (x, u)$, $\hat{p} := (p, p_u)$ and

$$\hat{H}(x, u, p, p_u) := H(x, p, u) + (p_u | g(x, p, u))$$

with $p_u(0) = 0$. (One can obviously eliminate the trivial equation on p_u, which is an extra but identically zero costate.) In the case of a shooting approach, the value of $u(0)$ is an additional shooting variable. Keeping the system in Hamiltonian form is convenient in the algorithmic framework described in Section 3.3, but other approaches for DAE such as predictor-corrector ones can of course be considered. In our case, we use this approach with $x = \delta I$, $p = p_{\delta I}$ to deal with the implicit equation (3.4) on β (while we use (3.5) to solve it explicitly for δ). The combination of this implicit approach with multiple shooting, homotopy and callback is described in the last section.

3.3 Numerical example

This section presents the results for a specific example of a trajectory around a planet, where a change in the solution's structure occurs during the process of differential continuation. It is important to note that, in our simulations, such a change in structure is more of an exception rather than the norm. The majority of the simulated trajectories exhibited the same structure for the control set, which was represented by a bounded cone and a drop-like set. However, we present this particular example to highlight the situation where the structure differs, necessitating the use of a callback and a switch function to reinitialize the multiple shooting algorithm.

Consider a solar sail whose optical properties determining shape of U are taken from Jet Propulsion Laboratory (JPL) Square Sail defined in [40, Table 2.1]:

$$\rho = 0.88,\ s = 0.94,\ \varepsilon_b = 0.55,\ \varepsilon_f = 0.05,\ B_b = 0.55,\ B_f = 0.79.$$

An initial orbit is determined by

$$I = (10^\circ, 50^\circ, 30^\circ, 1, 0.1).$$

The desired maneuver to be performed is increase of the inclination γ_2, what gives $d_I = (0, 1, 0, 0, 0)$. Initially, an optimization problem is solved to obtain the optimal solution for the control on the bounded polyhedral cone, $\hat{K}^g_\alpha$. This result serves as a reliable initial guess for the optimal control problem (OCP) being considered. The solution consists of five arcs, with the first arc being zero. The costate is

$$p^{conv}_{\delta I} = (-0.0837, 1, -0.0052, 0.0398, 0.0852).$$

Switches between zeros and bangs occurs at

$$f_1 = 49.4^\circ, f_2 = 237.9^\circ, f_3 = 265.6^\circ, f_4 = 286.9^\circ.$$

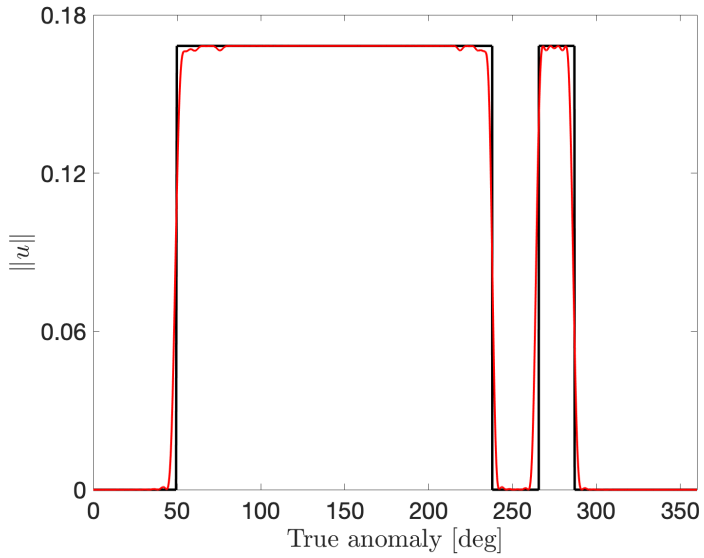

Figure 3.6: Results from convex optimization (in red) on $\hat{K}_\alpha^g$ compared to multiple shooting on $\hat{K}_\alpha$ with $\lambda = 0$ (in black).

We substitute the values $(p_{\delta I}, f_1, f_2, f_3, f_4)$ into the multiple shooting algorithm to solve the problem on the bounded cone $\hat{K}_\alpha$, with the continuation parameter $\lambda = 0$. The resulting controls are depicted in Figure 3.6, illustrating the norm of the control u. The red line represents the controls obtained through convex optimization on the polyhedral cone, which leads to some oscillations due to the linear combinations of a finite number of generators on the cone. In contrast, the black curve corresponds to the controls derived from the multiple shooting approach on the bounded cone. Since no discretization is involved, the line appears smooth. Both solutions are remarkably similar, providing evidence that convex optimization serves as a highly accurate approximation for the initial guess with $\lambda = 0$.

During the process of differential continuation using the previous solution, as expected, the callback function detects the disappearance of an arc, resulting in $f_4 < f_3$, which is physically impossible. This occurrence takes place at approximately $\lambda = 0.0256$, a relatively small value. This indicates that by "inflating" the control set, a better solution quickly emerges, leading to the removal of the second arc. Utilizing the switch function, the algorithm reconfigures the solution structure by eliminating the second arc, resulting in a zero-bang-zero structure. The algorithm continues the homotopy process, ultimately arriving at the final solution on the real control set with $\lambda = 1$.

Figure 3.7 presents the solutions throughout the process. In Figure 3.7a, the solutions are shown starting from $\lambda = 0$ in black and progressing until $\lambda = 0.0256$

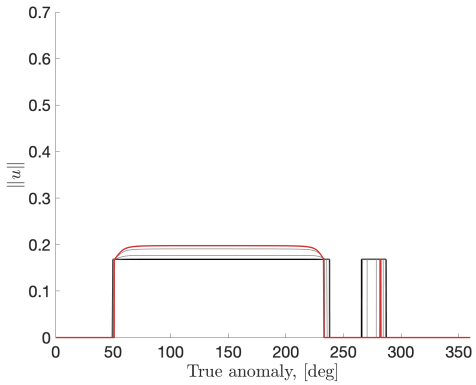

(a) Homotopy from the solution with $\lambda = 0$ in black till the moment when structure of the solution changes, notably $\lambda = 0.0256$, depicted in red. Intermediate solutions are represented in gray.

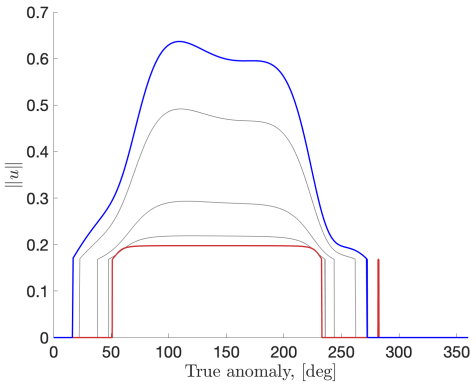

(b) Homotopy from the moment when change of structure occurs for $\lambda = 0.0256$, depicted in red, till the final solution with $\lambda = 1$, represented in black. Intermediate solutions are represented in gray.

Figure 3.7: Deformation of the solution along the differential continuation.

in red, which is when the second arc disappears. The gray curves illustrate the deformation of the solution as differential continuation is performed. At the point when $\lambda = 0.0256$, the structure of the solution is reinitialized, as depicted in Figure 3.7b. The subsequent continuation process leads to the final result at $\lambda = 1$, shown in blue. The final solution corresponds to the costate equal to

$$p_{\delta I}^{sol} = (-0.1637, 1, -0.0972, 0.0712, 1.6037).$$

Figure 3.8 shows the solution on the real control set in terms of control angles, defining attitude of the solar sail. When $\beta = \frac{\pi}{2}$, it means that the sail is aligned with the solar rays, so that no surface is exposed to the solar light, what corresponds to $\|u\| = 0$. In this case δ angle is not defined.

Convex optimization is done using CVX package in Matlab [26, 27]. Multiple shooting with differential continuation is performed using *control toolbox (CT)* developed in python. An example of the code which is executable online is available.[1]

To verify the accuracy of the solution, we integrate the trajectory of the initial system using the provided solution. Figure 3.9 depicts the dynamics of each of the five orbital elements over one orbit. The magnitude of the displacement, δI, depends on the parameter ε of the sail. However, since it does not impact the interpretation of the results, we normalize the displacement. As shown, all orbital parameters remain constant after the orbital period, except for γ_2, which continues to increase. It is important to note that our algorithm assumes a fixed

[1] ct.gitlabpages.inria.fr/gallery/solarsail/solarsail-simple-version-implicit.html

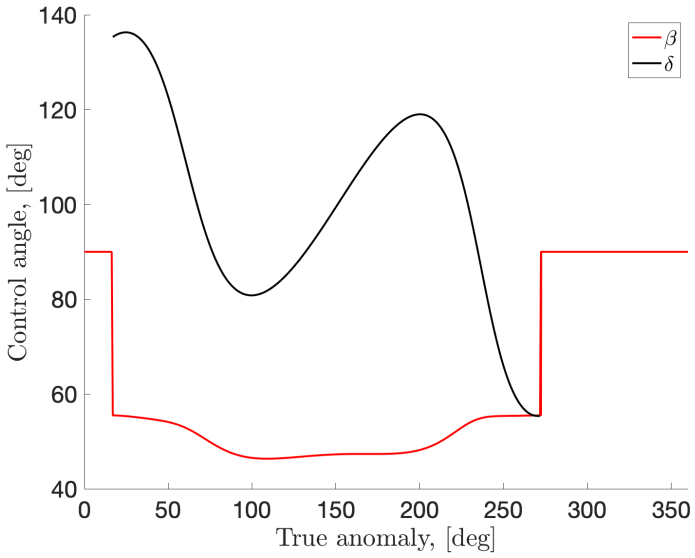

Figure 3.8: Controls in terms of orientation angles of the sail.

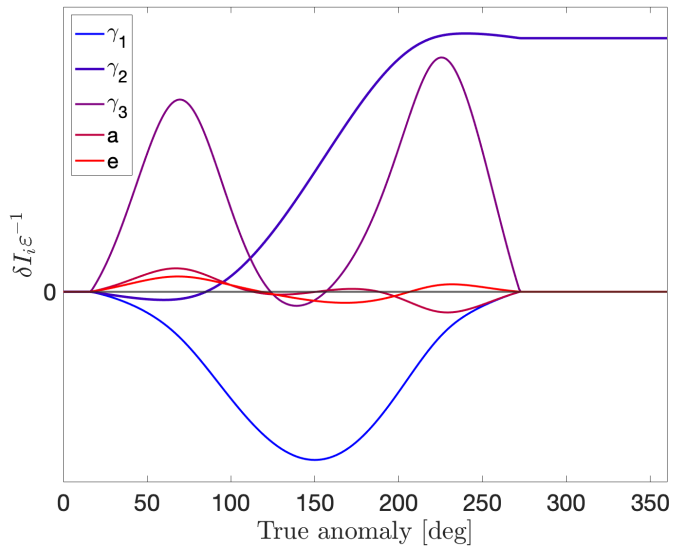

Figure 3.9: Integration of the dynamics using the optimal control solution.

state for one orbital period, but the final integration is performed using the actual dynamics. As expected, divergence becomes noticeable after integrating for 10 or more orbits, which is consistent with the fact that the optimal control is provided for the initial orbit. Ideally, the proposed methodology should be utilized as a feedback control system to determine the optimal trajectory for each orbital period, requiring reinitialization after each orbit.

Conclusion

This chapter presented a methodology for the design of optimal maneuvers of a non-ideal solar sail in orbit around a celestial body. The maneuver is aimed at obtaining a displacement toward a precise direction of the phase space. Cost function is the magnitude of such displacement. A reliable initial guess for the convergence of the shooting function is provided by the outcome of a convex optimization, which ensures the feasibility of the maneuver. The existence of a finite number of bangs over one orbit is another major outcome of this study, which may apply to other transfers problems characterized by cone constraints on the control set. The proposed algorithm can be implemented as a feedback control system, enabling the satellite to modify its trajectory or perform station-keeping maneuvers. The methodology could be straightforwardly extended to multi-revolution transfers.

Chapter 4

Sun occultation mission by natural bodies

Observation of solar corona, the outer layer of the Sun's atmosphere, poses challenges due to its low brightness compared to the solar disk. In this chapter, we investigate a space mission that utilizes Earth as an occulting body for the Sun in order to enhance visibility of the solar corona for observations using solar sails. We formulate an optimal control problem to minimize the total time of a controlled periodic orbit passing through the observation zone where the corona is visible. By applying the Pontryagin's maximum principle, we derive optimality conditions and employ indirect shooting techniques to find the optimized trajectory. Differential continuation techniques are utilized to explore optimal orbits for solar sails of varying configurations.

Introduction

In recent times, numerous satellites have been lost as a result of geomagnetic storms [36]. These storms, which are caused by eruptions from the surface of the Sun, result in an influx of particles into the atmosphere [63]. This increase in particles leads to a rise in atmospheric temperature, as well as an increase in atmospheric drag, what can cause satellites in low orbit to deorbit [56, 48]. Geomagnetic storms are one of the many phenomena that occur due to the constant evolution of the solar corona, the outermost layer of the Sun's atmosphere that extends millions of kilometers into space. The corona is a region of plasma that is hotter and less bright than the surface of the Sun. The evolution of the corona is responsible for space weather on Earth, which is crucial for designing space missions and launching satellites. However, due to the challenges in observation, our understanding of the solar corona remains limited [18]. To observe it, special instruments called coronographs are used to occult the Sun's disk. Alternatively, observations can be made during rare eclipses to study the corona in more detail, as shown in Figure 4.1. However, ground-based measurements suffer from scattering due to the atmosphere.

A novel concept was recently proposed, which consists of using natural bodies as occulting disks [23]. The idea is to place a satellite in proximity of the tip of the umbra cone generated by a celestial body (*e.g.*, Earth or Moon). Assuming that electrical power is gathered via solar panels, the satellite is constrained to periodically leave the observation zone end expose itself to sunlight to recharge its batteries and heat up. The possibility of using a solar sail to maneuver the satellite in a propellantless fashion was suggested by a team from Surrey Space Centre [2]. Their preliminary analysis showed that using a solar sail to accomplish this mission was promising, but that study considered an ideal sail with unrealistically-large surface-to-mass ratio. In this section, we investigate further the possibility to use solar sails in the context of the Sun occultation mission by offering a detailed study of optimal maneuvers for repeated observations by means of a non-ideal sail. The CRTBP (Earth-Sun system, where Earth serves as occulting body) is used to model the motion of the satellite. The trajectory design is formulated as a periodic optimal control problem aimed at minimizing the maneuvering time for a fixed duration of the observations. Integral of the incoming sunlight is part of the state variables, and it serves as a rough indicator of the charge of the batteries. PMP is then applied to deduce necessary conditions for optimality of the problem. Numerical solutions are achieved by using indirect techniques. Differential continuation is applied to investigate how the surface-to-mass ratio of the sail, its optical properties, and the imposed amount of sunlight exposure impact the trajectory.

Figure 4.1: Solar corona visible during the eclipse of August 2017. Credit: NASA/Aubrey Gemignani

4.1 Mission concept and interest of solar sailing

Figure 4.2 illustrates the geometry of the problem, including the so-called occultation zone which indicates the region where the Sun's corona can be observed while its disk is hidden. As depicted in the figure, the occultation zone is located far from the L_2 point, making it unsuitable for placing the spacecraft on any of its periodic orbit families. Additionally, an uncontrolled satellite located within the observation zone, with zero relative velocity, will inevitably drift away and enter the penumbra region. In the penumbra, the Sun is partially eclipsed, and the satellite is exposed to a limited amount of sunlight. Although long-lasting, uninterrupted observations of the corona are desirable, technological constraints impose that the satellite periodically leaves the observation zone to receive some incoming sunlight in order to raise its temperature and recharge batteries.

The rationale behind the design of periodic observations proposed in [2] is illustrated in Figure 4.2, and it can be summarized as:

- The satellite is first placed inside the occultation zone on the Sun-Earth axis with zero velocity, *i.e.*, the zero-velocity curve of the uncontrolled motion crosses the observation zone. Duration of the observations depends on the abscissa of the Sun-Earth axis crossing, an it can be as large as few days. In that study, 24-hour observations were envisaged.

- A coasting arc is then executed. Here, the satellite will first leave the observation zone and cross the penumbra region until it is exposed to full sunlight. Few more time is then spent in sunlight to fulfill mission

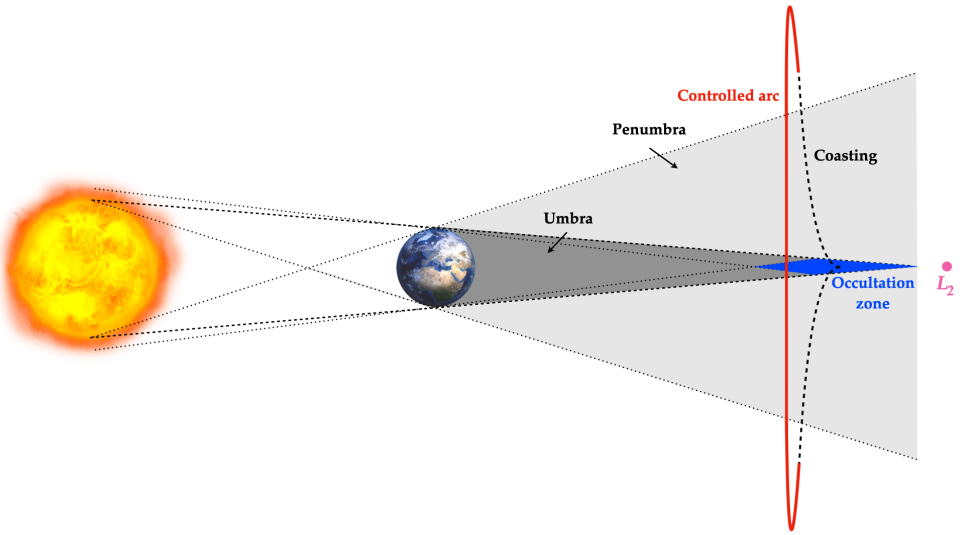

Figure 4.2: Geometry of the sun occultation zone.

requirements on satellite temperature raise and battery recharge. Specifically, two hours were claimed to be enough for this purpose.

- A controlled arc is afterwards implemented to mirror satellite's state at the end of the coasting arc with respect to the Earth-Sun axis. Specifically, endpoint conditions are such that the abscissa is the same of the initial point while all other components of position and velocity vectors have opposite sign.

- Finally, the satellite will naturally coast to the initial position (inside the observation zone), because of symmetric properties of trajectories in the CRTBP.

In [2], the authors explored various propulsion options to achieve the controlled arc. They concluded that chemical and low-thrust propulsion are not viable options to carry out repeated observations owing to the large ΔV required for a single orbit. Conversely, solar sails were identified as a promising technology because of their propellantless nature. The SRP-actuated trajectory that they found was characterized by a period of only a couple of days longer than the 45-day cycle of low-thrust trajectories. Nevertheless, the authors considered a perfectly reflective solar sail with a non-realistic size-to-mass ratio, which is the main limitation of the achieved results. In the following section, we propose a more detailed analysis of feasibility of the sun occultation mission by solar sailing.

4.2 Optimal control problem

Consider System (1.6) with the state $x = (r, v)$ position and velocity of the satellite in the standard synodic frame of the planar CRTBP. Because the satellite will transit through umbra and penumbra regions, where the quantity of incoming light is decreased by total and partial eclipses, respectively, we introduce the lightning factor $\tau(x)$, which scales the SRP force according to the received sunlight. This coefficient is a function of the position of the sail with respect to the Sun, and it is computed as [2]:

$$\tau(x) = \begin{cases} \tau = 1 & \text{if } a + b \leq c \\ \tau = 0 & \text{if } c \leq |b - a| \\ \tau = 1 - \frac{A}{\pi a^2} & \text{otherwise,} \end{cases}$$

where

$$a = \arcsin\left(\frac{R_\odot}{\|r_1\|}\right)$$
$$b = \arcsin\left(\frac{R_\oplus}{\|r_2\|}\right)$$
$$c = \arccos\left(\frac{r_1}{\|r_1\|} \cdot \frac{r_2}{\|r_2\|}\right)$$

with $R_\odot = 695550, R_\oplus = 6378.137$ being respectively Sun and Earth radius in km, and A is the visible area of the Sun's disk:

$$A = a^2 \arccos\left(\frac{\chi}{a}\right) + b^2 \arccos\left(\frac{c - \chi}{b}\right) c\sqrt{a^2 - \chi^2}$$
$$\chi = \frac{c^2 + a^2 - b^2}{2c}$$

As anticipated, temperature requirements and recharge of the batteries demand that the satellite periodically receives a minimum amount of solar radiation. To enforce this constraint, we introduced a new state variable, λ, consisting of the integral of the incoming radiation, so that

$$\frac{\mathrm{d}\,\lambda}{\mathrm{d}\,t} = \tau(x). \tag{4.1}$$

Although Equation (4.1) does not account for the attitude of the satellite, which, in turn, depends on the orientation of the sail, we believe that this simple model can offer some new insight with respect to the outcomes of [2], whereas a more advanced one would be beyond the scope of a preliminary analysis.

We assume planar orbits and the same requirement on the duration of the observations as in [2], namely that the time spent in the observation zone is equal

to 24 hours. The sail is not controlled during the observations, so that boundary conditions of the two-point boundary value problem (TPBVP) are enforced at the boundaries of the coasting arcs. Specifically, given $x_{obs} = [r_{obs}, 0]$ the state vector at the crossing of the Sun-Earth axis during the observation, boundary conditions are computed by integrating the equations of motion of the CRTBP forward and backward for a time $t_{coast} \geq 12$h, yielding

$$x_0 = x(t_{coast}), \quad x_f = x(-t_{coast}),$$

where x is solution of

$$\frac{\mathrm{d}\,x}{\mathrm{d}\,t} = f(x), \qquad x(0) = x_{obs},$$

and $f(x)$ given in Equation (1.6). For the sunlight, we require that the incoming radiation at the end of one orbit is larger than a desired value, $\lambda_{\min}$. Hence, the OCP that we tackle is:

$$\begin{aligned} \min\ & t_f \text{ subject to} \\ & \frac{\mathrm{d}\,x}{\mathrm{d}\,t} = f(x) + \varepsilon(x)\,\tau(x)Bu, \qquad u \in U \\ & \frac{\mathrm{d}\,\lambda}{\mathrm{d}\,t} = \tau(x), \\ & x(t_0) = x_0, \qquad\qquad x(t_f) = x_f, \\ & \lambda(t_0) = 0, \qquad\qquad \lambda(t_f) \geq \lambda_{\min}, \end{aligned} \tag{4.2}$$

where U denotes the control set defined in Section 1.2. The small parameter ε is proportional to the surface-to-mass ratio of the sail and to the inverse squared distance from the Sun, see Equation (1.2). Denoting by $p = (p_x, p_\lambda)$ with $p_x = (p_r, p_v)$ costate variables, the pre-hamiltonian is defined as

$$H = \ p_x \cdot (f(x) + \varepsilon\tau(x)Bu) + p_\lambda\,\tau(x)$$

where f_v denotes the projection of f on v. Application of the PMP yields

$$u^* = \arg\left(\max_{u\in U}\ H\right) = \arg\left(\max_{u\in U}\ p_v \cdot u\right),$$

which, in turn, leads to the same control action described in Proposition 15 in Section 3.1.2, the only difference being that the control force is maximized in the direction p_v instead of $\psi = p_{\delta I}\check{G}$, referring to Equation (3.2). Transversality conditions are straightforwardly deduced from Equation (4.2), yielding the

shooting problem

$$\begin{aligned} \text{find } y = (t_f, p_x(t_0), p_\lambda(t_0)) \text{ such that} \\ & x(t_0) = x_0,\ x(t_f) = x_f \\ & \|p(t_0)\| = 1 \\ & \lambda_{\min} - \lambda(t_f) \leq 0,\ p_\lambda(t_f) \geq 0 \\ & p_\lambda(t_f) \cdot (\lambda_{\min} - \lambda(t_f)) = 0 \end{aligned} \tag{4.3}$$

The last equation of Problem (4.3) indicates that the adjoint $p_\lambda(t_f) = 0$ only when the constraint on the cumulated radiation is inactive, *i.e.*, $\lambda_{min} - \lambda(t_f)$ is strictly smaller than 0, and the same minimum-time solution of [2] is found by choosing the appropriate t_{coast}. Conversely, when $\lambda_{min} - \lambda(t_f) = 0$, the sail has to spend more than the minimum time to achieve the controlled arc in order to satisfy the constraint.

Because $\tau(x)$ is not differentiable at the transitions from sunlight, penumbra, and umbra regions (more than that, $\tau = 0$ in the latter one, so that the sail cannot generate any force), multiple arcs are necessary to properly solve the shooting problem. Specifically, on top of the possible bangs that may occur for non-ideal sails (as discussed in Section 3.1.2), an arc has to be initialized at the end of each crossing of different shadowing conditions. For the sake of conciseness these details are omitted in the remainder of the manuscript.

4.3 Preliminary mission analysis

This section is aimed at investigating how solutions of Problem (4.2) evolve by varying some parameters, namely the surface-to-mass ratio of the sail, its reflectivity coefficient, t_{coast}, and λ_{min}. To this purpose, we leverage on the outcomes of [2] to obtain a first solution of Problem (4.2). Specifically, their results are recovered by choosing $\lambda_{min} = 2\,\text{h}$, t_{coast} such that the controlled arc begins after that the satellite is exposed for two hours in the sunlight region (*i.e.*, the constraint on the final radiation will be inactive), and the same ideal sail with very large surface to mass ratio.

Once obtained the first solution, a differential continuation scheme, similarly to what was presented in Section 3.2.2, is applied to decrease the surface-to-mass ratio. We use HamPath [7] software for the simulations. Figures 4.3a and 4.3b illustrate trajectory and cost function (namely, the maneuvering time) as a function of the surface-to-mass ratio, respectively. Although the value of this parameter at the end of the continuation is less than one half of the value obtained in [2], both the trajectory and the orbital period exhibit minor changes. Specifically, the deterioration of the cost function is only of the order of 15%.

Now, we fix the surface-to-mass value to its minimum level obtained above to explore the feasibility of the problem for non-ideal trajectories. Hence, we carry out

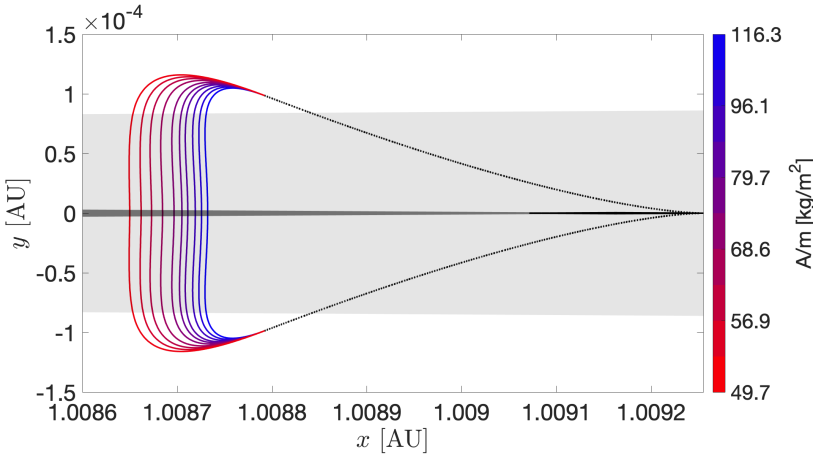

(a) Trajectories as a function of the surface-to-mass ratio for t_{coast} given in [2].

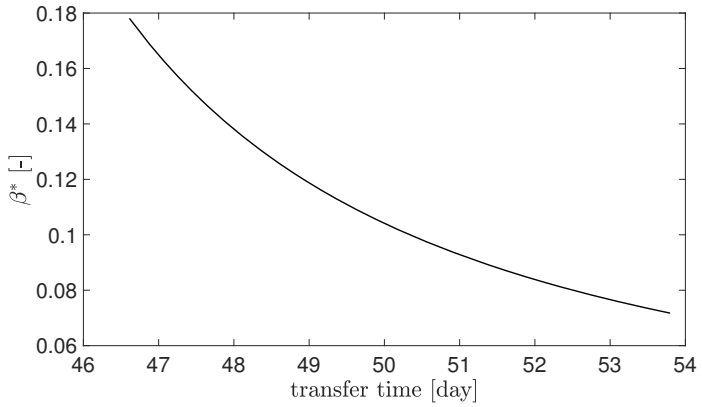

(b) Duration of total cycle time as function of the area-to-mass ratio A/m.

Figure 4.3: Deformation of the solution along the differential continuation.

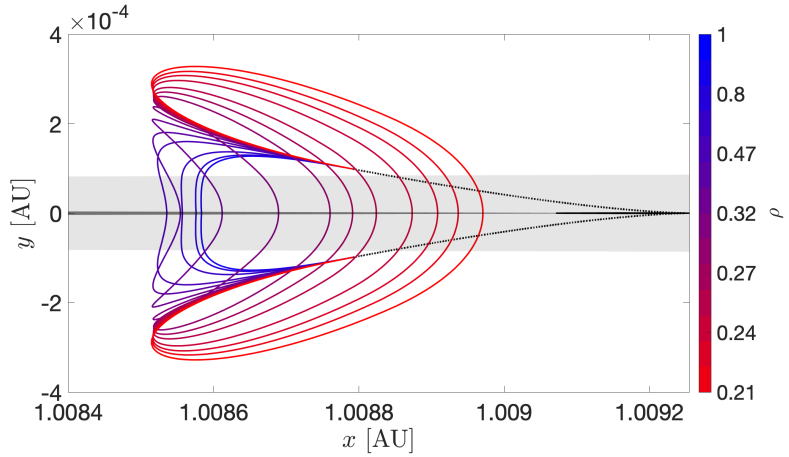

(a) Different orbits for different reflectivity coefficients ρ.

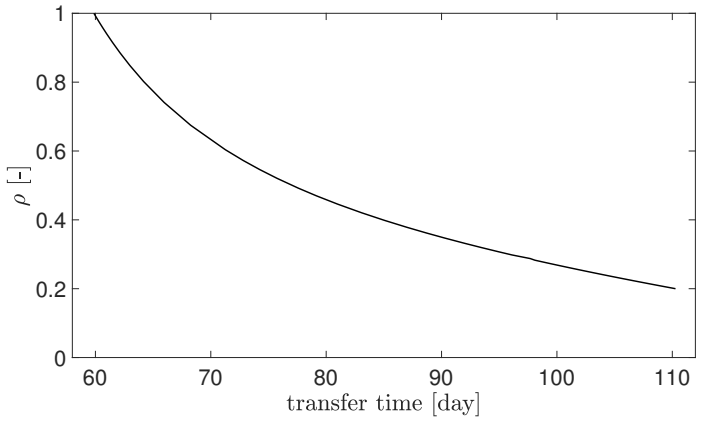

(b) Duration of total cycle time as function of reflectivity ρ.

Figure 4.4: Deformation of the solution along the differential continuation.

a second continuation aimed at decreasing the reflectivity coefficient ρ. The main outcome of this simulation is that feasible solutions exist even for very poorly-reflective sails, as illustrated in Figure 4.4a. When ρ is approximately equal to 0.3, the trajectory exhibits a bending that is due to the decrease of the maximum force in the y direction that the sail can generate (the angle of the convex cone containing U decreases with ρ, according to Equation (2.10)). Finally, we note that ρ has a major impact on the maneuvering time, as depicted in Figure 4.4b. Although sails are designed to be as ideal as possible, the reflectivity decreases during their lifetime, so that this result suggests that the time between observations will increase throughout the mission.

After having assessed the impact of physical properties on the feasibility and performance of the solutions, we relax the assumption that the satellite has to

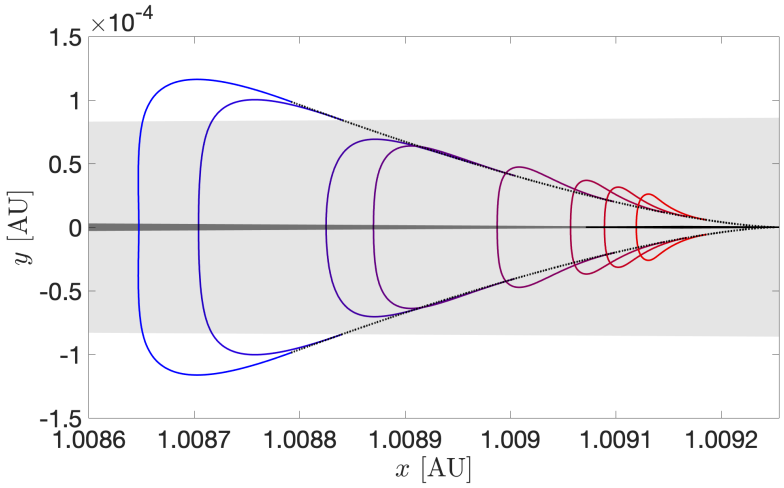

Figure 4.5: Different orbits achieved by reducing t_{coast} from 19 days (in blue) to 7 days (in red).

coast till the full sunlight and passively spend two hours there before starting the controlled arc. To this purpose, we inspect how the solutions change for decreasing values of t_{coast}. We reduced t_{coast} from 19 days for the trajectory depicted in blue in Figure 4.5 to 7 days for the trajectory in red. As the sail departs from the observation zone with zero velocity in the x direction, it accelerates while coasting. This explains why the total maneuver time increases at a slower rate compared to the distance traveled by the sail. This simulation shows that sufficient radiation may gathered in the penumbra to satisfy the constraint on $\lambda(t_f)$, as disclosed in Figure 4.5, where feasible solutions exist such that the sail never enters in the full sunlight zone.

The previous simulations demonstrated that the constraint λ_{min} of a minimum of two hours of equivalent full sunlight has a negligible impact on the trajectory, as it is satisfied at all times. However, we are interested in examining its potential influence on the resulting trajectory. To investigate this, we increase significantly λ_{min}, so that the constraint becomes active.

We choose λ_{min} to be equal to the sunlight received during the controlled arc from the previous simulation, where $t_{coast} = 11$ days (as shown in Figure 4.5). In that specific trajectory, the controlled arc lasted for 18 days, and the received sunlight corresponded to 14 days. We then employ homotopy to explore optimal trajectories with the constraint $\lambda_{min} \in [12.7, 15.4]$ days. Finally, Figure 4.6 illustrates the deformation of the family of solutions.

To facilitate understanding of difference between all the results, we summarized the simulation parameters in Table 4.1.

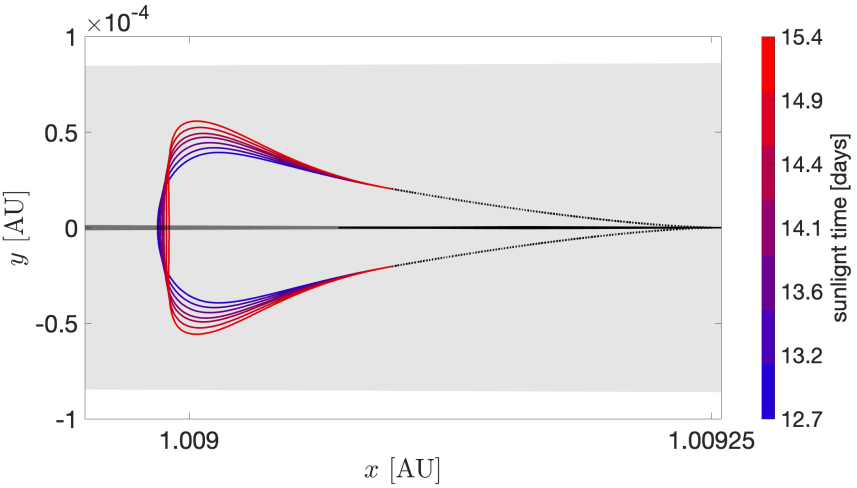

Figure 4.6: Deformation of the trajectory depending on the constraint $\lambda_{t_f} = \lambda_{min}$.

Simulation	Figure	$\frac{A}{m}$	ρ	t_{coast}	λ_{min}
1	4.3	varies	1	19 days	2h
2	4.4	49.7	varies	19 days	2h
3	4.5	49.7	1	varies	2h
4	4.6	49.7	1	11 days	varies

Table 4.1: Parameters of simulations.

Conclusion

Solar sailing enables the Sun occultation mission, as other spacecraft types require a significant ΔV, leading to high costs and limited observation cycles. Through our research, we identified feasible orbits for a realistic non-ideal solar sail, providing valuable insights for future mission designs. We included received sunlight as part of the state vector to account for the need to recharge batteries and heat the spacecraft, and examined its impact on orbital design. These preliminary results offer promising trajectories for future missions utilizing solar sails. Sun occultation is just an example of very ambitious missions that can be performed using solars sails.

Conclusion

This thesis is devoted to the geometric control of solar sails. Three contributions have been proposed ranging from the inspection of the controllability of these systems to the design of optimal maneuvers.

The first one involves a theoretical study of controllability for periodical systems with constrained control sets, whose convex hull is not a neighborhood of the origin. Lack of a formal mathematical framework to study those systems is discussed and a novel sufficient condition for global controllability is formulated. This condition is expressed by means of pushforwards along the flow of the drift, rather than in terms of Lie brackets. It turns out that this also amounts to local controllability of a time-varying linear approximation with constrained controls.

The second contribution is computational. An algorithm is devised to assess the local controllability of solar sails using convex optimization. This algorithm uses trigonometric polynomials and the theory of squared functional systems to verify the existence of a non-reachable half-space in the vicinity of the reference orbit. Furthermore, the methodology is expanded to be applicable to various types of periodic orbits and to any satellite performing station-keeping maneuvers around them. A minimum requirement for the local controllability of such systems is also proposed.

The third contribution of this thesis focuses on the study of optimal control for solar sails orbiting around celestial bodies. The dynamics of the system is thoroughly analyzed to identify the necessary conditions to find optimal trajectories. Moreover, it allows to determine the possible structures of the solution and to bound the number of control arcs over one orbit. Additionally, a switching function is introduced to initialize the solution structure for performing shooting with multiple arcs. The initial guess for the algorithm is obtained using convex optimization, which guarantees feasibility of the initialization. Advanced numerical techniques such as differential continuation, callback, and implicit computation of the optimal control action as a dynamic feedback are employed to perform numerical simulations.

Overall, we have developed highly efficient and mathematically precise techniques for addressing trajectory design during the preliminary mission analysis. The technique giving the minimum requirement allows to establish

necessary design parameters for the satellite. Additionally, the optimal control algorithm serves as a valuable tool for mission design, facilitating an effective feasibility analysis of the missions. Furthermore, advancing the development of these tools will enable their implementation onboard, playing a vital role in enhancing satellite autonomy.

Perspectives

Enhancement of the model of the dynamical environment where the solar sail moves is the first, genuine perspective of the thesis. Assessing controllability of a sail in orbit about a celestial body and subject to satellite-independent perturbations (*e.g.*, non-sphericity of the attractor) can be achieved by combining contributions of Chapters 2 and 3. Specifically, the surface-to-mass ratio of a sail could be chosen such that the average drift inducted by the perturbations at hand is compensated. Then, controllability in the presence of attitude-dependent perturbations other than SRP (*e.g.*, atmospheric drag) could be also studied. In this case, a thorough analysis of the impacts of these perturbations on the geometry of the control set is mandatory. Solar eclipses could be included in the analysis. In this case, a technical difficulty concerns the treatment of discontinuities induced by the transitions from sunlight to umbra exposure and *vice versa*, which may jeopardize the convergence of Fourier coefficients used to impose positivity constraints. Exploitation of other polynomial bases on a finite interval could be a possible way to treat this problem. Finally, assessment of controllability for stable trajectories in the framework of the elliptic restricted three-body problem, suggests the extension of the contributions of Chapter 2 to the study of quasi-periodic motion. To this purpose, positivity of multivariate trigonometric polynomials is required.

Another natural progression in line with the analysis presented in Chapter 2 is to eliminate the assumption of periodicity in the drift. Instead of considering solar sails solely in orbit around celestial bodies, the tool could be extended to analyze any reference trajectory. This would enable controllability analysis for satellites involved in interplanetary transfers, planetary fly-bys, and more complex trajectories.

In terms of the optimal control study, the next step would involve integrating attitude control with trajectory optimization to achieve more realistic results. Currently, the assumption of instantaneous changes in sail orientation, as discussed in Chapter 3, may have a significant impact on the outcomes. In practice, it is challenging to perfectly align the sail with solar rays and maintain zero control due to limitations in attitude control systems. Furthermore, the sail is not a perfectly flat and thin surface; it is attached to the satellite body, which experiences perturbations from solar radiation pressure. To address these challenges, it would

be necessary to consider a lower positive bound on the control instead of assuming zero control.

Additionally, an avenue worth exploring is making the algorithm implementable onboard the satellite itself. With an initial guess provided by convex optimization, the algorithm exhibits rapid convergence. Although convex optimization provides a sub-optimal yet feasible solution for the system, it can still be effectively implemented onboard. By utilizing this approach, the satellite can autonomously optimize its trajectory without relying on continuous communication with ground control, allowing for more efficient and adaptive operations in real-time scenarios.

Finally, expanding upon the concept presented in Chapter 4, solar sails pave the way to new possibilities for ambitious space missions. One notable advantage is the removal of the restriction imposed by the amount of available propellant on board, as solar sails do not require traditional propellants. This characteristic allows for missions with very large Δv capabilities, revolutionizing the concept of propulsion in space exploration.

Furthermore, similarly to reusable rocket boosters, solar sails can be utilized for multiple space missions. This reusability factor enhances cost-effectiveness and sustainability, as a single sail can be employed on various expeditions, optimizing resource utilization.

Solar sails excel in their ability to harness energy as they approach the Sun, resulting in increased speed. By employing a spiral trajectory towards the Sun and utilizing fly-bys to propel the sail away from the Sun's gravitational influence, it becomes feasible to send sails to the farthest regions of the solar system and potentially even beyond. This opens up exciting opportunities for exploring mysteries and unanswered questions within our solar system. Various intriguing phenomena within our solar system continue to pique scientific curiosity. Examples include the quest to uncover the existence of Planet 9, the possibility of small black holes residing in our solar system, the nature and composition of objects in the Kuiper Belt extending beyond Neptune's orbit, and the enigmatic Oort Cloud—the outermost region of the solar system. Investigating and studying these enigmas necessitate spacecraft capable of observations and flybys. Solar sails offer a promising solution to address these mysteries, enabling the construction of low-cost, fast light sails capable of reaching the distant regions of our solar system. Moreover, solar sails open up the possibility of venturing beyond our solar system. This advancement could enable missions to the focal region of the solar gravitational lens, facilitating exoplanet imaging, or even missions to other stellar systems. By pushing the boundaries of our solar system, solar sails hold the potential for groundbreaking discoveries and unprecedented exploration endeavors.

Bibliography

[1] A. A. Agrachev and Y. L. Sachkov, *Control Theory from the Geometric Viewpoint*, vol. 87 of Encyclopaedia of Mathematical Sciences, Springer Berlin Heidelberg, 2004.

[2] N. Bernardini, N. Baresi, R. Armellin, S. Eckersley, and S. A. Matthews, *Trajectory design of earth-enabled sun occultation missions*, Acta Astronautica, 195 (2022), pp. 251–264.

[3] B. Bonnard, *Contrôlabilité des systèmes non linéaires*, Comptes Rendus des Séances de l'Académie des Sciences. Série I. Mathématique, 292 (1981), pp. 535–537.

[4] B. Bonnard, J.-B. Caillau, and E. Trélat, *Geometric optimal control of elliptic keplerian orbits*, Discrete & Continuous Dynamical Systems - B, 5 (2005), pp. 929–956.

[5] P. Boulle, *La Planète des singes*, Julliard, 1963.

[6] J. P. Boyd, *Computing the zeros, maxima and inflection points of Chebyshev, Legendre and Fourier series: solving transcendental equations by spectral interpolation and polynomial rootfinding*, Journal of Engineering Mathematics, 56 (2007), pp. 203–219.

[7] J.-B. Caillau, O. Cots, and J. Gergaud, *Differential continuation for regular optimal control problems*, Optimization Methods and Software, 27 (2012), pp. 177–196.

[8] J.-B. Caillau and B. Daoud, *Minimum time control of the restricted three-body problem*, SIAM Journal on Control and Optimization, 50 (2012), pp. 3178–3202.

[9] J.-B. Caillau, L. Dell'Elce, A. Herasimenka, and J.-B. Pomet, *On the controllability of nonlinear systems with a periodic drift*, (2022). HAL preprint no. 03779482.

[10] J.-B. Caillau, J. Féjoz, M. Orieux, and R. Roussarie, *On singularities of min time affine control systems*, SIAM Journal on Control and Optimization, 60 (2022), pp. 1143–1162.

[11] J.-B. Caillau and J. Noailles, *Coplanar control of a satellite around the Earth*, ESAIM: Control, Optimisation and Calculus of Variations, 6 (2001), pp. 239–258.

[12] A. Caruso, M. Bassetto, G. Mengali, and A. A. Quarta, *Optimal solar sail trajectory approximation with finite fourier series*, Advances in Space Research, 67 (2021), pp. 2834–2843. Solar Sailing: Concepts, Technology, and Missions II.

[13] A. Caruso, G. Mengali, A. A. Quarta, and L. Niccolai, *Solar sail optimal control with solar irradiance fluctuations*, Advances in Space Research, 67 (2021), pp. 2776–2783.

[14] L. Carzana, P. Visser, and J. Heiligers, *Locally optimal control laws for earth-bound solar sailing with atmospheric drag*, Aerospace Science and Technology, 127 (2022), p. 107666.

[15] A. C. Clarke, *La Planète des singes*, Harcourt Brace Jovanovich, 1972.

[16] C. Colombo, N. Miguel Banos, and I. Gkolias, *Modulating Solar Sail Control for End-Of-life Disposal with Solar Sails*, in 5th International Symposium on Solar Sailing, Aachen, Germany, 2019.

[17] J.-M. Coron, *Control and Nonlinearity*, American Mathematical Society, aug 2009.

[18] S. R. Cranmer, S. E. Gibson, and P. Riley, *Origins of the ambient solar wind: Implications for space weather*, in The Scientific Foundation of Space Weather, Springer Netherlands, 2017, pp. 41–80.

[19] H. D. Curtis, *Orbital mechanics for engineering students*, Butterworth-Heinemann, 2013.

[20] B. Dachwald, *Optimal solar sail trajectories for missions to the outer solar system*, in AIAA/AAS Astrodynamics Specialist Conference and Exhibit, American Institute of Aeronautics and Astronautics, jun 2004.

[21] B. Dachwald, M. Macdonald, C. R. McInnes, G. Mengali, and A. A. Quarta, *Impact of Optical Degradation on Solar Sail Mission Performance*, Journal of Spacecraft and Rockets, 44 (2007), pp. 740–749.

[22] B. Dumitrescu, *Positive Trigonometric Polynomials and Signal Processing Applications*, Springer Netherlands, 2007.

[23] S. Eckersley and S. Kemble, *Method of solar occultation*, Airbus DS Patent 9,676,500, 2017.

[24] A. Farrés and À. Jorba, *A dynamical system approach for the station keeping of a solar sail*, The Journal of the Astronautical Sciences, 56 (2008), pp. 199–230.

[25] J. Gergaud and T. Haberkorn, *Homotopy method for minimum consumption orbit transfer problem*, ESAIM: Control, Optimisation and Calculus of Variations, 12 (2006), pp. 294–310.

[26] M. Grant and S. Boyd, *Graph implementations for nonsmooth convex programs*, in Recent Advances in Learning and Control, V. Blondel, S. Boyd, and H. Kimura, eds., Lecture Notes in Control and Information Sciences, Springer-Verlag Limited, 2008, pp. 95–110.

[27] M. Grant and S. Boyd, *CVX: Matlab software for disciplined convex programming, version 2.1*. `http://cvxr.com/cvx`, Mar. 2014.

[28] J. Hao, C. R. Glein, F. Huang, N. Yee, D. C. Catling, F. Postberg, J. K. Hillier, and R. M. Hazen, *Abundant phosphorus expected for possible life in enceladus's ocean*, Proceedings of the National Academy of Sciences, 119 (2022).

[29] A. F. Heaton and A. Artusio-Glimpse, *An update to the NASA reference solar sail thrust model*, in AIAA SPACE 2015 Conference and Exposition, American Institute of Aeronautics and Astronautics, aug 2015.

[30] A. Herasimenka, L. Dell'Elce, J.-B. Caillau, and J.-B. Pomet, *Controllability test for fast-oscillating systems with constrained control. Application to solar sailing*, in European Control Conference (ECC), 2022, pp. 2143–2148.

[31] A. Herasimenka, L. Dell'Elce, J.-B. Caillau, and J.-B. Pomet, *Controllability properties of solar sails*, Journal of Guidance, Control, and Dynamics, (2023), pp. 1–10.

[32] A. Herasimenka, A. Farrés, and L. Dell'Elce, *Station-keeping under conical constraint on the control force*, (2023). HAL preprint no. 04156856.

[33] R. A. Jacobson and C. L. Thornton, *Elements of solar sail navigation with application to a halley's comet rendezvous*, 1 (1978), pp. 365–371.

[34] V. Jurdjevic, *Geometric Control Theory*, Cambridge University Press, 1 ed., 1996.

[35] V. Jurdjevic and I. Kupka, *Control systems on semisimple Lie groups and their homogeneous spaces*, Annales de l'Institut Fourier, 31 (1981), pp. 151–179.

[36] R. Kataoka, D. Shiota, H. Fujiwara, H. Jin, C. Tao, H. Shinagawa, and Y. Miyoshi, *Unexpected space weather causing the reentry of 38 starlink satellites in february 2022*, Journal of Space Weather and Space Climate, 12 (2022), p. 41.

[37] M. Kim and C. Hall, *Symmetries in the optimal control of solar sail spacecraft*, Celestial Mechanics and Dynamical Astronomy, 92 (2005), pp. 273–293.

[38] C. Lobry, *Contrôlabilité des systèmes non linéaires*, SIAM J. Control, 8 (1970), pp. 573–605.

[39] M. Macdonald, C. McInnes, and B. Dachwald, *Heliocentric solar sail orbit transfers with locally optimal control laws*, Journal of Spacecraft and Rockets, 44 (2007), pp. 273–276.

[40] C. R. McInnes, *Solar Sailing*, Springer London, 1999.

[41] G. Mengali and A. Quarta, *Near-optimal solar-sail orbit-raising from low earth orbit*, Journal of Spacecraft and Rockets, 42 (2005), pp. 954–958.

[42] G. Mengali and A. A. Quarta, *Optimal three-dimensional interplanetary rendezvous using non-ideal solar sail*, Journal of Guidance, Control, and Dynamics, 28 (2005), pp. 173–177.

[43] O. Montenbruck and E. Gill, *Satellite Orbits*, Springer Science + Business Media, 2000.

[44] Y. Nesterov, *Squared Functional Systems and Optimization Problems*, in High Performance Optimization, P. M. Pardalos, D. Hearn, H. Frenk, K. Roos, T. Terlaky, and S. Zhang, eds., vol. 33, Springer US, Boston, MA, 2000, pp. 405–440. Series Title: Applied Optimization.

[45] L. Niccolai, A. Quarta, and G. Mengali, *Analytical solution of the optimal steering law for non-ideal solar sail*, Aerospace Science and Technology, 62 (2017), pp. 11–18.

[46] L. Niccolai, A. Quarta, and G. Mengali, *Solar sail heliocentric transfers with a q-law*, Acta Astronautica, 188 (2021), pp. 352–361.

[47] L. Niccolai, A. Quarta, and G. Mengali, *Trajectory approximation of a solar sail with constant pitch angle and optical degradation*, IEEE Transactions on Aerospace and Electronic Systems, 58 (2022), pp. 3643–3649.

[48] V. U. J. Nwankwo, *Space weather: Response of the atmosphere to solar activity and its implications for LEO satellites aerodynamic drag*, in Astrophysics and Space Science Proceedings, Springer International Publishing, 2018, pp. 637–644.

[49] T. Okada, Y. Kebukawa, J. Aoki, J. Matsumoto, H. Yano, T. Iwata, O. Mori, J.-P. Bibring, S. Ulamec, and R. Jaumann, *Science exploration and instrumentation of the OKEANOS mission to a jupiter trojan asteroid using the solar power sail*, Planetary and Space Science, 161 (2018), pp. 99–106.

[50] A. Peloni, M. Ceriotti, and B. Dachwald, *Solar-sail trajectory design for a multiple near-earth-asteroid rendezvous mission*, Journal of Guidance, Control, and Dynamics, 39 (2016), pp. 2712–2724.

[51] A. Peloni, A. V. Rao, and M. Ceriotti, *Automated trajectory optimizer for solar sailing (ATOSS)*, Aerospace Science and Technology, 72 (2018), pp. 465–475.

[52] J. Petersen, *L2 station keeping maneuver strategy for the james webb space telescope*, in AIAA/AAS Astrodynamics Specialist Conference, American Institute of Aeronautics and Astronautics, 2019.

[53] C. Porco, D. DiNino, and F. Nimmo, *How the geysers, tidal stresses, and thermal emission across the south polar terrain of Enceladus are related*, The Astronomical Journal, 148 (2014), p. 45.

[54] F. Postberg, J. Schmidt, J. Hillier, S. Kempf, and R. Srama, *A salt-water reservoir as the source of a compositionally stratified plume on enceladus*, Nature, 474 (2011), pp. 620–622.

[55] L. Rios-Reyes and D. J. Scheeres, *Generalized model for solar sails*, Journal of Spacecraft and Rockets, 42 (2005), pp. 182–185.

[56] R. Schwenn, *Space weather: the solar perspective*, Living Reviews in Solar Physics, 3 (2006), p. 2.

[57] Y.-F. G. Sheng-Pin Gong and J.-F. Li, *Solar sail time-optimal interplanetary transfer trajectory design*, Research in Astronomy and Astrophysics, 11 (2011), p. 981.

[58] Y. Song and S. Gong, *Solar sail trajectory optimization of multi-asteroid rendezvous mission*, Acta Astronautica, 157 (2019), pp. 111–122.

[59] M. Spivak, *A Comprehensive Introduction to Differential Geometry*, Publish or Perish, Houston (U.S.A.), second ed., 1979.

[60] N. Sullo, A. Peloni, and M. Ceriotti, *Low-thrust to solar-sail trajectories: A homotopic approach*, Journal of Guidance, Control, and Dynamics, 40 (2017), pp. 2796–2806.

[61] S. G. Turyshev, D. Garber, L. D. Friedman, A. M. Hein, N. Barnes, K. Batygin, M. E. Brown, L. Cronin, A. Davoyan, A. Dubill, S. Gibson, D. M. Hassler, N. R. Izenberg, P. Kervella, P. D. Mauskopf, N. Murphy, A. Nutter, C. Porco, D. Riccobono, J. Schalkwyk, K. B. Stevenson, M. V. Sykes, M. Sultana, V. T. Toth, M. Velli, and S. P. Worden, *Science opportunities with solar sailing smallsats*, 2023.

[62] J. H. Waite Jr, W. S. Lewis, B. A. Magee, J. I. Lunine, W. B. McKinnon, C. R. Glein, O. Mousis, D. T. Young, T. Brockwell, J. Westlake, M.-J. Nguyen, B. D. Teolis, H. B. Niemann, R. L. M. Jr, M. Perry, and W.-H. Ip, *Liquid water on enceladus from observations of ammonia and 40ar in the plume*, Nature, 460 (2009), pp. 487–490.

[63] D. F. Webb and T. A. Howard, *Coronal mass ejections: observations*, Living Reviews in Solar Physics, 9 (2012), p. 3.

[64] J. Zhu, E. Trélat, and M. Cerf, *Geometric optimal control and applications to aerospace*, Pacific Journal of Mathematics for Industry, 9 (2017).